Oskar Darselius Berg
Master Thesis
N15
Spring 2020

Thermal Stability of Titanium and Niobium Stabilized Stainless Steel

Preface

This is a master thesis performed in Engineering Nanoscience, during 20 weeks at Alfa Laval AB 2020. The work has been conducted in Lund, at the department of Material Technology and Chemistry and the Division of Synchrotron Radiation Research at Lund University. The master thesis involves investigating the microstructure of the stainless steel used in the brazed heat exchanger at Alfa Laval, as well as high temperature stainless steel alternatives for future usage. This is done through comparing several types of heat treatment. Especially investigating temperature series, including the non-treated material. How pre-deformed stainless steels react to heat treatment is also investigated.

The work also includes a feasibility study of the usage of X-ray diffraction to identify surface oxide content on stainless steel, since this is a critical part of the functionality of stainless steels.

Acknowledgements

To everybody at Alfa Laval and the Division of Synchotron Research who has helped me in this study, I would like to say thank you very much. I would especially like to thank Axel Knutsson for helping me with everything, from showing me where to find the coffee at Alfa Laval to allowing me to be a part of the extremely cool MAX IV experiments. Thank you Patrik Åkerlund for tirelessly proof reading this work and helping me with everything metallurgy related.

I would also like to say thank you to Niklas Olsson and Roland Johansson, for helping me with everything that is not displayed in this master thesis. All of the metallic cutting, polishing, curing of epoxy pucks and more. The tips and tricks you have given me has made all of my experiments significantly easier.

Thank you, Kim von Allmen for helping me with the X-ray diffraction and the data analysis associated with it. Thank you, Johan Gustafson, for not only giving me the opportunity to use the X-ray machine but also helping me with all of my random questions. I would also like to thank Carina Fasth, my thesis examiner.

Last but not least, I would like to thank Filip Lenrick for putting me in touch with this awesome opportunity.

Abstract

This master thesis examined the microstructure after heat treatments in stainless steel, two conventional stainless steel (304 and 316) and two novel high temperature stainless steel. These stainless steels are for the use in high temperature heat exchangers for extended temperature range. The positive characteristics in stainless steel are inversely correlated to grain size, characteristics such as strength and mechanical isotropy. Therefore, the grain size will be investigated after heat treatment at several high temperatures (1020℃, 1130℃ and 1230℃).

Further, the study contained an investigation of the oxide layer with X-ray diffraction, since the oxide plays a vital role in protecting the stainless steel from corrosion.

The grain size was investigated through the ASTM E112-10 methodology, which measures the amount of grain boundaries per unit length. This is performed three times to obtain an average. This was compared to conventional cross-sectional measurements. This showed a difference in maximum 10 µm, which is deemed adequately representative.

ASTM E112-10 method shows that the high temperature stainless steels (321H and 347H) have a smaller grain size up to 1030℃ heat treatment. The method also shows anisotropy in the grain size between the different directions, planar and cross-sectional. This anisotropy was most extreme in the conventional stainless steel 304.

The grain size of these stainless steels was also investigated with and without exposure to nitrogen gas during heat treatment. Nitrogen in the matrix acts as a grain refiner, which should mean smaller grains in the samples exposed to nitrogen gas. The results followed the theory, since most of the samples and directions display smaller grains when exposed to nitrogen gas. This is with exception to three samples; 304 planar, 316 cross-sectional and 321 planar. 321H planar and 316 cross-sectional displays small differences, inadequate for any conclusions. 304 planar does however display a large difference.

What makes the high temperature steels' (321H and 347H) more temperature stable are their particles. 321H has precipitation of titanium carbide, TiC, and 347H has precipitation of niobium carbide, NbC. TiC does convert (at least somewhat) into titanium nitride, TiN, even before any exposure to nitrogen gas.

The plastic deformation effect on the heat-treated samples is also investigated. The texture change generates larger grain size in all samples except 347H, which exhibits smaller grains. This means that heat exchangers will have larger grains in the deformed parts, except for heat exchangers made from 347H.

For the plastically deformed samples of 321H there were no main difference in particles after heat treatment, neither size nor amount. For the NbC particles in 347H an increased precipitation is observed as well as a stagnation of growth after a certain point.

X-ray diffraction which was performed on the 316 powder generates a signal. There is no signal at the point where the oxide should be placed on the detector, however there is a clear signal from the stainless steel. Further investigation is needed since most of the beam was blocked, however that was hindered due to the Covid-19 pandemic.

Contents

1. Introduction

Steel is essentially iron alloyed with carbon in order to improve mechanical properties such as stiffness and hardness, mainly through atomic obstruction by interstitial carbon atoms. [1] Steel is one of the most common materials. Its versatile characteristics when it comes to mechanical and chemical properties combined with its low price makes for an excellent material. It is extremely versatile, usage ranging from cargo ships to kitchen sinks.

Stainless steel, in turn, is achieved by adding Cr to the steel. This new alloy is claimed to have been invented by Harry Brearly, who mixed in 12 wt% Cr into the steel in order to improve the wear resistance. The Cr did not improve the wear resistance, but the corrosion resistance was greatly improved. This is due to a Cr oxide film forming on the surface when exposed to air, effectively hindering further oxidation and corrosion.

Due to the severity of the times, during World War II, new manufacturing methods was rapidly innovated to keep up with the shortages of medical equipment. This was the time where austenitic stainless steel was starting to be developed and put into practice. The new material allowed for a corrosion resistant, and hence durable and hygienic, handling of everything from food to medicine. Today we live in a world with vast access to both food and medicine. This can in some sense can be attributed to the stainless-steel development of the 20th century. [3] However, the steel production releases a lot of carbon dioxide. In fact, the single largest carbon dioxide producer in Sweden is SSAB, which produces the iron needed for creation of stainless steel. [2]

Even though the stainless steel of today is a great contributor to society's wealth, it is not without its disadvantages. There are several different grades of steel tailormade for specific applications. The stainless steels commonly used today only works in temperature intervals up to approximately 800°C, but many modern applications demand a better durability at even higher temperatures. One example of such applications is heat exchangers, which consists of a network of channels where the heat from one medium can be transferred to another. For certain applications, the function of the heat exchanger would be improved if the temperature of the medium could be increased. The goal with this project is to investigate higher temperature stainless steels, for this exact application. [3]

These high temperature steels, 321H and 347H, are investigated and compared with the traditional stainless steels, 304 and 316. The microstructural surface is inspected using optical microscopy and energy dispersive X-ray spectroscopy during several different conditions, before/after heat treatment and plastic deformation of the material.

Corrosion is a big problem in stainless steel heat exchangers. What protects the stainless steel is the native oxide, a few nanometer thick Cr_2O_3. Using X-ray diffraction, the goal is to be able to resolve the oxide for future application in noticing corrosion in heat exchangers.

1.1 Alfa Laval

Alfa Laval was founded in 1883 by Gustaf de Laval and Oscar Lamm. Their original business

was manufacturing and selling separators and still to this day Alfa Laval deals with specialized products for industry. One example of this is heat exchangers, which will be the subject of this report. These products are used to cool, heat, separate and transport products as chemicals, water and oil.
The company has subsidiary companies in almost 100 countries. Today Alfa Laval has over 3700 patents and has an innovative culture, investing 2.3% of its annual sales in research. This leads to the launch of 35-40 new products every year. [4]

1.2 Scope and Objective

The goal of this project is to investigate high temperature stainless steels for later applications within brazed heat exchangers. This would allow for heat exchangers which can operate at higher temperatures and hence be operational for new areas of application. The stainless steels up for investigation are 321H and 347H. These will be compared with the conventional stainless steels 304 and 316. All the samples will be put through heat treatments to see how these affect their microstructures in different ways.

The investigations were done through optical microscopy, before and after heat treatment. Specific interest will be towards calculating the grain size.

Figure 1.1: *An example of a grain in stainless steel*

Figure 1.1 shows a grain, which is a small volume of a metal, which contains a homogenous crystal structure. The particles of the high temperature steels will be investigated as well, both through optical microscopy (counting the number of particles and taking note of their area) and chemically quantifying them through energy dispersive X-ray spectroscopy (EDX). These particles are a hard-secondary phase present, which give particular macroscopic material qualities. These material characteristics will be compared regarding before and after heat treatment.

The same procedures will be conducted after plastically deforming the samples with the intention to spot differences in grain size, as well as general observation of the behavior of the materials. The intent is to observe whether the plastic deformation catalyzes grain growth through an increase of nucleation point, inhibits grain growth due to the extra energy needed to release the residual stresses or affect the material so little that the deformation has no effect. Observations such as precipitation of particles and phases which may contribute to the material's macroscopic behaviors is also investigated in these plastically strained samples.

1.3 Austenitic Stainless Steel

There are several different crystal structures of steel, distinguished as several phases within the material. This Master Thesis considers austenitic stainless steel. Austenitic stainless steel is a face centered cubic (FCC) based steel (Fe has an FCC structure abbreviated with γ-Fe), usually characterized by its chromium and nickel content. Together with carbon, these elements are almost always present in austenitic stainless steel. [1]

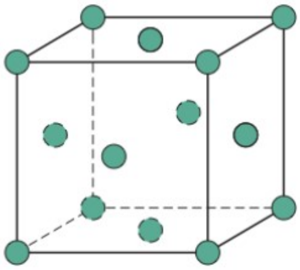

Figure 1.2: *The crystallographic structure of FCC* [5]

Figure 1.2 describes FCC structure and that it has a packing factor of 74%. The FCC has an atomically content of 4 atoms in the repeating structure.

Austenite is a stable and applicable steel used over a wide range of temperatures and environments. It is usually referred to as having great ductility (due to the FCC structure) and suitable for heavy forming operations. The corrosion resistance of austenite is generally considered to be excellent and makes for a great use in a heat exchanger, which often operate in corrosive environments and high temperatures.

Generally, austenitic stainless steel has the goal of being one single phase structure without any secondary phase precipitation. Precipitation is when a decrease in solubility generates a segregation of the material matrix into separate phase. These separate phases could however be useful, since secondary particles may inhibit deformation. How these functions are however dependent on their chemical relationship with the rest of the material matrix. [1]

1.4 Additives and their Effect

Table 1.1: *The general chemical composition of austenitic of stainless steel, given in weight percent.* [3]

	C (wt%)	Cr (wt%)	Ni (wt%)	Mo (wt%)	Crystal Structure
Austenitic	<0.08	16-20	8-25	0-6	FCC

Table 1.1 shows that the austenitic stainless steel can be distinguished by its additives. These additives and their effect on the austenitic structure will be considered more deeply in this

section. Further, in this section ferrite (α and/or F), cementite (Fe_3C) and Ni_3Fe (γ´) considered unwanted separate phases.

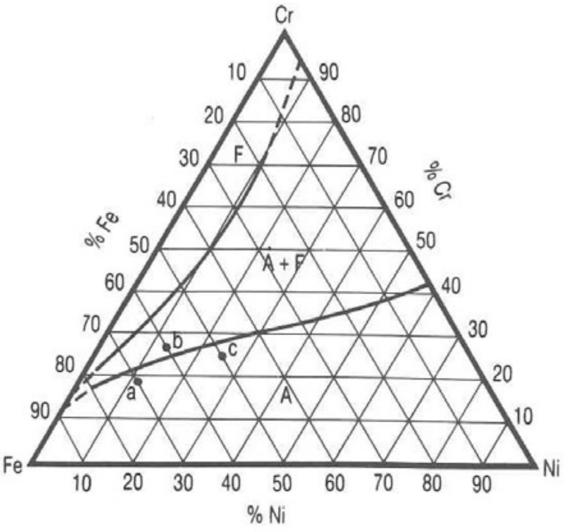

Figure 1.3: *1000 ℃ section of a Fe-Cr-Ni ternary diagram, illustrating the effect on the structure by the addition of Ni and Cr. More Ni and Cr clearly display a higher fraction of austenitic phase. A = Austenite, F = Ferrite.* [1]

Figure 1.3 illustrates how the high temperature structure of the stainless steels depends on the relative amount of chromium and nickel. The chromium stabilizes the ferritic phase and nickel stabilizes austenitic, by occupying the tetrahedral void in the FCC structure. This is essentially is how acquiring the austenitic structure occurs in practice, by adding nickel to a ferritic structure. That means when adding a Cr to the steel to make it stainless, it needs additional Ni for the (now) stainless steel to have an FCC crystalline structure. A lot of nickel can also generate a γ′-phase (Ni_3Fe). [1]

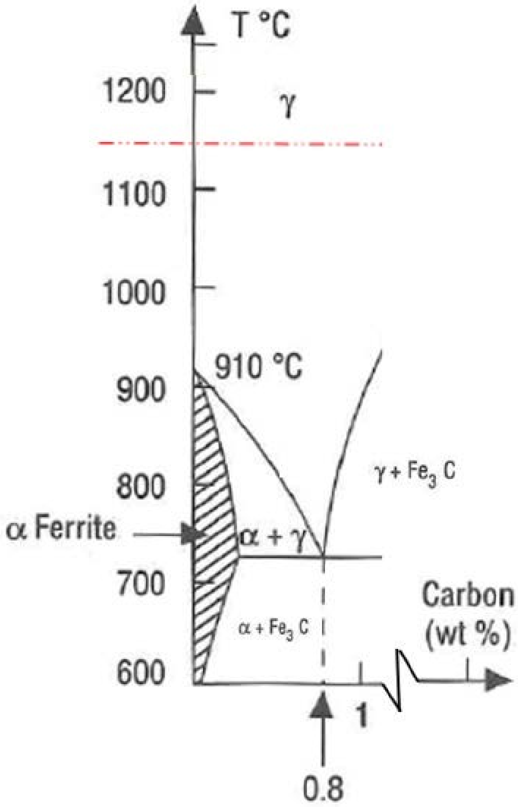

Figure 1.4: *An illustration of that carbon is an austenitic stabilizer, as well as increased solubility of carbon (in austenite) at higher temperatures. This is illustrated by the disappearance of* α*-Fe at higher temperature (above 910℃).* [1]

Figure 1.4 shows carbon as an γ-Fe stabilizer and that the austenitic stainless steel can absorb a lot of carbon at elevated temperatures up to 0.08 wt%. Carbon occupies the octahedral void in the FCC crystal structure, as does nitrogen. Observe that this figure is an example of steel, not an example of this thesis specific austenitic steel. The solubility of carbon decreases as the temperature decreases, which may cause precipitation of unwanted $Cr_{23}C_6$.This precipitation is generally taking place in the sensitization region (425-800℃). Therefore, to obtain a stable austenitic stainless steel meanwhile avoiding precipitation of carbon one generally solution anneal the material, followed by quenching (rapid cooling). Solution annealing is heating the material up to a relative high temperature to relive residual stresses and stabilizing a phase. Solution annealing is usually performed at approximately 1000-1150℃ (see dashed red line at 1150℃). [1]

Carbon is generally considered the most important steel alloying element. Carbon increases the hardness, by obstructing atomic slip. Carbon addition is not only positive since increasing the carbon content decreases weldability because of the material’s tendency to form martensite, generally an unwanted phase of steel. [6]

Molybdenum is used in a stainless steel for increased corrosive resistance, as in 316 stainless steel. Molybdenum promotes formation of the BCC material matrix (ferrite) and hence needs sufficient nitrogen addition for the austenitic material matrix to be maintained Molybdenum also promotes formation of σ-phase. σ-precipitation will cause a brittle material. [1]

Titanium and niobium (used in 321 and 347 grades of stainless steel) are ferrite stabilizers. They however also bond to nitrogen and carbon, and hence stabilizing γ-Fe by keeping these additives in the material. Nitrogen is in similarity to carbon, a strong γ-Fe stabilizer. [1] Prolonged exposure to temperatures within the temperature range 425-800°C, the carbide and chromium precipitation region, may create and unstable material. This is called sensitization. This may cause intergranular corrosion in austenitic steels with high carbon content, typically with a name denoted with the letter "H". This is because the lack of chromium in regions makes the material weak, or non-stainless which may be caused by sensitization. The chromium usually precipitates as a $Cr_{23}C_6$. Likewise, the precipitation of chromium in high chromium austenite causes σ-phase precipitation. [7]

The austenitic stainless steel contains an FCC crystalline matrix, with several different grains with different crystalline orientation. In theory this should not exist, since it is not thermodynamically stable. However, to make these disappear energy need to be provided into the structure to induce grain growth, see section 1.6.

One common reason for failure of materials is the gathering of dislocations/voids, causing a crack. Grains obstruct dislocational motion through their boundaries and therefore creates a less failure prone material, hence making the grained structure stronger. These grain boundaries store energy from deformations which specific effect will also be studied in this thesis. [7]

1.5 Deformation

During metal deformation the metal changes in several significant ways. At the atomic scale it forces the atoms from their original positions in the crystal structure, known as atomic slip. The grains are hence deformed, and the new grain boundaries are created. The new added grain boundary area is due to the addition of new dislocations, crystalline imperfections. All the energy stored by the material is exhibited through dislocations. However, 99% of the (deformational) energy provided is relived as heat.

The single crystalline grains change their orientation in accordance with the applied force. The rotation of the grains depends on the crystal in question, creating a deformed texture in the material. This means that the summation (texture) of crystalline orientations is deformed in accordance with the applied force. This increases the grain boundary area.

Austenite's FCC crystal has two major deformational modes, atomic slip and twinning. [7]

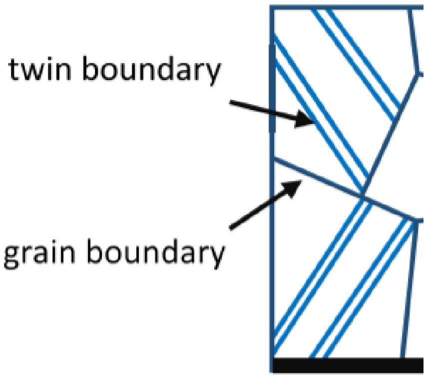

***Figure 1.5:** An illustration of a grain boundary and twinning.* [8]

Figure 1.5 shows that twinning is a straight-line grain boundary, created by stacks of dislocations. The slip state takes place within the close-packed planes ({111}) and in the close-packed directions (<110>). The slip in metals causes generally two consequences; deformation microstructures which causes deformation textures. [7]

1.6 Recrystallization

During deformation of crystalline materials, the free energy is raised. This is due to the increased presence of dislocations and interfaces within the crystal structure. According to thermodynamics, this state should spontaneously vanish. Although the necessary atomistic mechanism is usually very slow at room temperature. Heating the crystal structure allows atoms to move more freely (due to increased diffusion rate). This process is called annealing.

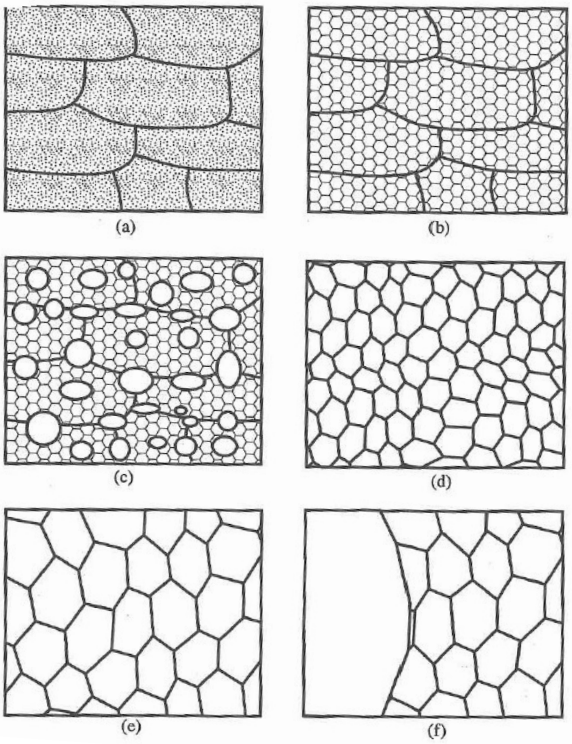

***Figure 1.6:** Illustrations of the main steps of annealing over time: (a) Deformed state (b) Recovered state, however containing dislocational structure (illustrated by hexagonal pattern) (c) Partial recrystallized state (d) Fully recrystallized state (e) Grain growth (d) Abnormal grain growth* [7]

Figure 1.6 illustrates the annealing steps; Recovery, Recrystallisation and Grain growth. During recovery, dislocations (crystalline imperfections) are relocated as well as annihilated (see figure 1.6a to 1.6b). This change does not generally affect grain boundaries during recovery.

The removal of dislocations may suggest a return to a non-defomed state, although that is not true. This is since the dislocation structure (now defect structure) is not removed, only the dislocations themselves. The material defect is a disruption in the perfect material arrangement and in figure 11b shows the defect structure after the disappearance of dislocations. The dislocation structure is still present, therefore creating a meta-stable state. The next state of annealing removes these structures, during recrystallisation.

In recrystallisation new (dislocation free) grains nucleates within the structure (figure 1.6c). During this phase, in annealing, new grains grows and consumes the old grains. This creates a new structure, free from the dislocational structure.

Even though these new grains are lacking the induced dislocations, the new material still contains thermodynamically unstable grain boundaries (figure 1.6d). Due to this fact, subsequent annealing may cause grain boundaries to disappear. This is the next step in annealing, grain growth (figure 1.6e). This is the step to avoid in this thesis.

During grain growth the smaller grains are eliminated first, which causes the biggest drop in free energy due to maximum elimination of grain boundaries. The consumption of smaller grains by bigger grains is known as Ostwald Ripening. In rare cases the selective growth of a few grains may occur. This is known as abnormal grain growth (figure 1.6f). [7]

1.7 Grain Growth

The isothermal grain growth within materials seems to be very similar, regardless of the type of alloy. The growth of grain radii, R, can be described by

$$< R^n > - < R_0^n > = ct \tag{1}$$

where n and c are constants for each material, t is the growth time, RR_0 is the start radii for the grain growing, $<x>$ is the mean value for x and n is usually a number around 2. Growth time is when previous annealing steps are completed, and annealing time is the total time the material has been heat treated. [7] Due to equation 1 and that n is usually around 2, radius generally increases as a function of the square root of the annealing time. [9]

The grain growth is generally influenced by several factors. Grain growth (exception for abnormal grain growth) is characterized by high angle grain boundary movement, meaning growth of grains and not twin boundaries. This movement is very small or non-existent at low temperatures and need high temperatures for any substantial movement at all. Since the grain boundary movement is by definition linked to texture, the texture has a substantial effect on the grain growth. While temperature catalyzes grain growth, solutes and particles tend to immobilize the material and inhibit grain growth. The grain growth may also be inhibited by many low angle grain boundaries with a low potential energy. Hence, a highly textured material inhibits grain growth. [7, 9]

Abnormal grain growth is a discontinuous process in which a few grains start growing faster than the surrounding matrix. This can be, however not limited to, an unpinning from particles/the rest of the material matrix. Therefore, this allows for an unhinged grain growth in this specific grain. Abnormal grain growth can be defined as whether a large grain radius has increased faster than the average grain size

$$\frac{d}{dt}\left(\frac{R_{large}}{< R >}\right) > 0 \tag{2}$$

where R_{large} is the large grain radius. Abnormal grain growth may however be hard to discover due to the general crude methodology used when investigating grain size generally. The cutting generally performed on metallurgical samples may somewhat destroy the surface. To avoid this, one needs to conclude a normalized grain growth distribution for the sample to be considered representative. [7, 9]

1.8 Particles effect on the material

Particles dispersed in the metal matrix will exert a retarding pressure on a slip in the material and may affect the recovery, recrystallisation and grain growth. This is known as Zener's drag, and might affect the 321H and 347H (the novel stainless steel) due to their particles. This is affected by several parameters, such as shape, size, particle spacing, volume fraction and most importantly coherence.

The Zener drag exerted by a single particle in a grain boundary attracts (energetically) more particles by lowering the boundary energy. A particle coherent (chemically bonded) with the surrounding material matrix does not only attract more particles, but also provides more resistance to atomic slip than an incoherent particle. A coherent particle requires the double of force excreted for slip, compared to an incoherent particle. If a high angle grain boundary (e.g. twin boundary) slips past the particle, the particle is losing its coherency.

The lack of coherency of a particle will result in a less stable particle, through the Gibbs-Thomson effect. This may cause the particle to dissolve and re-precipitate from the bulk in a coherent state or cause the particle to be cut and thus become a part of the boundary. The obstruction of randomly (coherent) distributed particles on a grain boundary in the bulk material is given in equation 3, which shows the retarding pressure (P_z, Zener pinning pressure) discussed above

$$P_Z = \frac{3F_V\gamma}{2R} \tag{3}$$

where F_V is the volume fraction of randomly distributed spherical particles and γ is the grain boundary potential energy. [7]

2. The Stainless Steels of this work

Table 2.1: *The chemical compositions of the different samples, see appendix A for more thorough information.*

	304 (wt%)	**316 (wt%)**	**321H (wt%)**	**347H (wt%)**
Cr	18.35	16.54	17.13	17.26
Ni	8.01	9.92	9.00	9.16
C	0.038	0.027	0.046	0.053
Mn	1.16	1.29	1.06	1.42
P	0.030	0.031	0.030	0.029
S	0.003	<0.001	0.003	<0.001

Si	0.46	0.51	0.46	0.35
Nb	-	-	-	0.66
Ti	-	-	0.35	-
N	0.057	-	0.010	-
Mo	0.29	2.02	0.32	0.37
Fe	Balance	Balance	Balance	Balance

Table 2.1 shows the investigated stainless steels, two conventional stainless steels (304 and 316) and two new high temperature stabilized stainless steel (321H and 347H). See Appendix A for more detailed information. These stainless steels will be discussed in this chapter.

The 304 alloy is a versatile and a widely used stainless steel with carbon content between 0.04-0.10% for optimum resistance to chromium and carbide sensitization.
[7]

316 is a molybdenum stainless steel and is considered to have an improved resistance to corrosion in comparison to 304, given moderately corrosive environments. However, 316 perform worse than 304 in acidic environments. [7]

The stainless steel of the type of 321H has a high resistance to corrosion in the sensitization temperature region (approximately 425-800°C). This is due to its particles. 321H is developed for higher resistance at temperatures above 540°C, compared to 304 and 316. [10]
347H has been stabilized with NbC particles to have excellent sensitization resistance in the characteristic temperature range of 425-800°C, as is the case with 321H. Its toughness is not exclusive to the high temperature range, since it has a good low temperature toughness. It is although developed for high temperature applications, >540°C. [11]

2.1 Titanium Carbide, TiC

The nucleation of TiC particles in 321H stainless steel, creates a generally better high temperature material. TiC is a stable ceramic. Addition creates a higher tensile strength at higher temperatures, due to the load bearing properties of the TiC hindering dislocational motion (see Zener’s drag section 1.8). Given these positive aspects, there is a negative perspective to these particles if they occur in an excess amount. The appearance of these particles occurs at 600-800°C and lowers the ductility of the material significantly. There are high residual stresses introduced into the material because of this precipitation and hence reducing the strength in comparison to the even higher theoretical strength of the material.
[12]

TiC in a stainless-steel matrix increases the resistance to sensitization, to minimize the sensitization the goal is to bind up as much carbon as possible in the coherent TiC particles. This is done through the nucleation process, catalyzed by heating. [13]

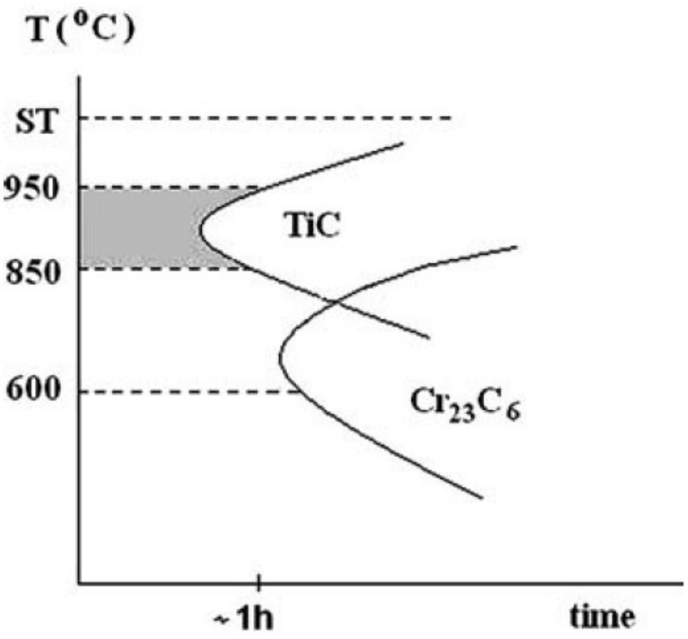

Figure 2.1: *Precipitation behavior for 321H particles, showing optimum temperature (850-950°C) for TiC precipitation.* [13]

The heating increases the prevalence of the TiC and hence decreases the possibility for sensitization up to 950°C, given 1 h exposure, see figure 2.1. After that temperature, the TiC loses its coherency with the matrix. When heat treating the stainless steel above 950°C the material is depleted of titanium which may allow for sensitization at lower temperature.

The precipitation can be described with these equations 4 and 5

$$\ln[\mathrm{Ti}]\,[\mathrm{C}] = 8.86 - \frac{24236}{T},\, T \geq 1155\ K \tag{4}$$

$$\ln[\mathrm{Ti}]\,[\mathrm{C}] = 8.86 - \frac{23808}{T},\, 298 < T < 1155\ K \tag{5}$$

where [X] is soluble amount in wt% of the specific element and *T* is the temperature. [13]

2.2 Niobium Carbide, NbC

NbC precipitation increases strength during long term exposure to high temperatures. The spheroidal particles have a low interfacial energy due to its semi-coherency to the matrix and works to pin the material matrix of stainless steel. NbC are insoluble due to its high melting temperature.

During ageing, secondary nanosized NbC can be prevalent surrounding the dislocations of the material. Secondary NbC phase particles generally as a function of time. This provides a large obstacle for the migration of the dislocations within the material, which causes material failure.

NbC coarsening rate (causing incoherency) is small since the diffusion rate of Nb-atoms in an austenitic matrix is slow. This creates depleted regions of Nb in the matrix surrounding of the

NbC particles. This further slows down the coarsening rate. This also means the secondary precipitation of NbC particles are drastically slowed down. [14]

Stabilizing the stainless steel through precipitation of NbC is normally conducted in the temperature range 800-925℃. Recrystallization of stainless steel 347H (containing NbC precipitates) as well as uncontrolled precipitation of NbC occurs at 1050℃. [15]

3. Method

The general methods used in this report are described here. The characterization methods using a light optical microscope (ASTM E112-10), Scanning Electron Microscope (EDX) and X-ray diffraction.

The investigation will contain deformations and that will be induced using a tensile tester, which will also be described in this chapter.

3.1 Grain Size

Grain size was investigated optically using a microscope and the ASTM E112-10 method.

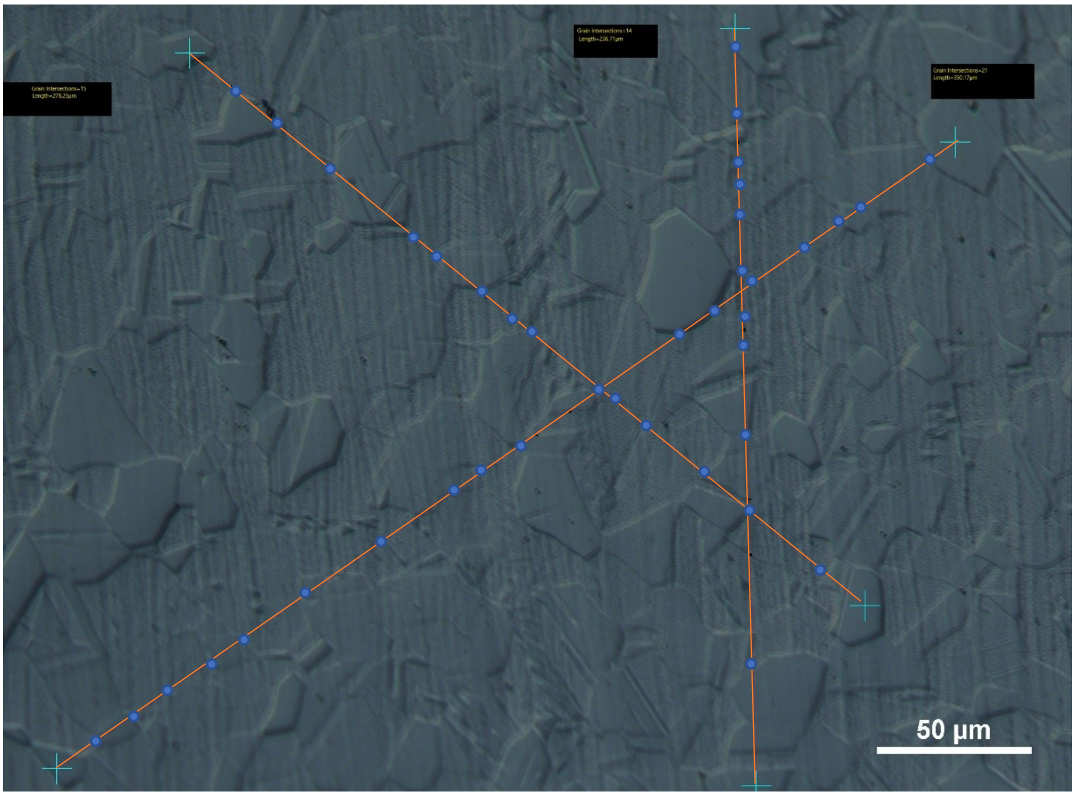

Figure 3.1: *An example of the ASTM E112-10 in practice, which is drawing three lines and noticing the grain boundaries*

Figure 3.1 illustrates grain size calculation and it was obtained through the methodology of ASTM E112-10. This is done through drawing three lines at random on the sample. This is to be able to observe the small grain boundaries on the sample as well as other interesting details. The grain boundaries are noted on the line, and then the length of the line is divided by the amount of grain boundaries. This is done three times (as noted) to obtain a statistically adequate measurement of approximate grain diameter.

3.2 Scanning Electron Microscope, SEM

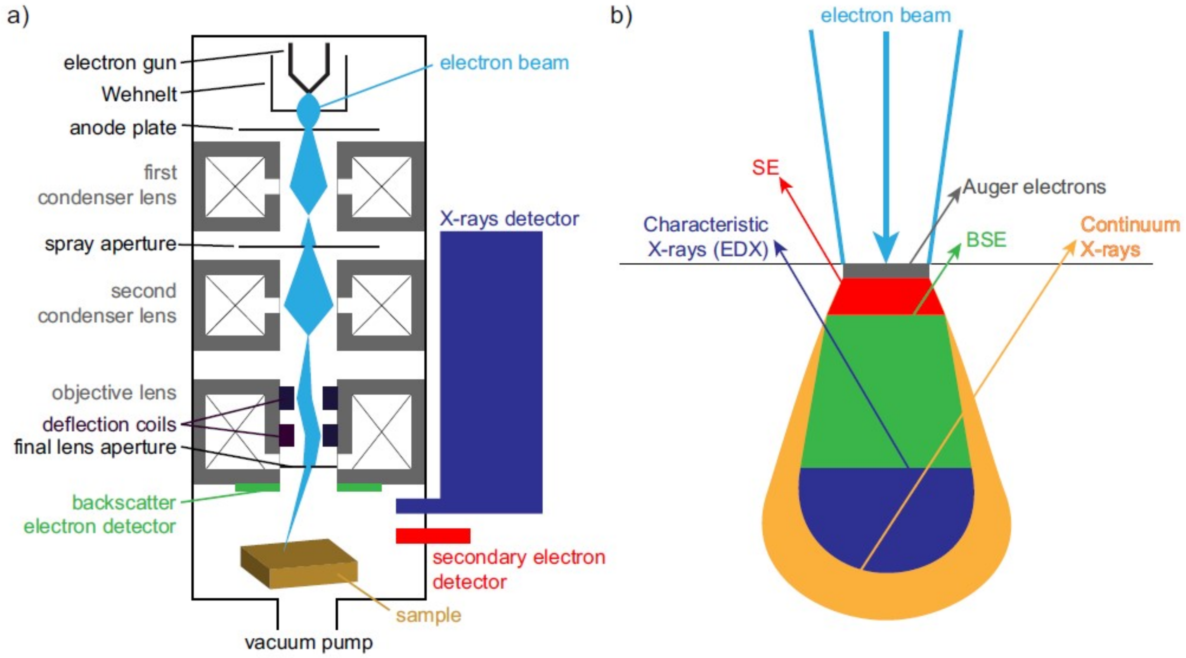

Figure 3.2: *a) A schematic of a SEM microscope b) The excitation volume generated by an electron beam and the corresponding signals generated.* [16]

Figure 3.2 shows a schematic Scanning Electron Microscope, SEM. The purpose of SEM is to produce high resolution images of surfaces. Images magnified beyond the limits of optical microscope. This is due to the low wavelength of the electrons interacting with the sample. The comparatively low wavelengths of light needed to match the electrons wavelength in a SEM does not interact strongly enough with matter to be feasible for imaging thin samples.

The electron gun accelerates a narrow divergent beam, typically 0.1-5 nm in diameter, of electrons towards the sample. This probe area then generates several different signals (figure 3.2b). One signal detected is the elastically scattered electrons are called BSE, Back-Scattered Electrons. The elastically BSE provide a chemical composition contrast, because of the large effect atomic number has on the elastic scattering. The image is provided by the detector located relatively far away from the sample, next to the final aperture, see figure 3.2. BSE typically have the same energy as the beam, since they are elastically scattered.

The origin of Secondary Electrons, SE, makes their energy significantly lower, this is illustrated by figure 3.2b. SE are generated as ionization products. Closer to the sample is the Secondary Electron detector. These are significantly lower energy electrons than BSE. SE is the electrons which are ejected from the atoms as a result of the interaction with the beam. As a result of the low depth of the SE excitation volume the SE detector is topographically sensitive.

The primary beam of SEM can excite the atoms in the sample, which returns to the ground state by generating an X-ray. This X-ray signal is also known as a characteristic X-ray, which has a characteristic energy corresponding to the drop in electron orbital energy (shells). These are denoted with shell and step. For example, K_α means a drop to the K-shell from the shell above, α signifies one shell drop for the electron, β two etc. Since the difference between these shells are characteristic in atoms, this allows for elemental detection. The detection of these X-rays is known by several abbreviations, abbreviating the same name, Energy Dispersive X-ray Spectroscopy. Examples are EDX, EDS, XEDS, the technique will be referred to as EDX (**E**nergy **D**ispersive **X**-ray Spectroscopy). [16]

3.3 Tensile Testing, Plastic Deformation

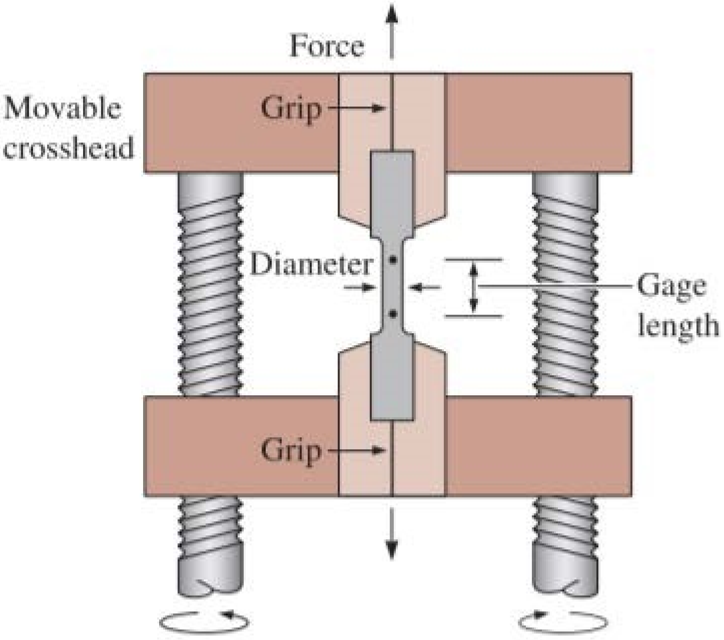

Figure 3.3: *A cross-sectional image of the holder during a tensile test.* [17]

Figure 3.3 illustrates the setup for a tensile test. A tensile test is a common way to deform a material and hence determine its strength. The method is simply pulling the sample in the setup illustrated in figure 3.3. The tensile test generates a stress-stain curve by force application, displayed in figure 3.4. [17]

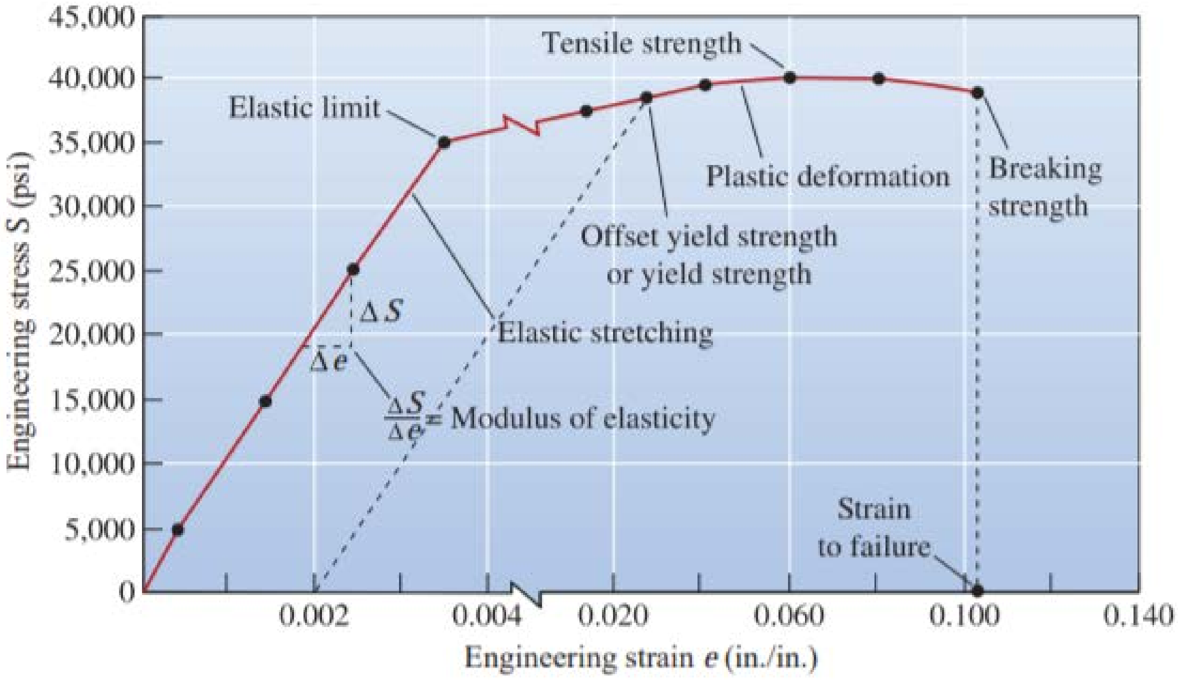

Figure 3.4: *The stress-strain curve of an aluminum alloy* [17]

The figure 3.4 results from the area reduction and elongation of the sample. This characteristic curve has specific sections representing different types of deformation. The material starts deforming elastically, in figure 3.4 up to approximately 35,000 psi (approximately 240 MPa). Until this point the material deforms linearly in accordance with the Modulus of elasticity. If the sample is released during this process, no permanent deformation occurs. Following the elastic limit, the material deforms plastically (permanently), as slip occurs within the microstructure of the material. Usually the elastic limit is not as clear as the one given in the example in figure 3.4. Hence, one usually uses 0.2% elongation. This is known as the yield strength, for determining the start of plastic deformation.

The tensile strength is the maximum stress a material can tolerate before breakage, and the elongation at which the material breaks is the Strain to failure. This is correlated to the movements of dislocations within the structure, which is why grain size matters. The smaller the grains, the more grain boundaries are present to obstruct dislocational motion. At the point of tensile strength, the material exhibits necking, reducing the cross-sectional area and hence the stress tolerance. This is due to the gathering of dislocations. [17]

3.4 X-ray Diffraction, XRD

The characteristic scattering pattern of XRD originates from the interaction between the atom and the incoming beam. The atom acts as a point object when interacting with the X-ray, generating a 3-dimensional wave. This 3-dimensional wave can be considered a plane wave at a sufficient distance (distance of the X-ray detector). A collection of these point objects, as a material matrix with several atomic planes, will therefore create an interference pattern with its collection of wave fronts. Given a perfect periodicity in the material this will generate a sharp diffraction pattern, in similarity to a grating with a specific slit size. This sharp pattern will become blurrier with decreased periodicity in the material. As with a grating, the interference pattern measured as the reciprocal distance between the atomic planes, d, within the material. See equation 8 (Bragg equation) for illustration of the maxima where θ is the diffraction angle, λ is the wavelength and n is an integer. [18]

$$n\lambda = 2d\,sin(\theta) \tag{6}$$

The reflected beam hits the detector at a 2θ angle to the incident beam, hence the data is given as a function of 2θ.

4. Experimental Details

4.1 Polishing

Figure 4.1: *An example of a stainless-steel sample molded into an epoxy puck*

Figure 4.1 illustrates an epoxy puck, containing a stainless-steel sample. To be able to polish the sample, the sample was first cut and molded into epoxy resin as in figure 4.1. For the polishing to result in a flat surface, the sample was placed in the middle of the resulting epoxy puck.

Before polishing grinding with 220 grit grinding paper is required. Following this, polishing is conducted in three different steps. The two following steps using small suspended diamond particles (9 and 3 µm) while polishing. The final step was using OP-S, a liquid containing a suspension of small silica particles for the precise final polish.

4.2 Grain Size

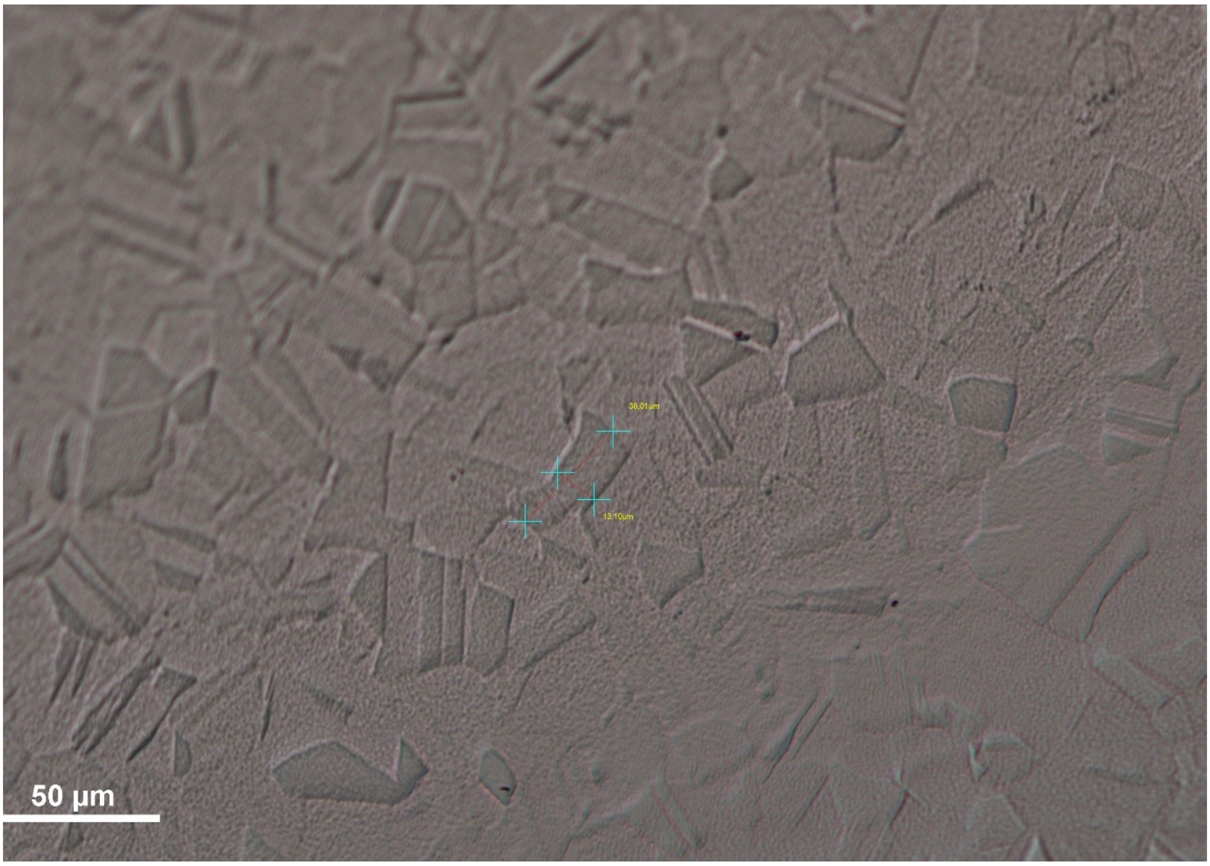

Figure 4.2: *A direct grain size measurement of the planar 304, averaging a grain diameter through measure the length in two different perpendicular directions*

Figure 4.2 shows a grain size determination direct diameter measurement, see Appendix C for all images. This is done through drawing lines on a grain and then using the average as the grain diameter.

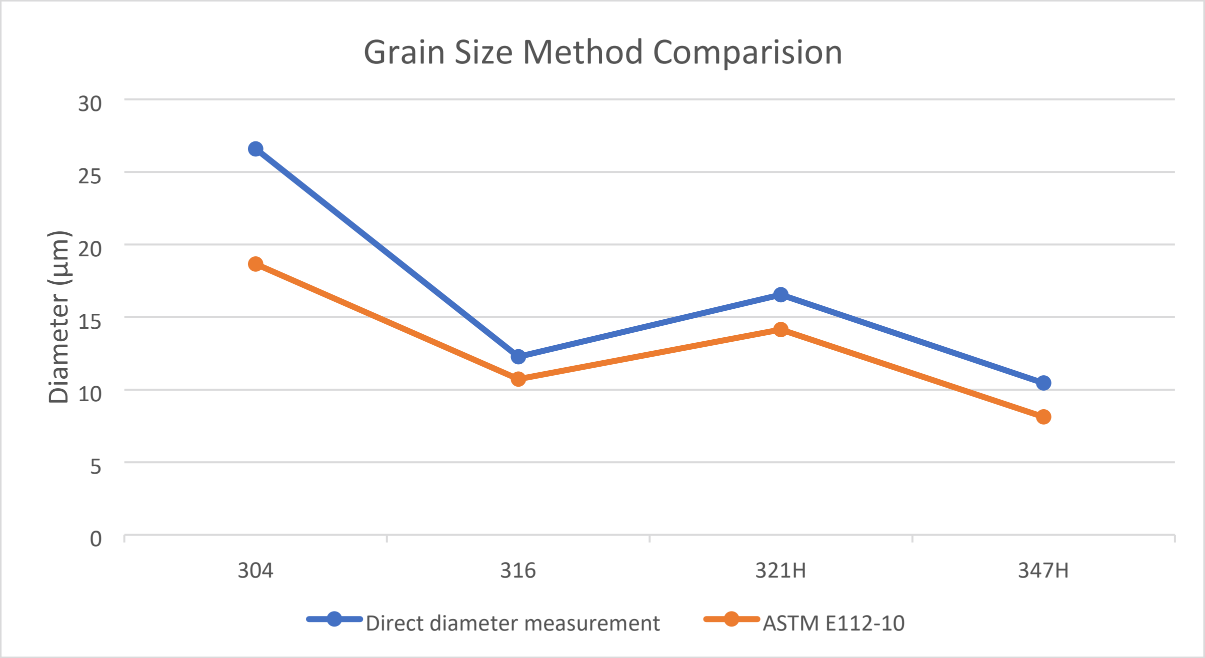

Figure 4.3: *a comparison between the different ways of measuring grain size presented above, see Appendix B and C for the images.*

Figure 4.3 shows the comparison between the direct diameter measurements and the ASTM E112-10. The value obtained from these different methods seems to approximately match up, see figure 9.3 where the samples have been at room temperature. The different methods differ < 10 µm. This is deemed acceptable, and the ASTM E112-10 is deemed an acceptable way to measure grain size at these temperatures. The grain growth on these stainless steels will be further investigated in the result, to obtain the grain growth at Alfa Laval's different brazing cycles. The effect of nitrogen exposure will also be investigated, since it is a common addition during these brazing cycles.

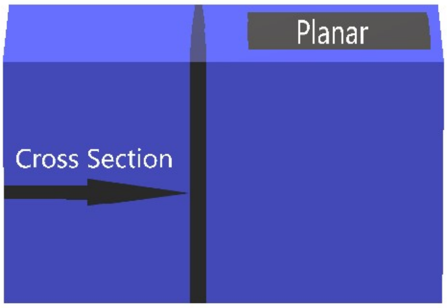

Figure 4.4: *A piece of stainless steel, illustrating the two directions the data was collected in.*

Figure 4.4 illustrates that there are two different directions used; planar and cross-sectional. These directions will be compared for any differential results, relating it to an anisotropic grain size.

4.3 Scanning Electron Microscope, SEM

The primary use of this SEM in this master thesis is to be able to identify the particles, as well as characterizing their composition (using EDX).

4.4 Tensile Testing, Plastic Deformation

Tensile testing was performed on the sample to induce a texture change into the material. This is to investigate whether heat exchangers in operation will benefit or not from the stresses present during manufacturing. The texture change could result in increased grain size, inducing the opposite.

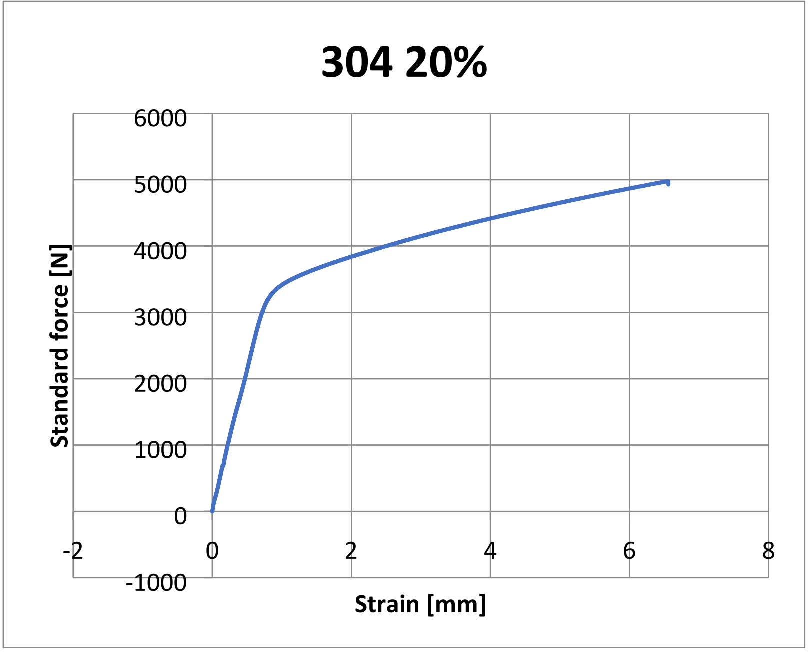

Figure 4.5: *An example of the stress-strain curve generated in the deformation of stainless steel*

Figure 4.5 display the tensile testing which was performed using testXpert, see Appendix G for all tensile tests. This program allowed for automated plastic deformation, in accordance to instructions. Because of the deformations of the stainless-steel during manufacturing (approximately 10-20%), the samples were deformed by 10% and 20% length increase.

4.5 X-ray Diffraction

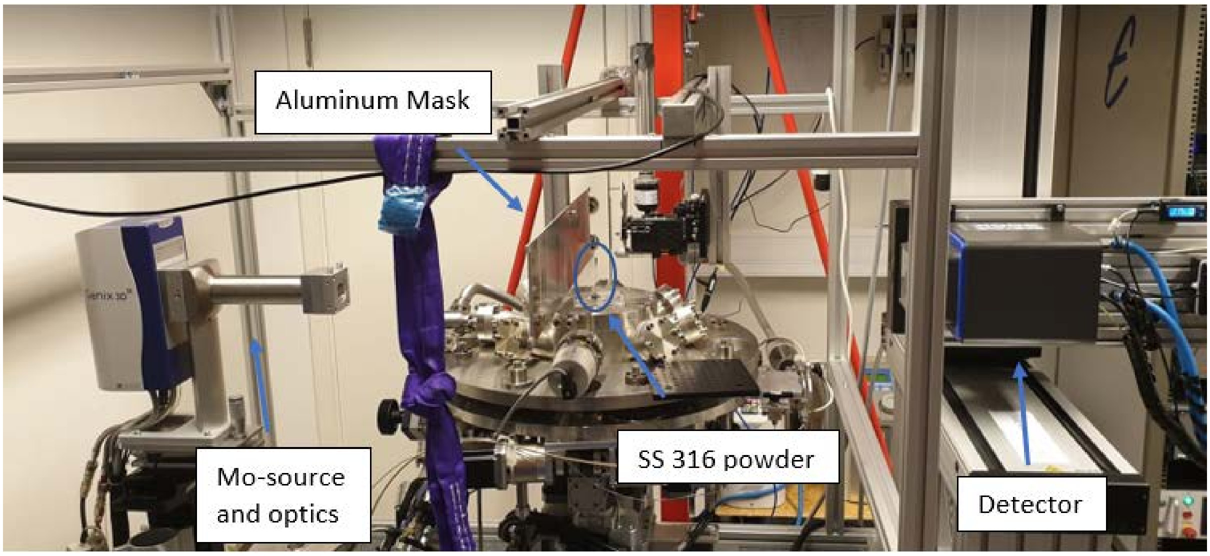

Figure 4.6: *The XRD machine used for the feasibility study of characterizing stainless steel, with a Mo source*

Figure 4.6 illustrates the XRD machine used for the feasibility study which was the one owned by the Division of Synchrotron Radiation Research at Lund's University. This source used was a Mo source with optics to filter the α-radiation, followed by an aluminum mask to protect the detector from scattering the radiation in the air. Behind the mask, the stainless steel 316 powder is in a sample holder. After the diffraction event in the sample, the beam hits the detector. The detector is a CdTe detector with an active detection area of 83.8 × 106.5 mm^2. This area has a detection efficiency of 90%, meaning that 90% of the signal hitting the detector is noted. [19]

5. Results

Following this, the grain growth at the different brazing cycles will be presented. The characterization of the expected particle presence, using both optical and electron microscopes will follow.

The data from heat treatment will also be compared with samples which has been deformed. These samples have been plastically deformed in similarity to the manufacturing of channels of the heat exchangers.

5.1 Heat Treatment

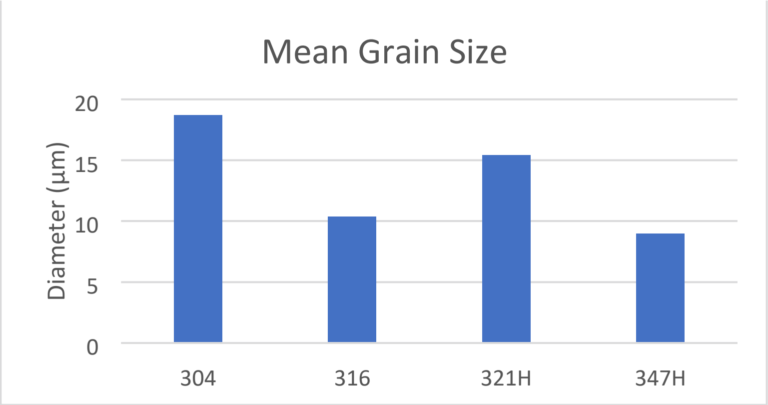

Figure 5.1: *The mean grain size of the before heat treated samples*

Figure 5.1 shows the mean before any heat treatment is performed. The smallest grains exist in 347H, and the largest in 304. The grain size varies from around 10 µm for 347H and 316 up to almost 20 µm for 304. Considering the grain sizes in the order of 100 µm after heat treatments (see below), the size difference of around 10 µm is considered negligible.

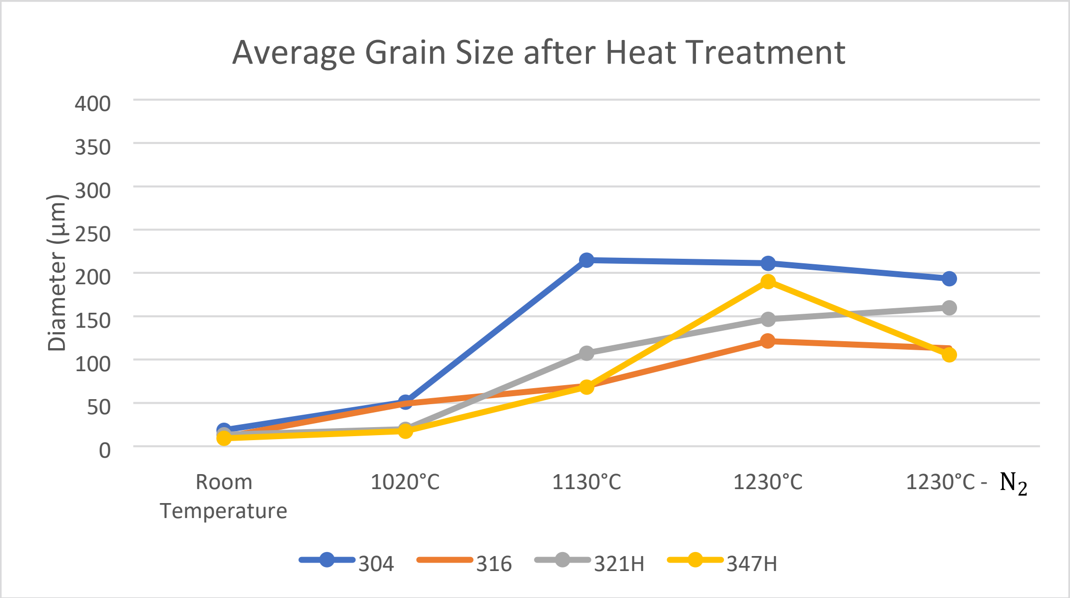

Figure 5.2: *The average grain diameter after heat treatment specified*

Figure 5.2 describes the average grain diameter at the different temperatures characteristic for Alfa Laval's brazing cycle. The last x-axis point is the 1230°C brazing cycle although with exposure to nitrogen gas. All was conducted using ASTM E112-10 method. New high temperature stainless steel does generate a lower grain size at temperatures equal or lower than 1020°C. There seems to be a vast grain growth no matter the type of stainless steel above 1020°C. However, the type which exhibits most growth is 304.

The effect of the nitrogen atmosphere during annealing is insignificant, except for 347H, where it significantly lowers the grain size in accordance with the theory.

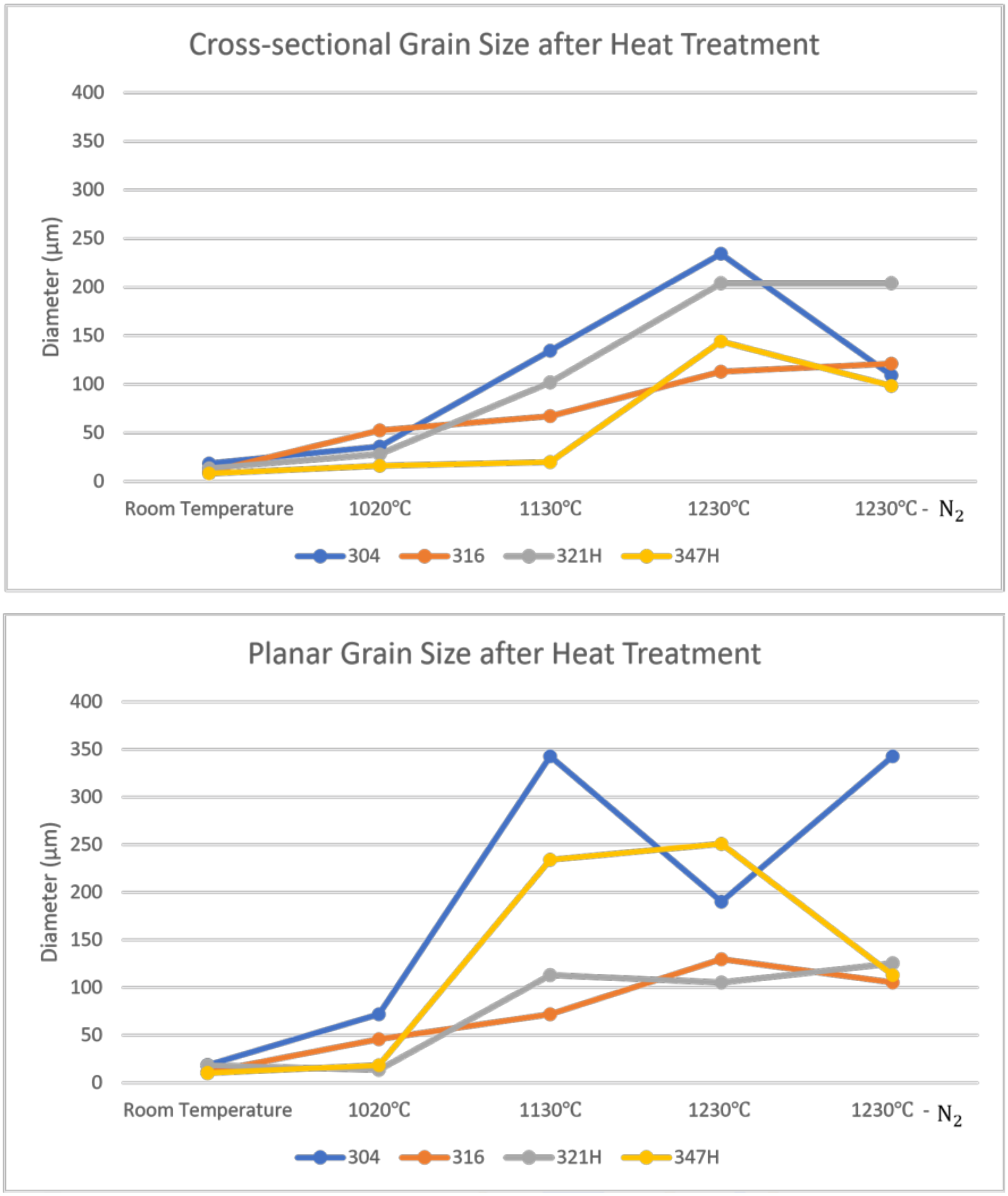

Figure 5.3: *The cross-sectional (up) and planar (down) grain diameter of the grains at different heat treatment temperatures*

Figure 5.3 shows the different directions during heat treatment. It illustrates that the high temperature stabilized stainless steels (321H and 347H) generally performing better ≤ 1020 °C in the different directions as well.

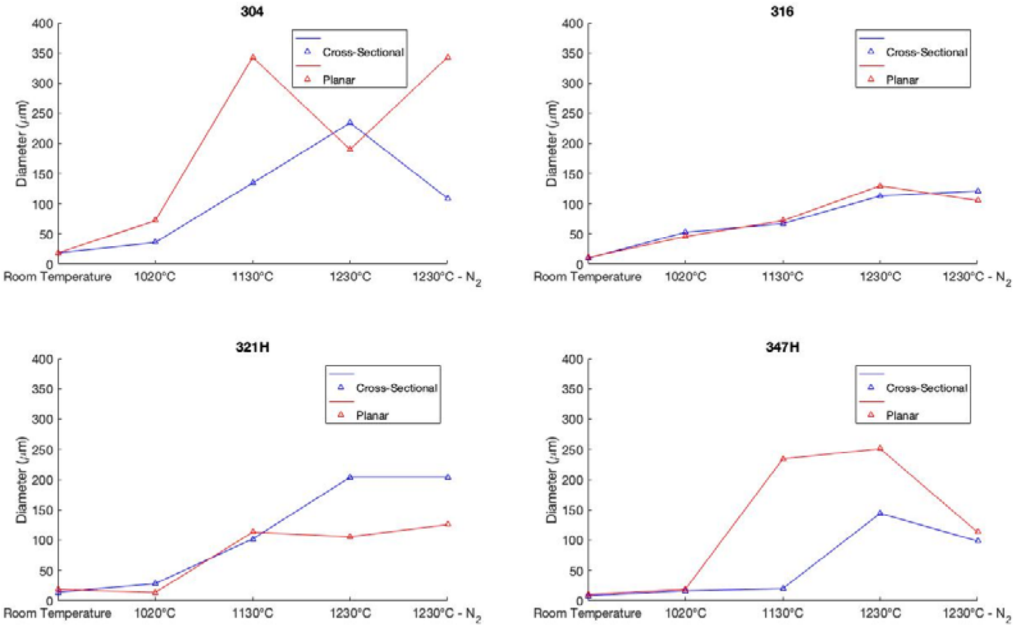

Figure 5.4: *Illustrations of the difference in the different directions in the different stainless steels, after heat treatment*

Figure 5.4 illustrate significant anisotropy in 304 & 347H at higher temperatures than 1020°C. There is some anisotropy in 321H at higher temperatures as well, however it is significantly less than in 304/347H.

When observing 304 planar there is a clear difference in grain size in the opposite direction than one might expect. This might be explained by the vast growth of the 304 grains up to 1230°C, see figure 10.4. If the measurement point is used investigating very large grains, the result may not be representative. This is because the random measurement of an area containing a grain boundary will become even more significant as the grains grow. This might be the case for 304, since the stainless-steel exhibit a vast grain growth. Hence, the 304 planar data point might not be representative. For the images investigated in heat treatments, see Appendix D.

5.2 Plastic Strained Samples

The grain sizes are larger in the strained samples, especially for 316 and 321H. The large grain growth of 316 and 321H decreases substantially when increasing plastic deformation from 10% to 20%. See Appendix G for all of the tensile tests and subsequent images.

5.3 Particles

There is significant information to consider in the precipitation of the particles, which will be investigated in this chapter. Information such as size, composition and precipitation amount of the particles may have large effects on the annealing behavior.

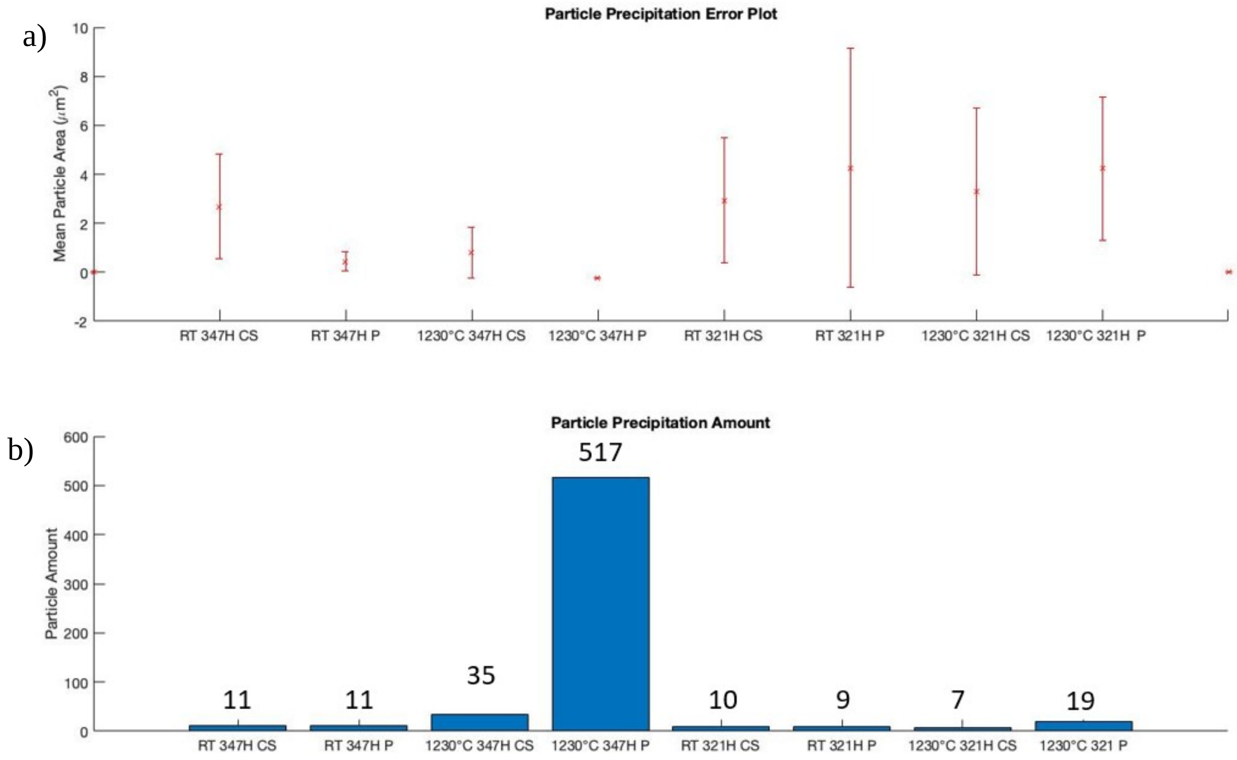

Figure 5.7: *An errorplot illustrating the mean particle area as well as the standard error of the measurements, as well as a bar plot showing the number of particles. RT = Room Temperature, CS = Cross Sectional and P = Planar. Appendix E shows particles and their size.*

Figure 5.7a is an errorplot of the mean particle area with the standard error and particle precipitation, showing a general lack of particle growth. 347H even seems to decrease its general mean particle area, however only statistically significant in 347H planar. This was done through measuring particle area on 2 different parts of the sample, see Appendix E. Figure 5.7b also shows the number of particles present on the sample. This seems to show an increased nucleation of particles in 347H, especially in the planar direction.

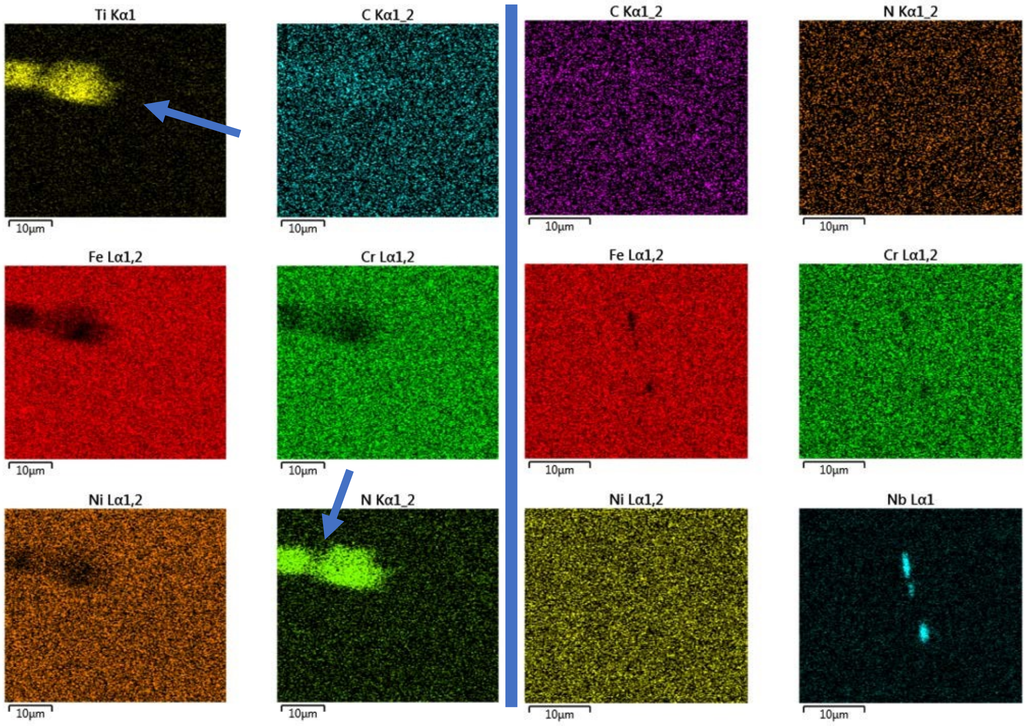

Figure 5.8: *EDX maps of 321H (left) and 347H (right) before a heat treatment at 1230℃. The TiN particle is marked by an arrow*

Figure 5.8 shows the EDX of 321H and 347H without any heat treatment. What is significantly surprising is that the TiC particle in the stainless steel seems to be partially converted to TiN, even before any heat treatment. This could be due to the nitrogen present in the air is adequate for TiC to convert.

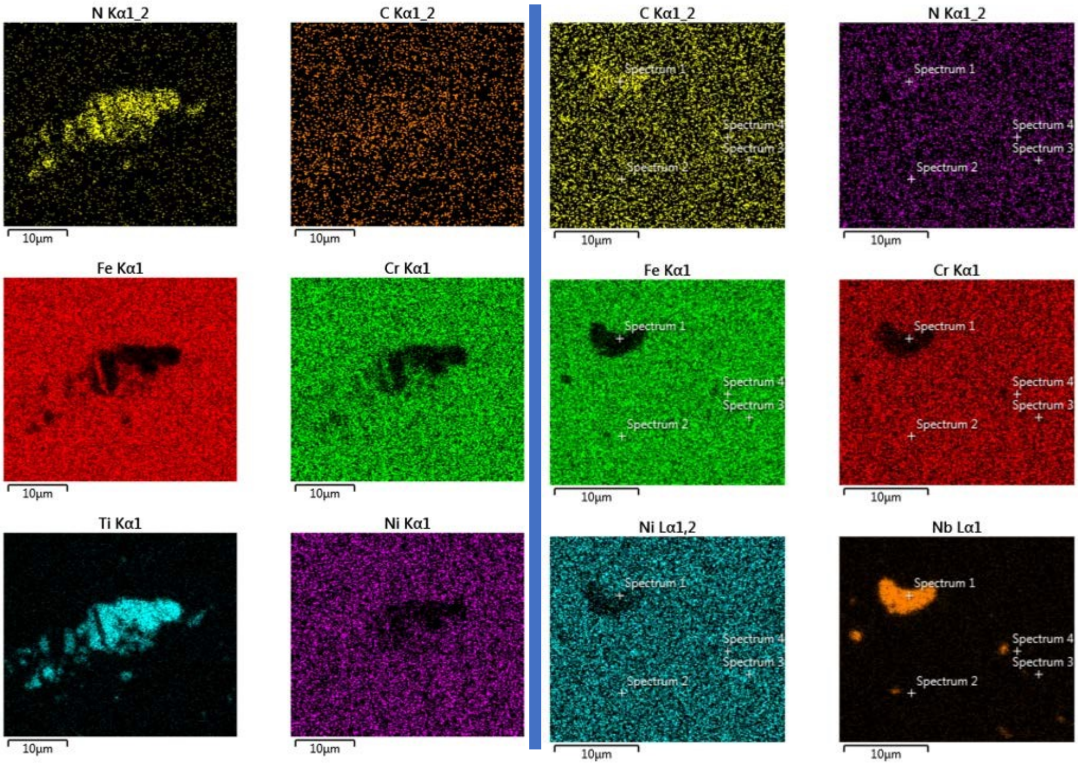

Figure 5.9: *EDX maps of 321H (left) and 347H (right) after a heat treatment at 1230℃ meanwhile exposed to N_2-gas*

Figure 5.9 shows the elemental distribution within the material of 321H and 347H after heat treatment at 1230℃ with exposure to nitrogen gas. The 347H have clear NbC particles and 321H has TiN particles.

The distribution of the precipitating particles in 321H and 347H is investigated through a normplot, where the red line is a perfect normal distribution in the different samples. It is important that the growth is normally distributed, since that means that the measured particle size is representing all precipitating particles within the sample. To reduce the dimensional effect of the particle's growth in three dimensions (and measuring area in two), the data is logarithmized. This is by using a natural logarithm (ln) on the data point. See figure 10.10 for the total normplotts of 321H and 347H.

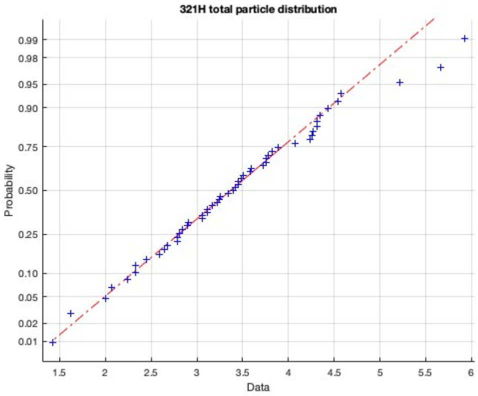

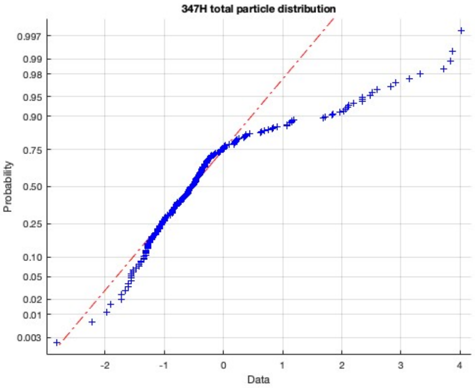

Figure 5.10: *321H (left) and 347H (right) logarithmic normplot for all datapoints, regardless of heat treatment.*

In figure 5.10 347H do illustrate a lack of normal distribution. This figure may be interpreted to be normally distributed in the central 50% of the values, although I do not find that adequate. Figure 5.10 shows 321H to nucleate particles in a normal distribution. This is even though the particles are from directions (cross-sectional and planar) as well as different brazing cycles (Room Temperature and 1230℃). This may indicate a somewhat more inert growth reaction to an increased temperature and direction from the particles.

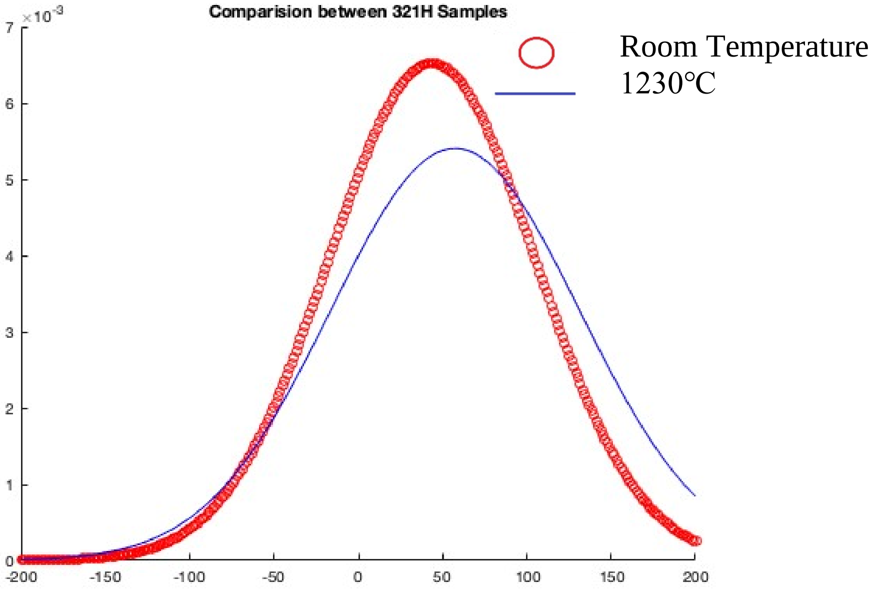

Figure 5.11: *The normal distributions generated for heat treatment at 1230*℃ *compared with the non-heat treated samples (room temperature)*

As figure 5.11 illustrates, the normal distributions are very similar. Hence, combining the data creates an adequate normal distribution for a normplot not being able to distinguish between them. This further gives evidence for a more inert growth mechanism when it comes to added particle nucleation.

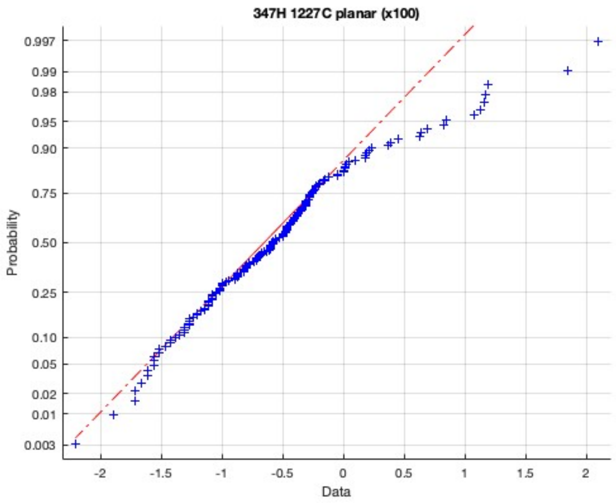

Figure 5.12: *The particle distribution in a planar sample which has been exposed to*

1230°C and N_2-gas, one example of the normplotts

Figure 5.12 and the other normplotts in Appendix F, display that all of the samples illustrate a distribution in accordance with a logarithmic normally distributed nucleation of particles. However, some of the samples (figure 5.12 for example) have a more left-screwed distribution (lack of larger particles). This could either be explained by Ostwald Ripening or the Gibbs-Thompson effect.

The fact that the sample data overall follows a logarithm normal distribution gives security to the fact that the measurements have been correctly performed.

5.4 X-ray Diffraction

Figure 5.13 displays the diffractogram produced for stainless steel 316 powder compared with a few reference diffractograms [24,25,26].

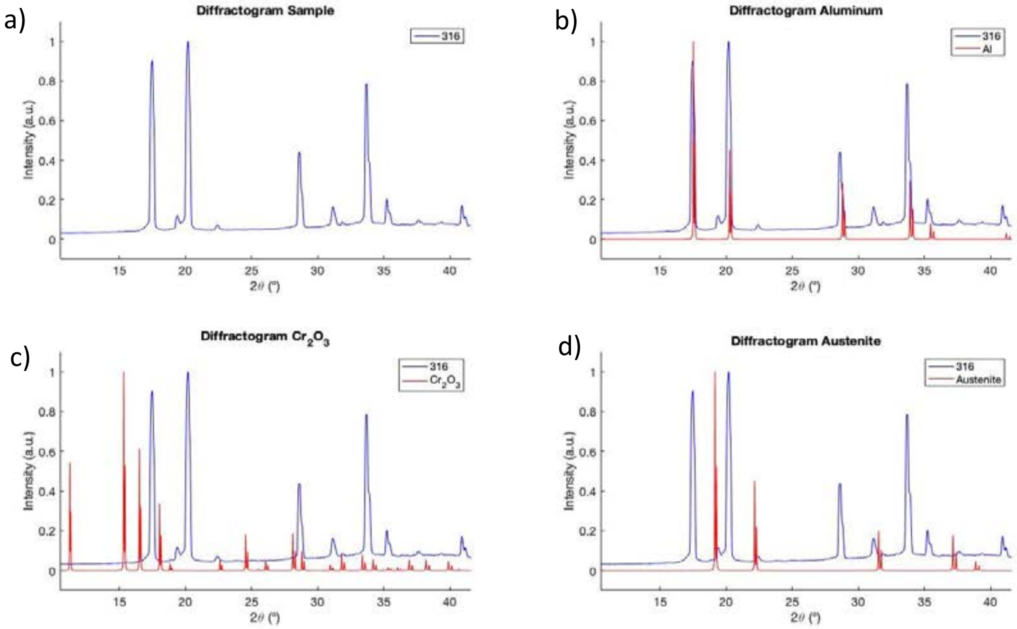

Figure 5.13: *The data generated from an 8 mmwide capillary od 316 powder, a), compared to reference diffractogram of; b) Aluminum c) Cr_2O_3 and d) Austenite*

Figure 5.13b explains most of the large peaks through scattering events by the aluminum mask. The Chromium oxide reference diffractogram in figure 5.13c does not match at all, most significantly there are no peaks at the characteristic 11° and 15°. It is however clear that the sample is in the beam path since the austenitic peaks are visible in figure 5.13d.

6. Discussion

The grain size increased in all of the samples, however the new high temperature stainless steels (321H/347H) show a smaller grain size after heat treatment up to 1020°C due to its particle precipitation. Three of the samples (304/321H/347H) exhibited anisotropy during the different brazing temperatures (1020°C, 1130°C, 1230°C). 347H sticks out due to showing a significant decrease in grain size when deformed and when heat treated with nitrogen gas. 347H seems to increase its precipitation of particles when heat treating at high temperatures (1230°C). Investigation of 316 native oxide did not resolve any signal using XRD. In this chapter, these results and the possible interpretations will be discussed further.

6.1 Grain size Microstructure

The differences in texture between these stainless steels will generate different responses to high temperature, which will in turn affect the annealing behavior. The texture (total crystallographic directions) in stainless steel clearly depends on the direction. This can also explain the anisotropy present at the highest temperature brazing cycles in 304 and 347H. What is clear is that the new high temperature stabilized stainless steels (321H/347H) have significantly smaller grains ≤ 1020°C than the conventional stainless steel (304/316).

6.2 Nitrogen Gas Effect

Nitrogen gas, which should act as a grain refiner, does have significant effect at the 1230°C heat treatment for 347H. However, for the other stainless steels, nitrogen does not seem to have a grain refining effect. It is possible that the grain refining effect of nitrogen is too small at 1230°C (for 304/316/321H). It is possible that the particles of 347H immobilizes the grain growth and hence the effect of nitrogen may be more significant. 321H particles might not contribute in the same way due to its transformation from TiC to TiN. The possible incoherence of TiN may be why they do not inhibit the grain growth in the same way that the NbC particles do.

Another case for why the nitrogen exposure may be more grain refining in 347H than the other stainless steel is the chemical composition of 347H. 347H has no nitrogen content, which might mean that a larger content nitrogen is absorbed into 347H.

6.3 Plastically Deformed Samples

In any heat exchanger manufacturing process, some deformation of the stainless steel will occur. Most significant, the channels are deformed from a solid piece of stainless steel.

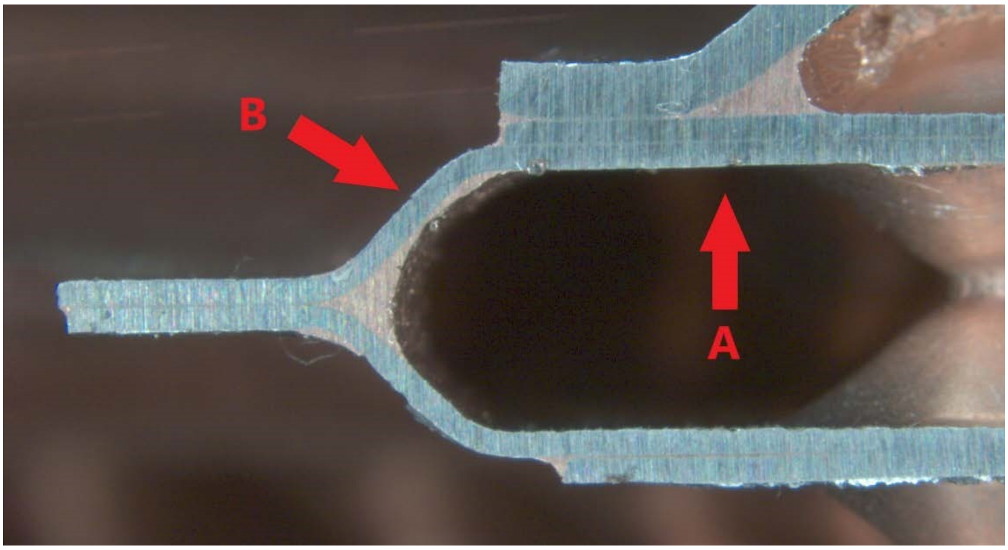

Figure 6.1: *The edges on the channels of a heat exchangers. A: The flat part, B: The curved part.*

Figure 6.1 shows flat part (A) and the deformed (B) of a heat exchanger. The deformed part is plastically strained in the range of the investigation, 10-20%. The results show that deformation will result in smaller grains in 347H and larger grains in all of the other stainless steel samples. This means that 347H will be mechanically more durable than the other stainless steel in the deformed part of a heat exchanger. 304 does theoretically have the least difference in grain size between these (A & B) and specifically for the brazing cycle of 1230 °C.

6.4 Anisotropy

The results clearly show that there is different grain growth in different directions for 304, 321H and 347H. 304 and 347H has the most significant anisotropy, in similarity to the previous section. This means that the in a flat part of the heat exchanger, the grain size will largely depend on what direction the stainless steel is observed in. For 321H the anisotropy is only clear at the highest temperature brazing cycle (1230°C).

6.5 Particles

321H lacks significant TiC precipitation after heat treatment at 1230°C. This despite that the stainless steel should precipitate TiC until the titanium content in the material matrix is depleted (see section 2.1). This might be due to insufficient annealing time. This will however also be positive since this probably means no lack of coherency. On the other hand, the particles do not seem to obstruct grain boundary movement (grain growth) at this temperature either. Hence, the purpose of the coherency seems to be lost.

NbC is insoluble and that might contribute to the increased precipitation at 1230°C heat treatment in 347H. NbC's semi-coherency with the matrix may be lost in an possible coarsening of the large particles. This could be a result of the high diffusion rate catalyzed by the high temperature in this heat treatment (1230°C). The stabilizing temperature for NbC is 800-925°C, therefore there might be an abnormal high diffusion rate in this heat treatment.

That might be why the 347H seems to exhibit grain growth above the temperature of 1020℃. The coarsening will cause NbC to lose its stabilizing effect. The loss of coherency with the matrix may also be why the size of the NbC particles seem to stagnate in their growth, due to the smaller coherent particles absorbing all of the precipitating matter and hence become big enough for visibility in an optical microscope.

In section 2.2 the fact is presented that secondary NbC particles nucleates around dislocations, obstructing their movement, as a function of time. This might be why the plastically strained samples exhibit a finer grain structure in 347H. The Zener's Drag results from these particles and their potential growth as discussed above.

6.6 X-ray Diffraction

Although Cr_2O_3 is known to form at the surface of stainless steels, we could not see any corresponding XRD signal. This may have several reasons.

The Cr oxide is a native oxide formed when the material is exposed to air, typically at room temperature. This probably results in a rather poorly ordered crystal structure, with broad diffraction peaks. Furthermore, the oxide is only a few nm thick, and the amount of material contributing to the corresponding diffraction pattern is significantly smaller than for the bulk of the steel. Considering the low signal from the austenitic steel phase, it is hence not very surprising that the Cr oxide signal is too low to be detected.

A major reason for the generally low signal seems to be that the Al mask was misplaced and therefore blocked most of the beam. A repetition of the measurements was planned but was obstructed by the outbreak of the Covid-19 pandemic.

The XRD method is concluded to be adequate to investigate stainless steel, since lines are visible. However, future work may be needed to investigate how to increase the oxide signal to generate a signal.

7. Conclusion

The new stabilized stainless steel (321H/347H) exhibit significant less grain growth than the conventional stainless steels (304/316) during a brazing cycle ≤1020℃: This combined with that 347H has less grain growth during nitrogen exposure and deformation makes 347H the optimal choice for usage in a heat exchanger.

347H reaction to heat treatment might be attributed to increased precipitation of particles, obstructing grain growth by Zener's drag. Even though 321H have less grain growth than the conventional stainless steels the particles do not seem to be as preventative to grain growth as the NbC-particles are in 347H.

The grain growth shows anisotropical behavior for 347H and 304, which is significant for failure investigation since the grain size will depend on the direction investigated.

X-ray diffraction can detect a signal of the austenitic stainless steel, however more improvements are needed for the oxide to be resolved. More specifically, the signal to noise ration needs to be improved and the aluminum mask needs to be moved from the beam path.

The XRD signals and intensity which need classification, to be able to draw more conclusions about the diffractogram would need further studies. Further, the signal to noise ration needs an increase to be able to resolve the oxide signal.

8. Future Work

This Master thesis has investigated the deformational effect on grain growth, however only in the planar direction. What could be interesting is the deformational effect in the different directions; planar and cross-sectional. Further interest is in whether grain growth is catalyzed in lower deformations than 10% for 347H.

The effect of nitrogen exposure during a heat treatment cycle was investigated and compared to the same cycle without the nitrogen. 1230℃ does however catalyzes grain growth to a large extent, hence the grain refining effect will be more negligible in that context. To further investigate the grain refining effect, nitrogen exposure at lower temperatures might give interesting results.

The particles have been counted and analyzed, however, to be able to investigate the coherency (chemical bonding) of the particles and their effect on heat treatment would be interesting. The stagnation of 347H growth would also be of interest.

References

[1] Lacome, P., Baroux, B., Beranger, G., 1993, “Stainless Steels”, Les Editions de Physique, France

[2] Jernkontoret, 2020-09-03, “HYBRIT – fossilfri stålproduktion”, source: https://www.jernkontoret.se/sv/vision-2050/koldioxidfri-stalproduktion/# , collected: 2020-09-07

[3] Jessen, C.Q., 2018, “*Stainless steel, - Handbook for the curious*”, Damstahl, Denmark

[4] Alfa Laval; “*Our Company*”, source: https://www.alfalaval.com/about-us/our-company/, collected: 2020-05-11

[5] Dotton, J.A., ”*Face Centered Cubic Structure*”, source: https://www.eeducation.psu.edu/matse81/node/2133, collected: 2020-08-26

[6] The Welder, “Metallurgy Matters: Carbon content, steel classifications, and alloy steels”, source: https://www.thefabricator.com/thewelder/article/metalsmaterials/carbon-contentsteel-classifications-and-alloy-steels, collected: 2020-05-11

[7] Humphrey, F.J., Hatherly, M., 2004,” Recrystallization and Related Annealing Phenomena Second Edition”, Elsevier, United Kingdom

[8] Klok, O., Lambrinou, K., Gavrilov, S., Stergar, E., Lim, J., Van der Donck, T., Van Renterghem, W., De Graeve, I., “Effect of deformation twinning on dissolution corrosion of 316L stainless steels in contact with static liquid lead-bismuth eutectic (LBE) at 500°C”, Journal of Nuclear Materials 510 (2018) 556-557.

[9] ScienceDirect, “Grain Growth”, source: https://www.sciencedirect.com/topics/materialsscience/grain-growth, collected: 2020-05-11

[10] Sandmeyer Steel Company, “Alloy 321/321H”, source: https://www.sandmeyersteel.com/321-321H.html, collected: 2020-05-11

[11] Sandmeyer Steel Company, “Alloy 3471/347H”, source: https://www.sandmeyersteel.com/347-347H.html, collected: 2020-05-11

[12] Grzesiak, D., AlMangour, B., Krawczyk, M., Baek, M., Lee, K., 2019, “Selective laser melting of TiC reinforced stainless steel nanocomposites: Mechanical behaviour at elevated temperatures”, Volume 256, Elsevier, Material Letters

[13] Moura, V., Kina, A.Y., Souto Maior, S., Lima, L.D., Mainier, F.B., 2006, “Influence of stabilization heat treatments on microstructure, hardness and intergranular corrosion resistance of the AISI 321 stainless steel”, 5TH BRAZILIAN MRS MEETING, Springer Science+Business Media

[14] Zhao W.X., Zhou D.Q., Jiang S.H., Wang H., Wu Y., Liu J., X.Z. Wang, Lu Z.P., 2018,

“Ultrahigh stability and strong precipitation strengthening of nanosized NbC in aluminaforming austenitic stainless steels subjecting to long-term high-temperature exposure”, Volume 738, Materials Science and Engineering: A, Elsevier

[15] Gómez X., Echeberría J., Microstructure and mechanical properties of low alloy steel T11–austenitic stainless steel 347H bimetallic tubes

[16] Rullik L., 2018. “*Industrial Alloys Studied by Surface Sensitive Techniques*” Lund: Fysiska institutionen, Lunds universitet.

[17] Askeland R.D., Fulay P.P., Wright W.J., 2011,” The Science and Engineering of Materials”, Stamford, Cengage Learing

[18] Als-Nielsen, J., McMorrow, D., “Elements of Modern X-ray Physics”, United Kingdom, Wiley

[19] Dectris, “PILATUS3 R CdTen 300K”, source: https://www.dectris.com/products/pilatus3/pilatus3-r-cdte-for-laboratory/pilatus3-r-cdte-300k/, collected: 2020-08-31

Appendix A

The samples consist of several stainless steels, see the following four tables, table A.1-A.4. This information has been provided by Degerfors Laboratories.

Table A.1: *The chemical composition of 347H*

Element	Content (wt%)	Uncertainty of Measurement (%)	Accredited range of measurement	Standard Method
C	0.053	0.03	0.0020 - 5.0	ASTM E 1019-18
Si	0.35	*		ASTM E 572-13
Mn	1.42	*		ASTM E 572-13
P	0.029	0.004	0.002 - 0.1	ASTM E 1086-14
S	<0.001	*	0.0010 - 0.35	ASTM E 1019-18
Cr	17.26	*		ASTM E 572-13
Ni	9.16	*		ASTM E 572-13
Mo	0.37	*		ASTM E 572-13
Ti	<0.003	*		ASTM E 572-13
Nb	0.66	*		ASTM E 572-13
Cu	0.32	*		ASTM E 572-13
Co	0.15	*		ASTM E 572-13
N	0.032	0.002	0.0002 - 0.50	ASTM E 1019-18
Sn	<0.02	*		ASTM E 572-13
W	0.04	*		ASTM E 572-13
V	0.050	*		ASTM E 572-13
Al	0.004	*	0.01 - 1.3	ASTM E 1086-14
Ta	0.004	*		ASTM E 1086-14
Ca	0.0004	*		ASTM E 1086-14
B	0.0002	0.0001	0.0002 - 0.012	ASTM E 1086-14
As	0.004	0.0005	0.001 - 0.030	ASTM E 1086-14
Fe	70.07	*		ASTM E 1086-14

Table A.2: *The chemical composition of 321H*

Element	Content (wt%)	Uncertainty of Measurement (%)	Accredited range of measurement	Standard Method
C	0.046	0.03	0.0020 - 5.0	ASTM E 1019-18
Si	0.46	*		ASTM E 572-13
Mn	1.06	*		ASTM E 572-13
P	0.030	0.004	0.002 - 0.1	ASTM E 1086-14
S	0.003	*	0.0010 - 0.35	ASTM E 1019-18
Cr	17.13	*		ASTM E 572-13
Ni	9.00	*		ASTM E 572-13
Mo	0.32	*		ASTM E 572-13
Ti	0.35	*		ASTM E 572-13
Nb	0.008	*		ASTM E 572-13
Cu	0.33	*		ASTM E 572-13
Co	0.16	*		ASTM E 572-13
N	0.010	0.002	0.0002 - 0.50	ASTM E 1019-18
Sn	<0.02	*		ASTM E 572-13
W	0.04	*		ASTM E 572-13
V	0.10	*		ASTM E 572-13
Al	0.030	*	0.01 - 1.3	ASTM E 1086-14
Ta	0.009	*		ASTM E 1086-14
Ca	0.0004	*		ASTM E 1086-14
B	0.0006	0.0001	0.0002 - 0.012	ASTM E 1086-14
As	0.006	0.0005	0.001 - 0.030	ASTM E 1086-14
Fe	70.89	*		ASTM E 1086-14

Table A.3: *The chemical composition of 316*

Element	Content (wt%)	Uncertainty of Measurement (%)	Accredited range of measurement	Standard Method

C	0.027	0.03	0.0020 - 5.0	ASTM E 1019-18
Si	0.51	*		ASTM E 572-13
Mn	1.29	*		ASTM E 572-13
P	0.031	0.004	0.002 - 0.1	ASTM E 1086-14
S	<0.001	*	0.0010 - 0.35	ASTM E 1019-18
Cr	16.54	*		ASTM E 572-13
Ni	9.92	*		ASTM E 572-13
Mo	2.02	*		ASTM E 572-13
Ti	0.011	*		ASTM E 572-13
Nb	0.009	*		ASTM E 572-13
Cu	0.29	*		ASTM E 572-13
Co	0.27	*		ASTM E 572-13
N	0.046	0.002	0.0002 - 0.50	ASTM E 1019-18
Sn	<0.02	*		ASTM E 572-13
W	0.06	*		ASTM E 572-13
V	0.073	*		ASTM E 572-13
Al	0.004	*	0.01 - 1.3	ASTM E 1086-14
Ta	0.009	*		ASTM E 1086-14
Ca	0.0007	*		ASTM E 1086-14
B	0.0019	0.0001	0.0002 - 0.012	ASTM E 1086-14
As	0.006	0.0005	0.001 - 0.030	ASTM E 1086-14
Fe	68.86	*		ASTM E 1086-14

Table A.4: *The chemical composition of 304*

Element	Content (wt%)	Uncertainty of Measurement (%)	Accredited range of measurement	Standard Method
C	0.038	0.03	0.0020 - 5.0	ASTM E 1019-18
Si	0.46	*		ASTM E 572-13
Mn	1.16	*		ASTM E 572-13
P	0.030	0.004	0.002 - 0.1	ASTM E 1086-14

S	0.003	*	0.0010 - 0.35	ASTM E 1019-18
Cr	18.25	*		ASTM E 572-13
Ni	8.01	*		ASTM E 572-13
Mo	0.29	*		ASTM E 572-13
Ti	<0.003	*		ASTM E 572-13
Nb	0.018	*		ASTM E 572-13
Cu	0.59	*		ASTM E 572-13
Co	0.19	*		ASTM E 572-13
N	0.057	0.002	0.0002 - 0.50	ASTM E 1019-18
Sn	<0.02	*		ASTM E 572-13
W	0.03	*		ASTM E 572-13
V	0.093	*		ASTM E 572-13
Al	0.02	*	0.01 - 1.3	ASTM E 1086-14
Ta	0.006	*		ASTM E 1086-14
Ca	0.0005	*		ASTM E 1086-14
B	0.0003	0.0001	0.0002 - 0.012	ASTM E 1086-14
As	0.005	0.0005	0.001 - 0.030	ASTM E 1086-14
Fe	70.74	*		ASTM E 1086-14

Appendix B

Following figures shows grain size measurements on the four stainless steels at room temperature.

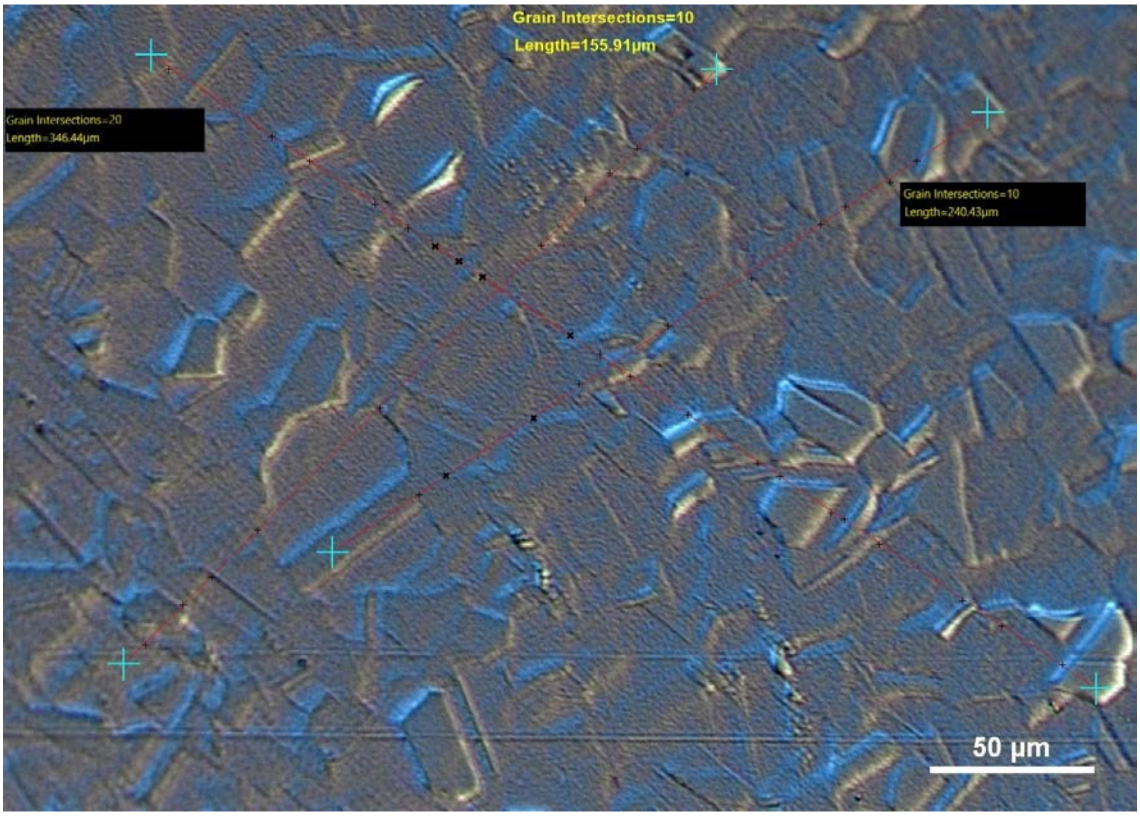

Figure B.1*: 304 stainless steel, planar view at room temperature*

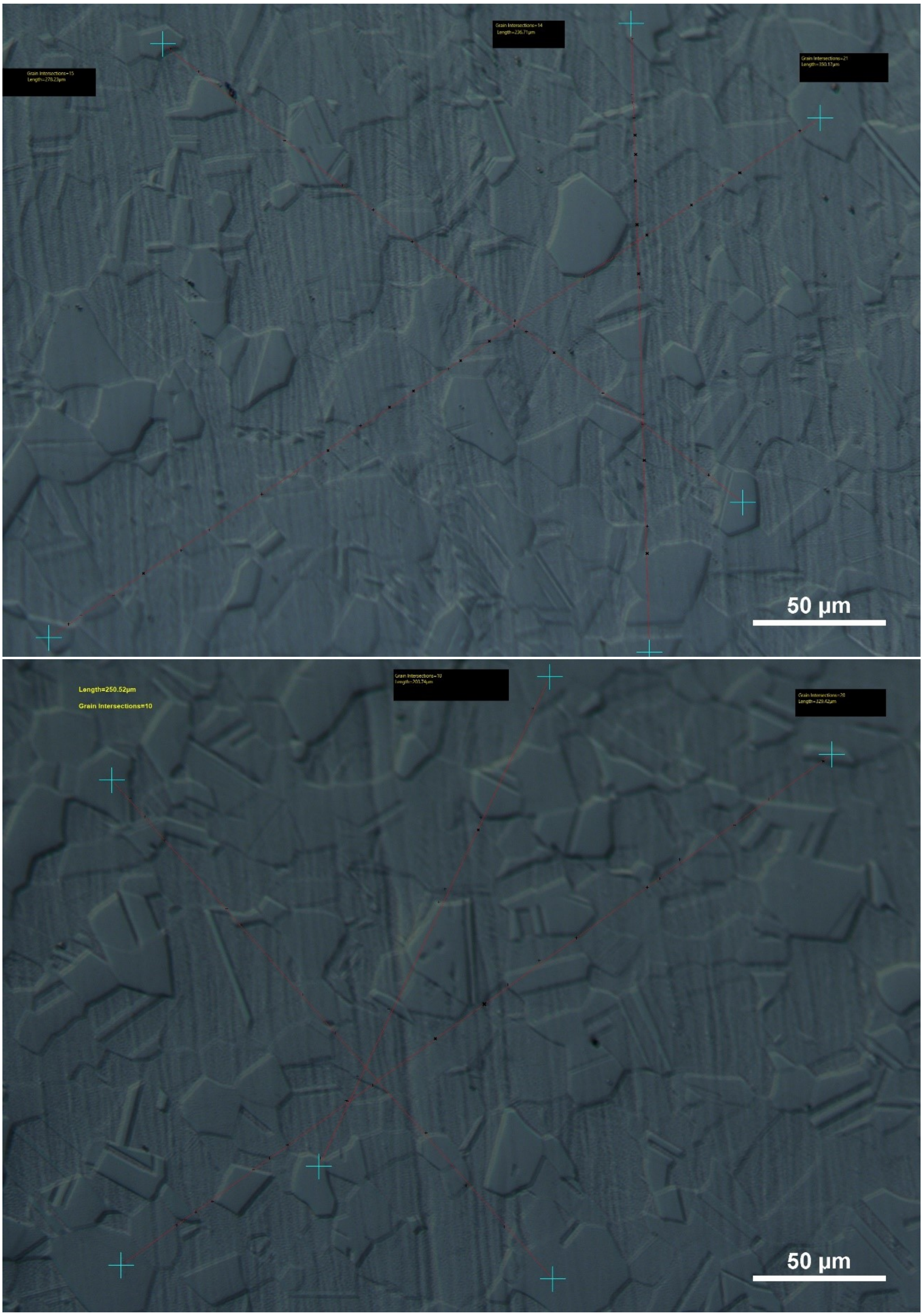

Figure B.2*: x- (up) and y-directions (down) of the 304 stainless steel at room temperature*

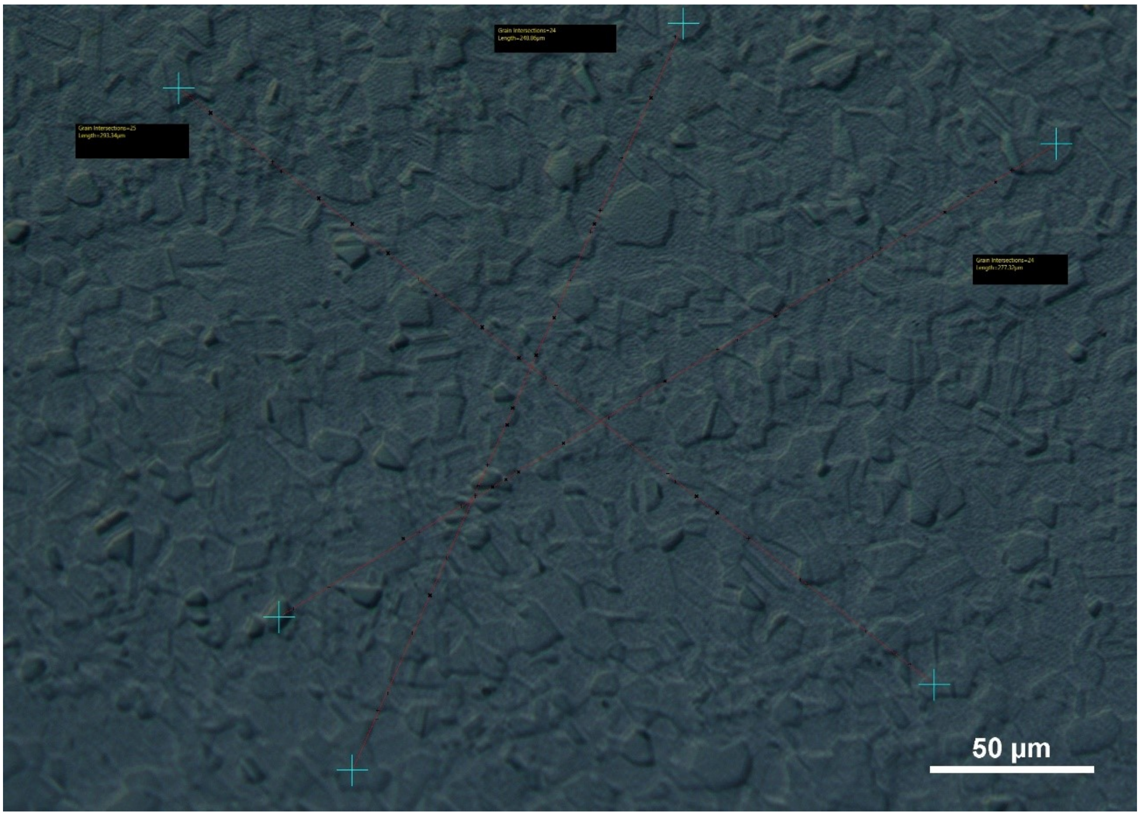

Figure B.3*: 316 stainless steel, planar view at room temperature*

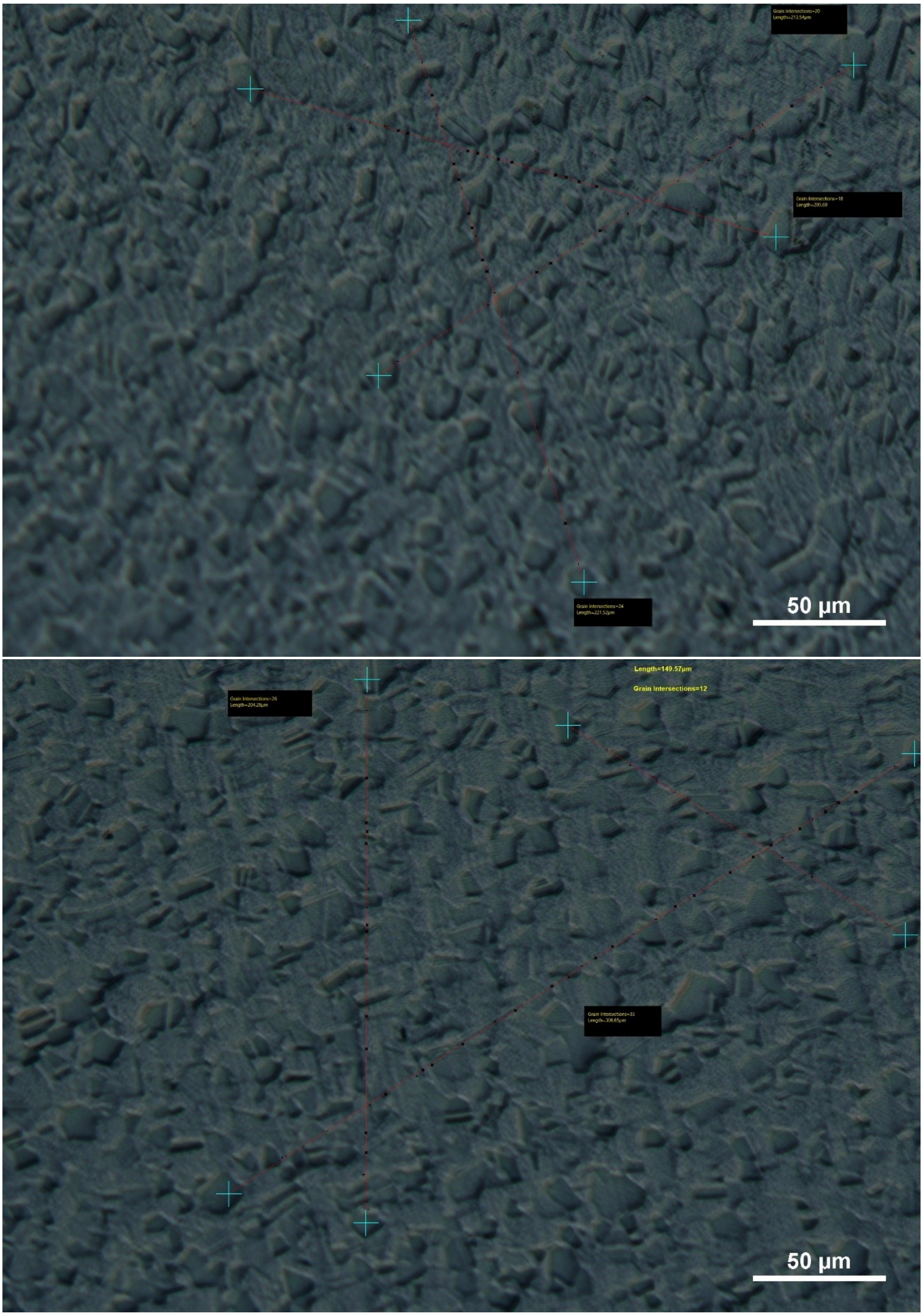

***Figure B.4**: x- (up) and y-directions (down) of 316 at room temperature*

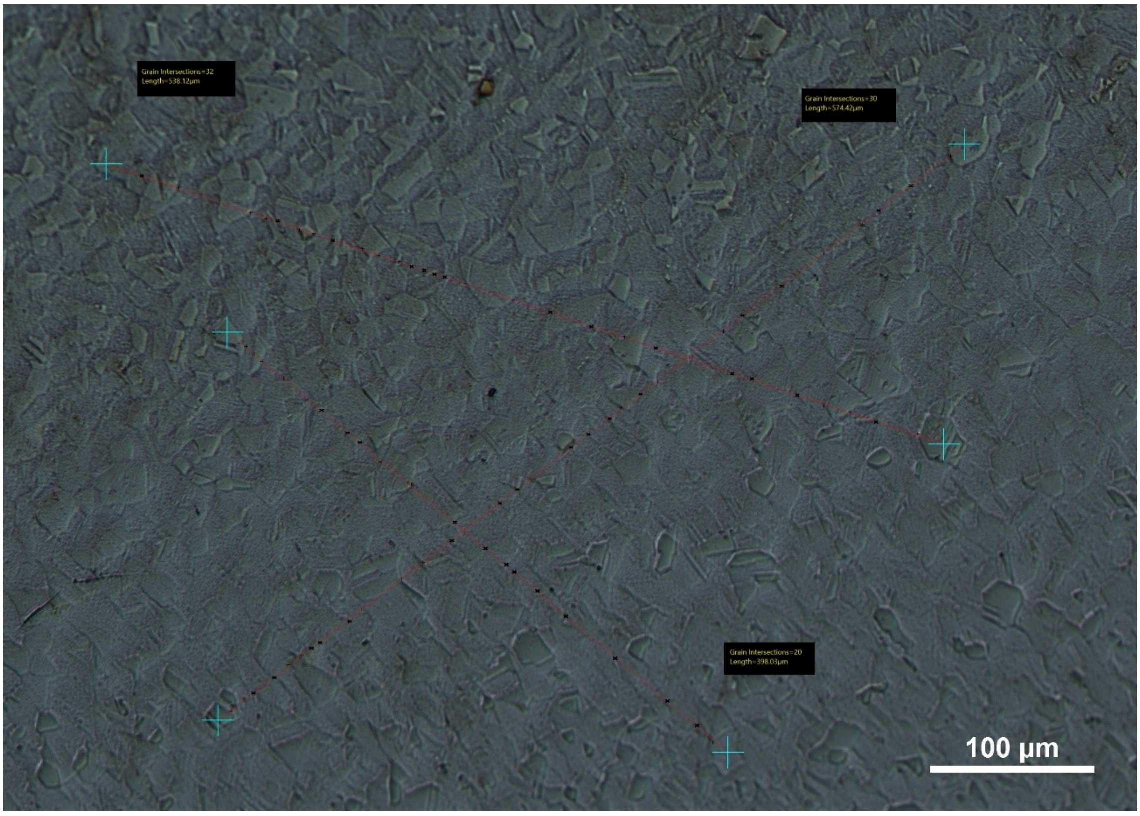

***Figure B.5**: 321H stainless steel, planar view at room temperature*

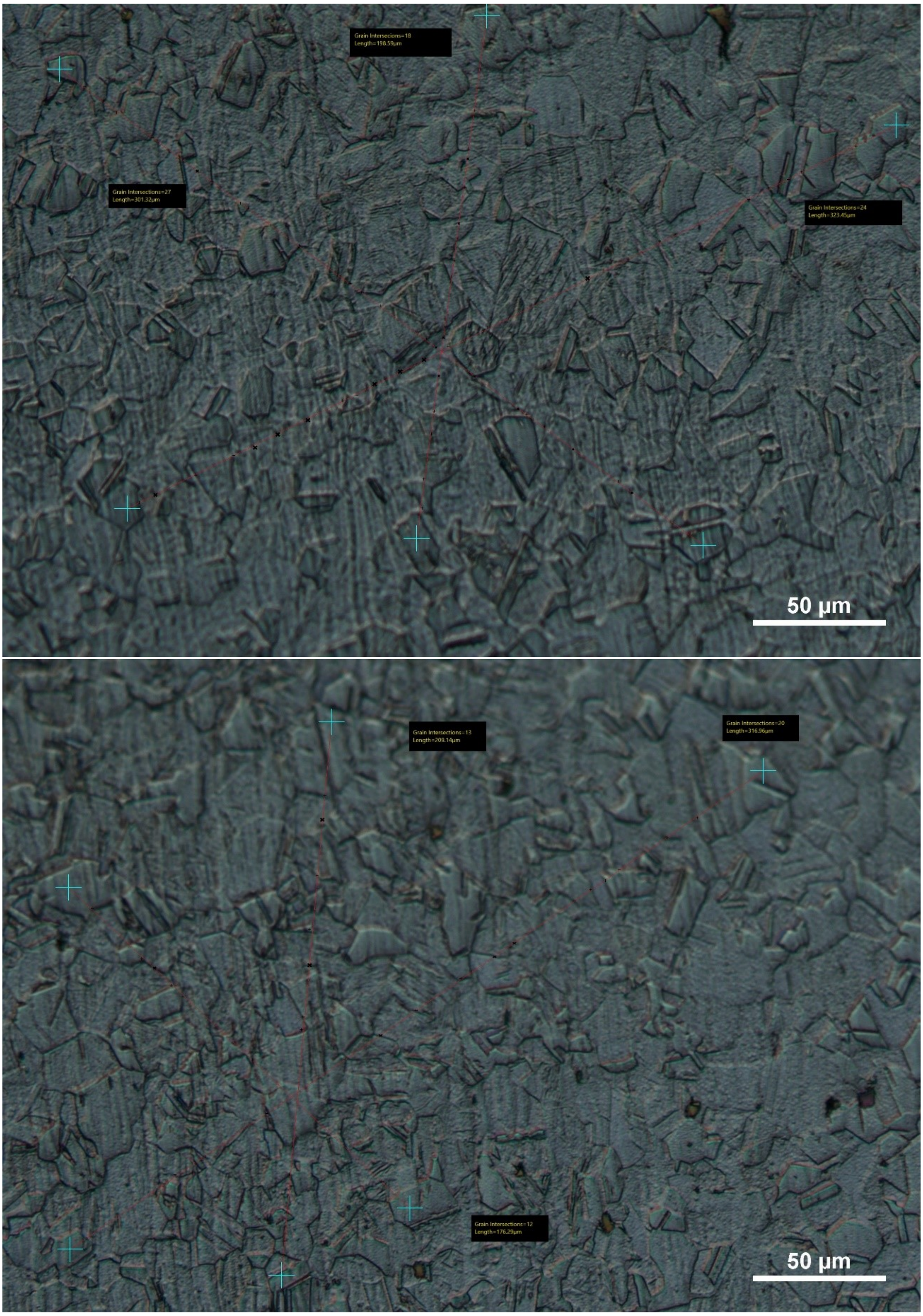

***Figure B.6**: x- (up) and y-directions (down) of 321H at room temperature*

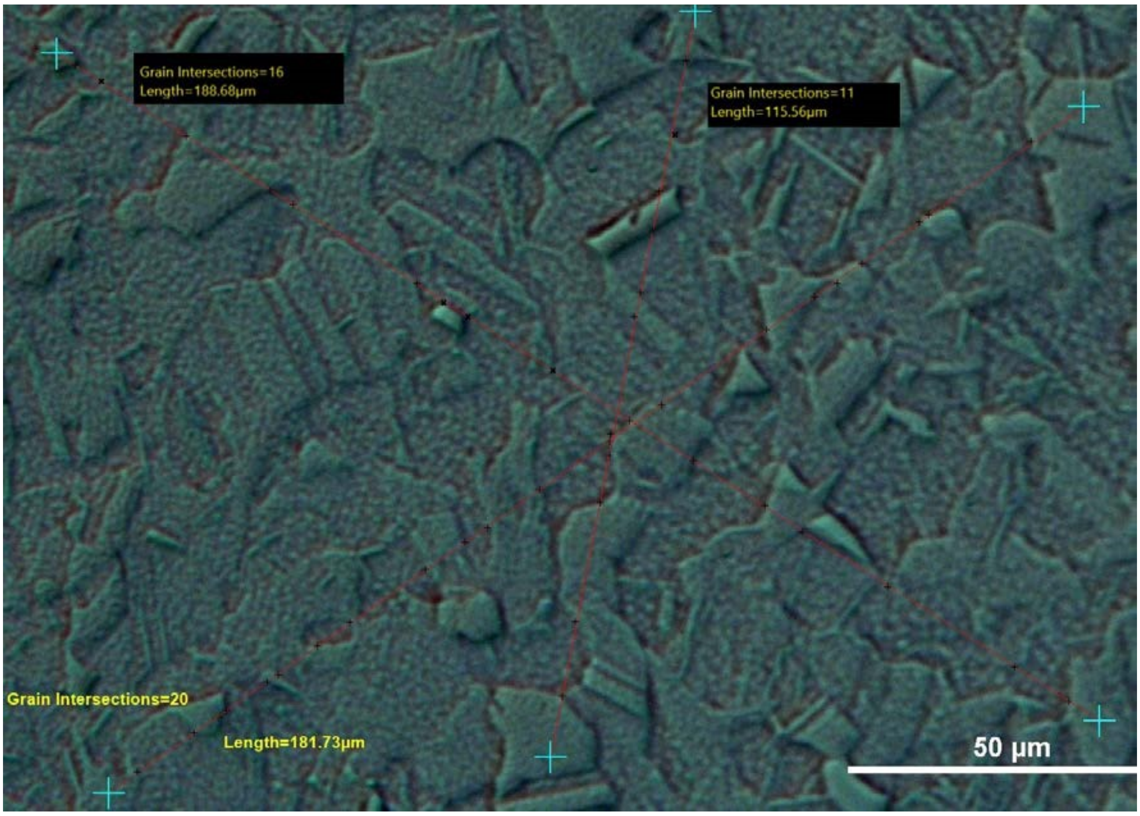

Figure B.7: *347H stainless steel, planar view at room temperature*

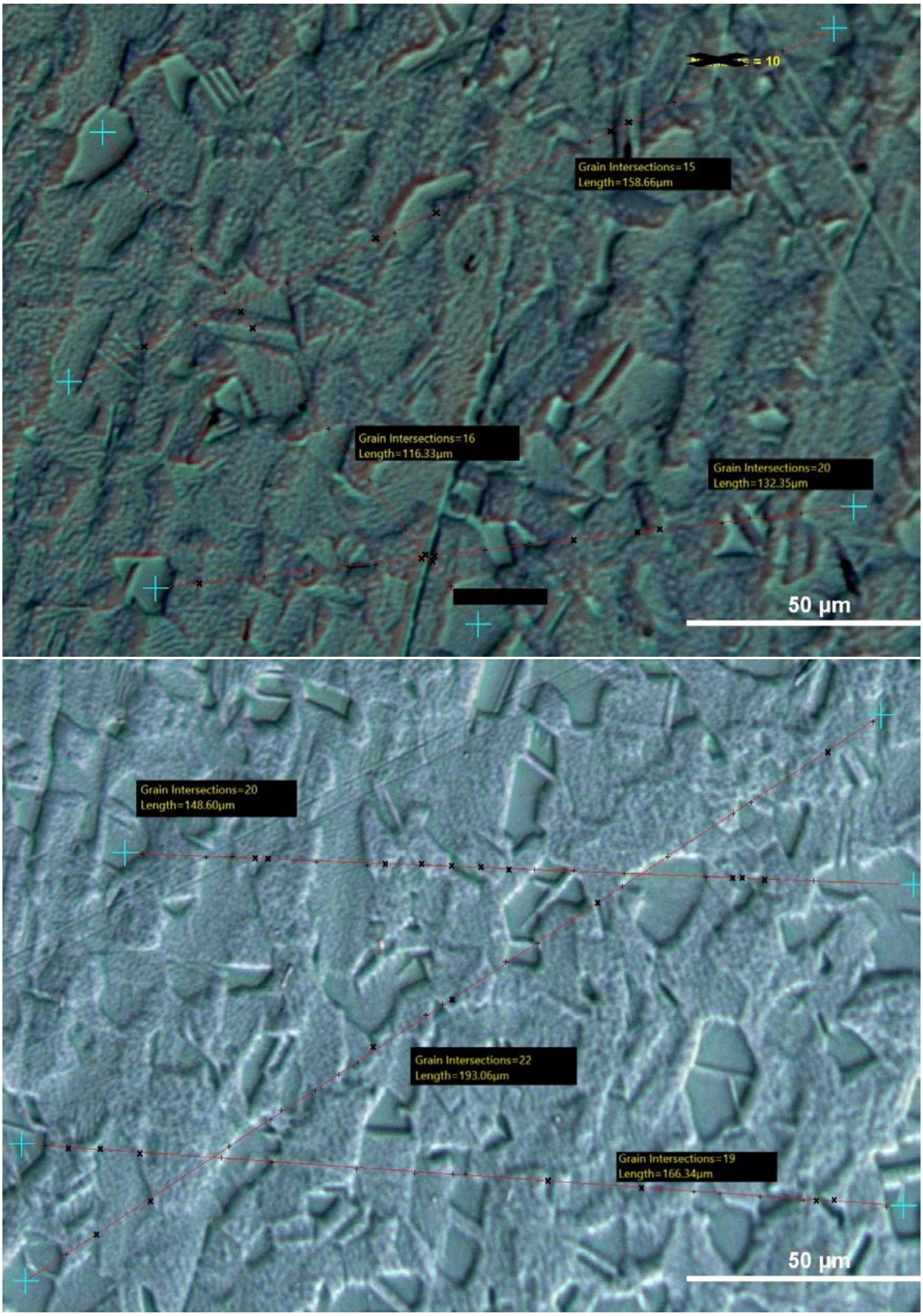

Figure B.8: *x- (up) and y-directions (down) of 347H at room temperature*

Appendix C

Cross-sectional measurements of grain sizes are presented here in Appendix C, all of the samples are kept at room temperatures.

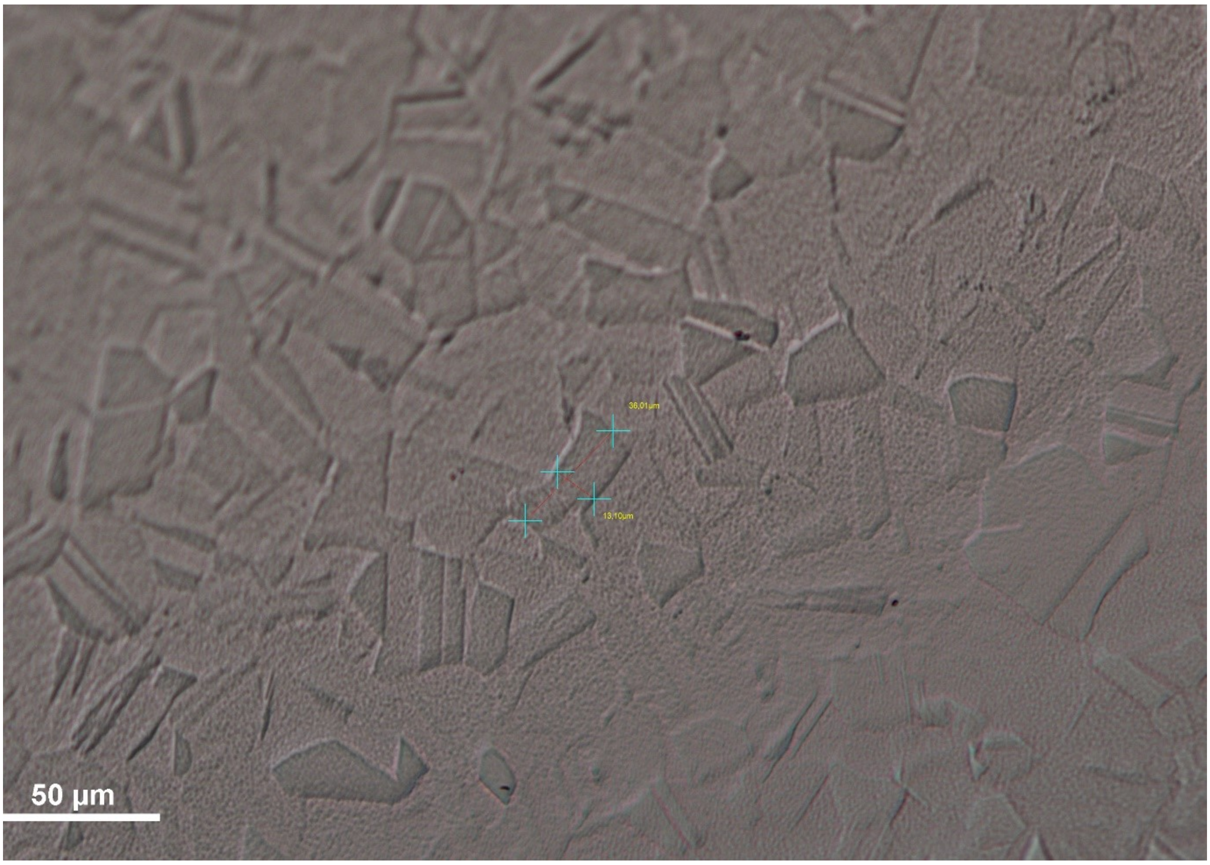

Figure C.1*: Cross section of the planar view, sample 304.*

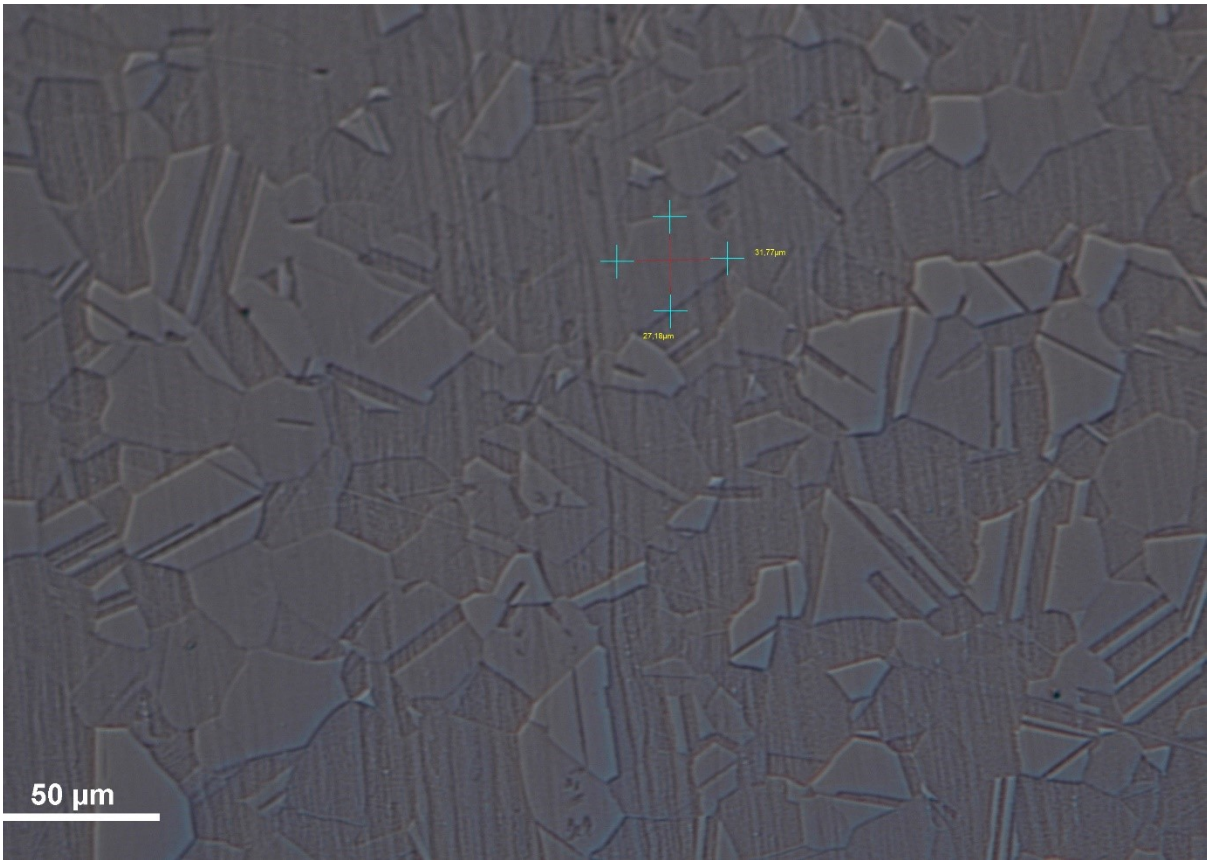

Figure C.2*: Cross section of the x-direction, sample 304.*

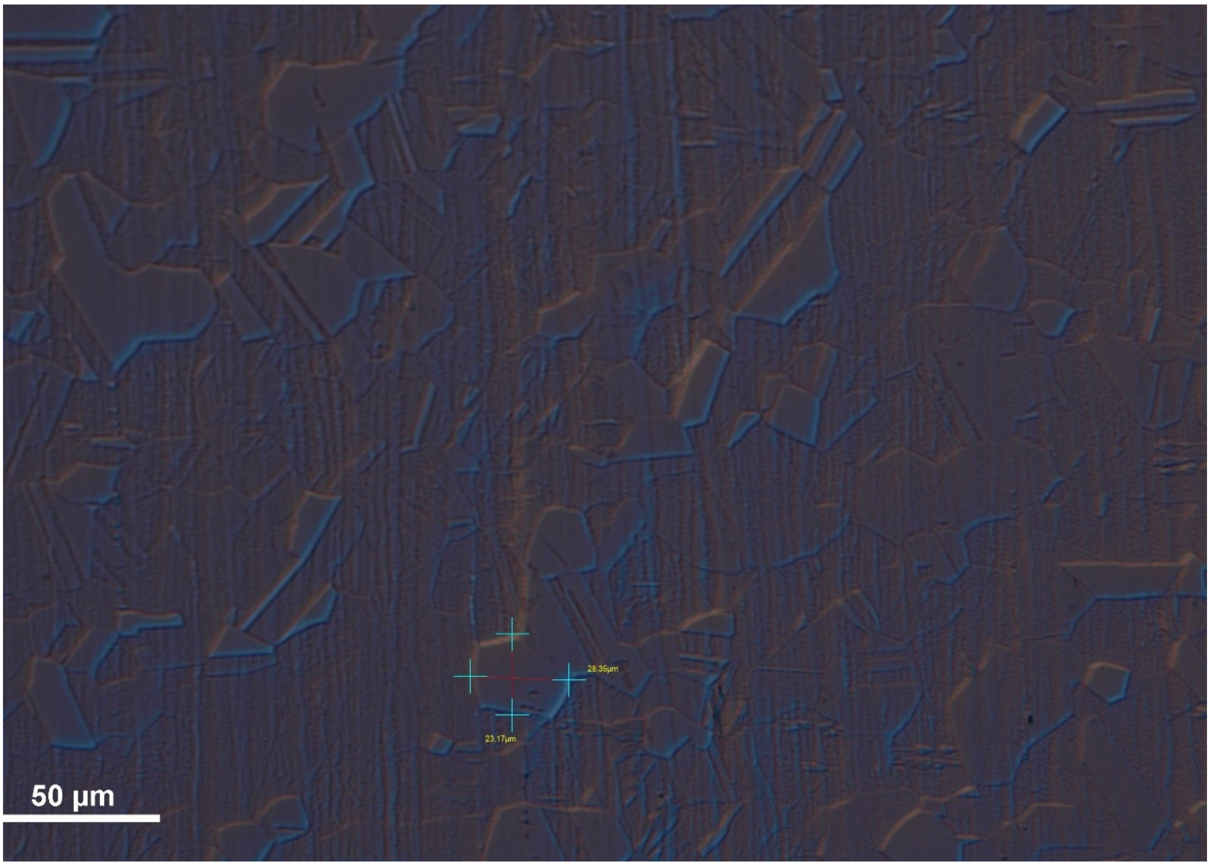

***Figure C.3**: Cross section of the y-direction, sample 304.*

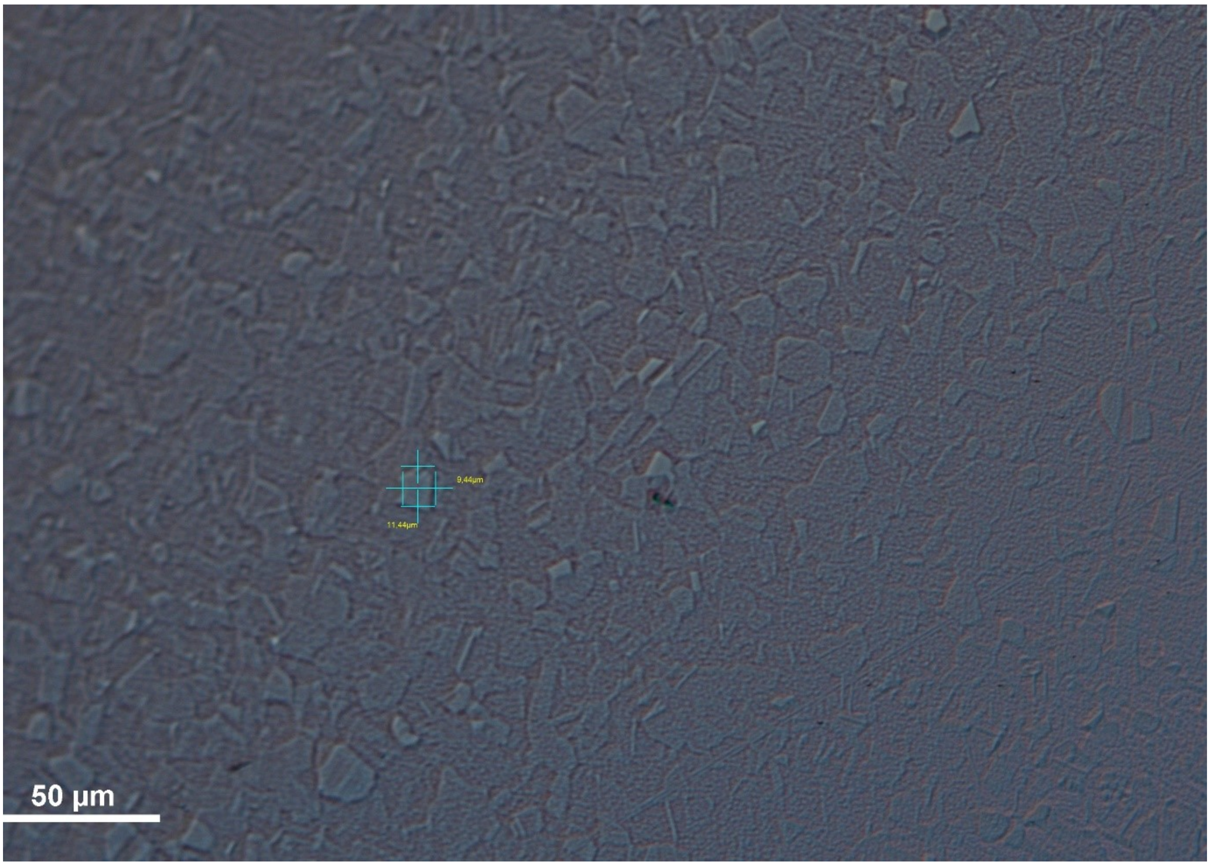

Figure C.4*: Cross section of the planar view, sample 316.*

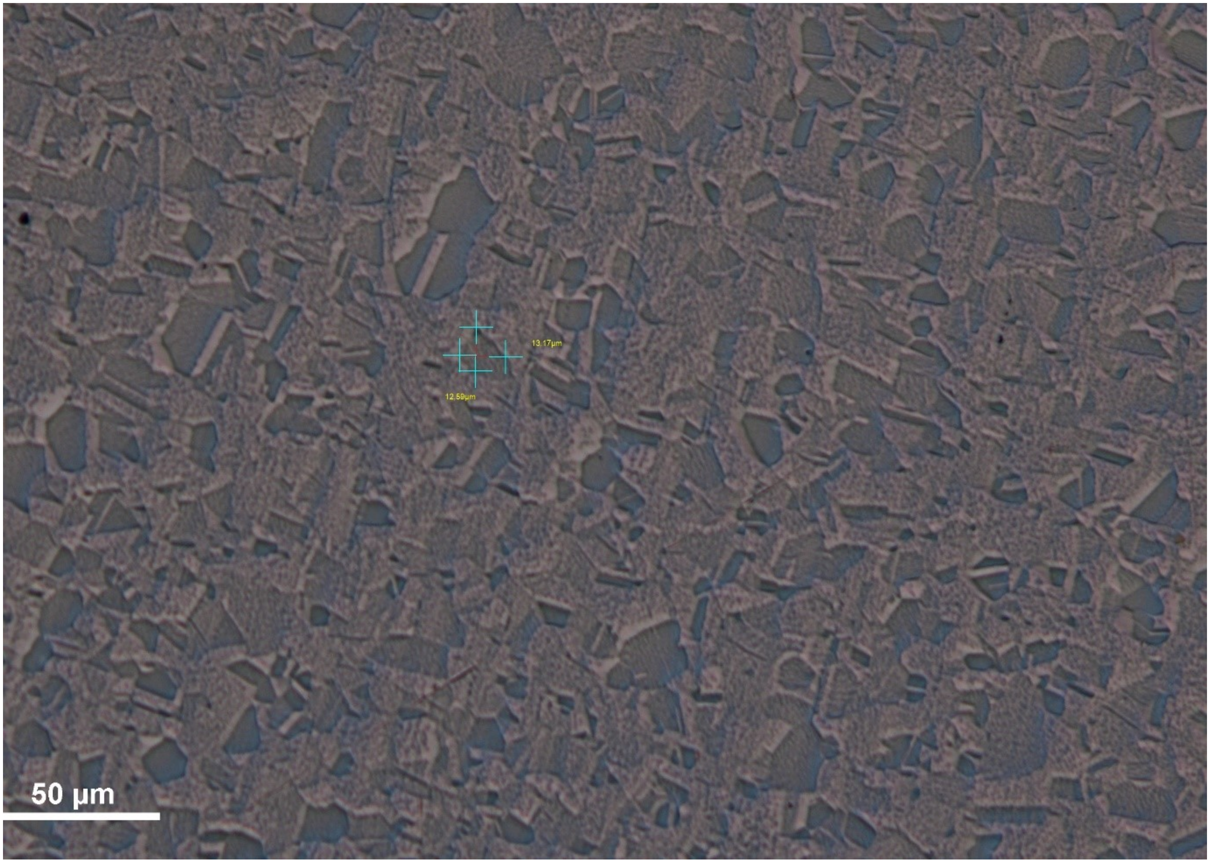

Figure C.5*: Cross section of the x-direction, sample 316.*

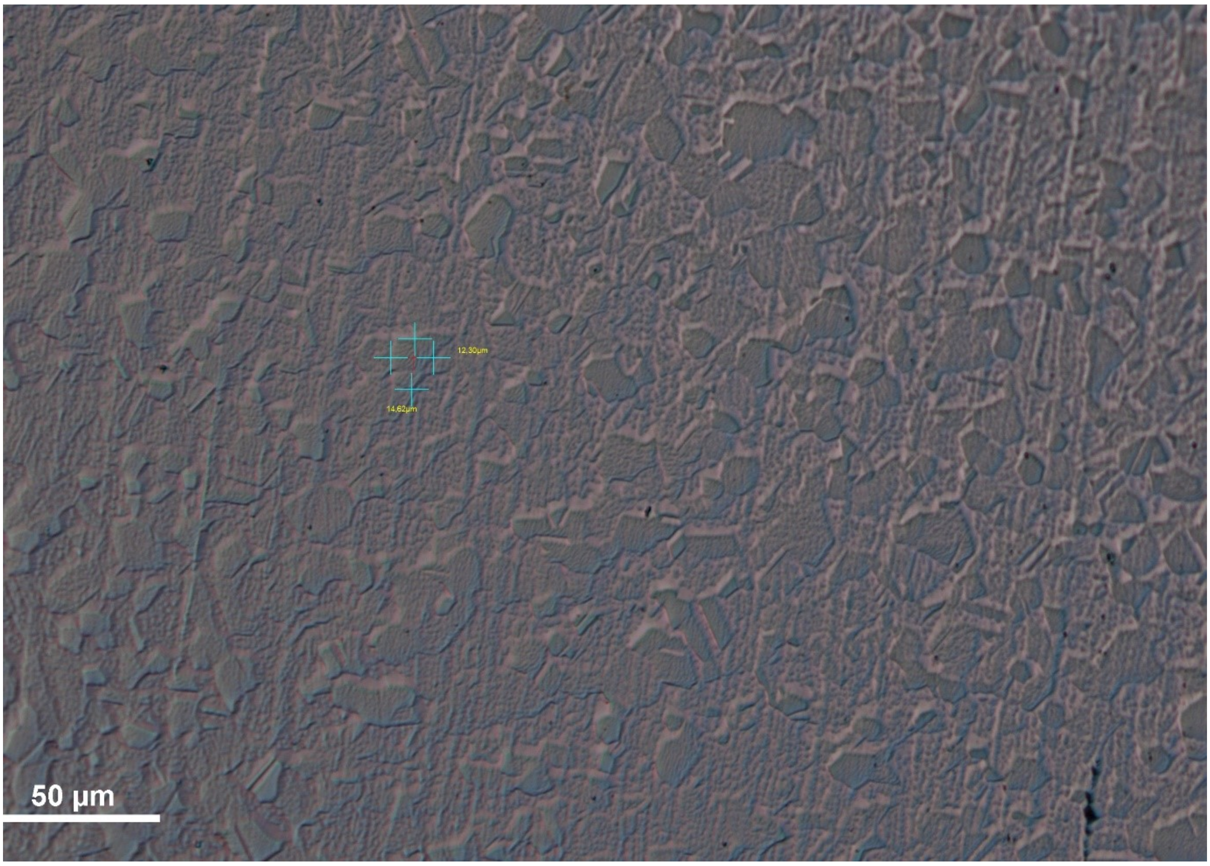

Figure C.6*: Cross section of the y-direction, sample 316.*

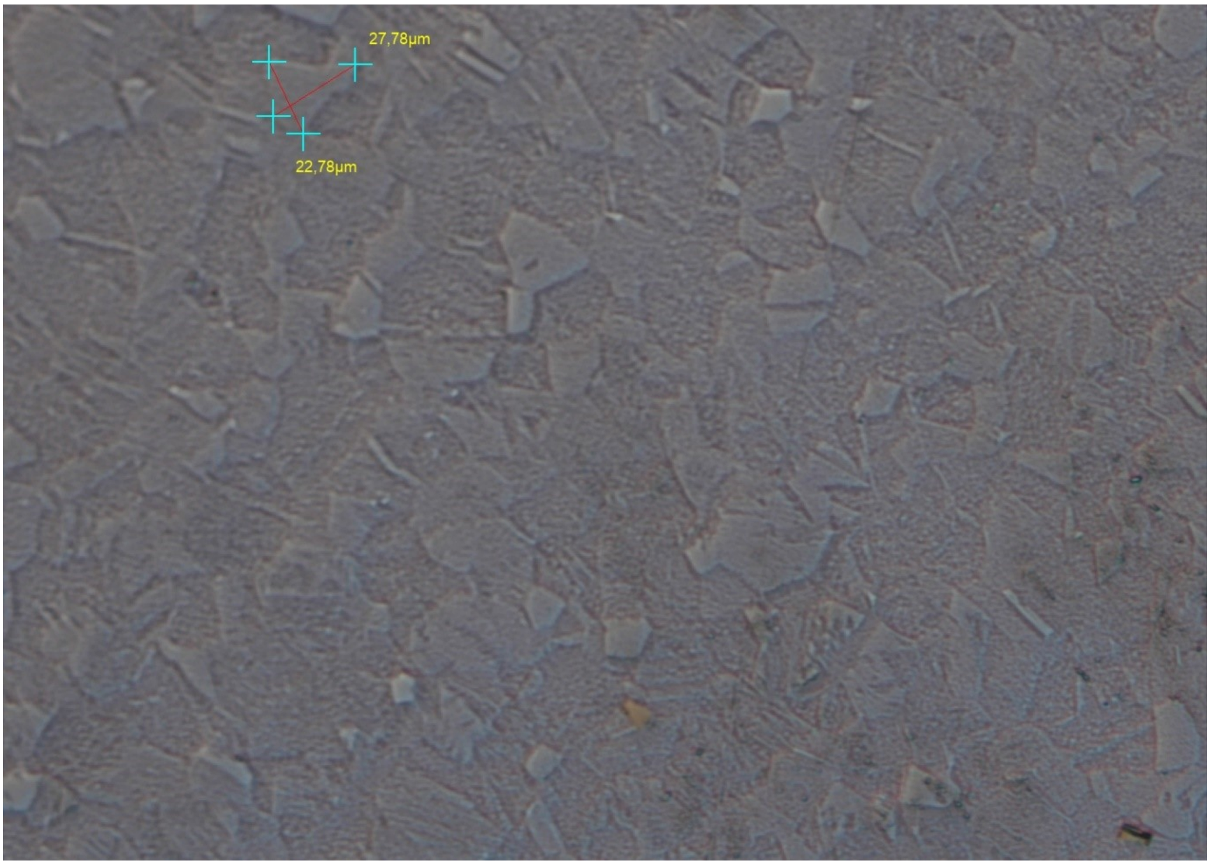

Figure C.7*: Cross section of the planar view, sample 321H.*

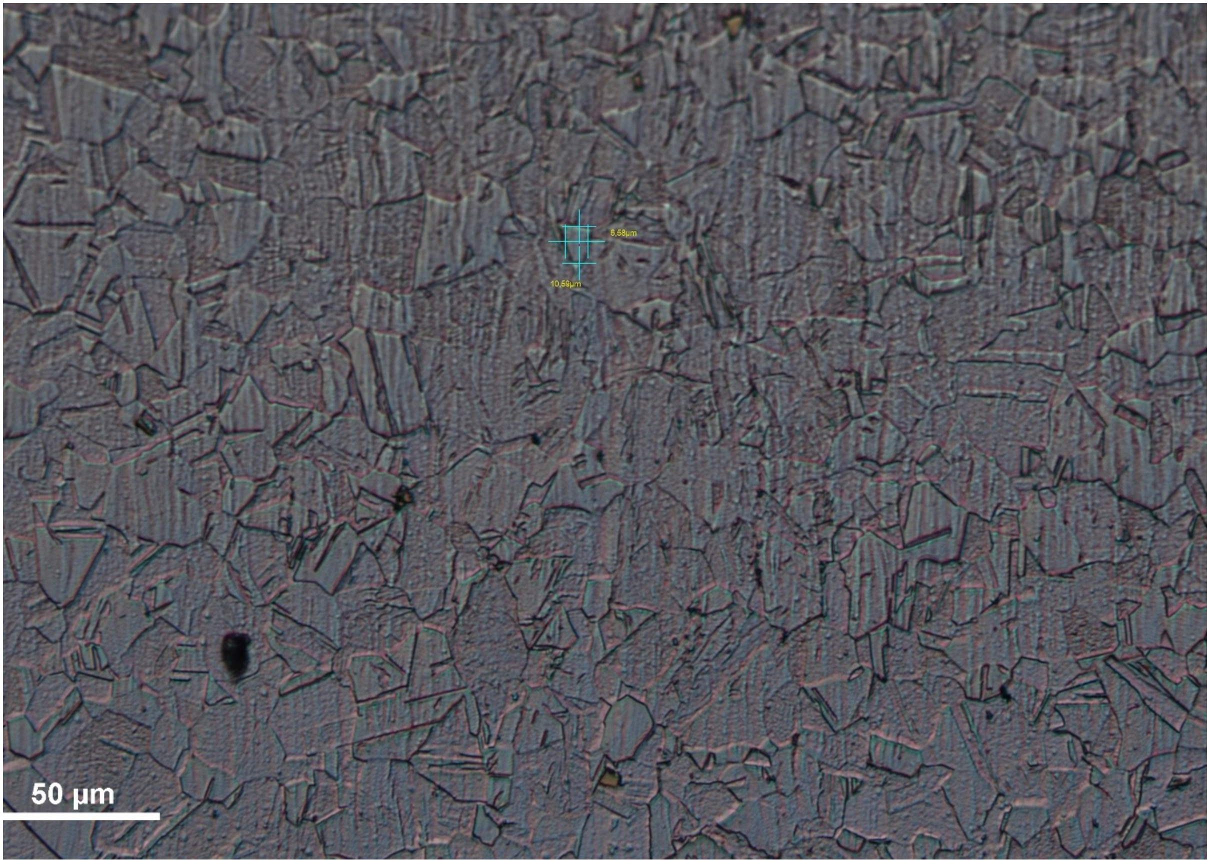

Figure C.8*: Cross section of the x-direction, sample 321H.*

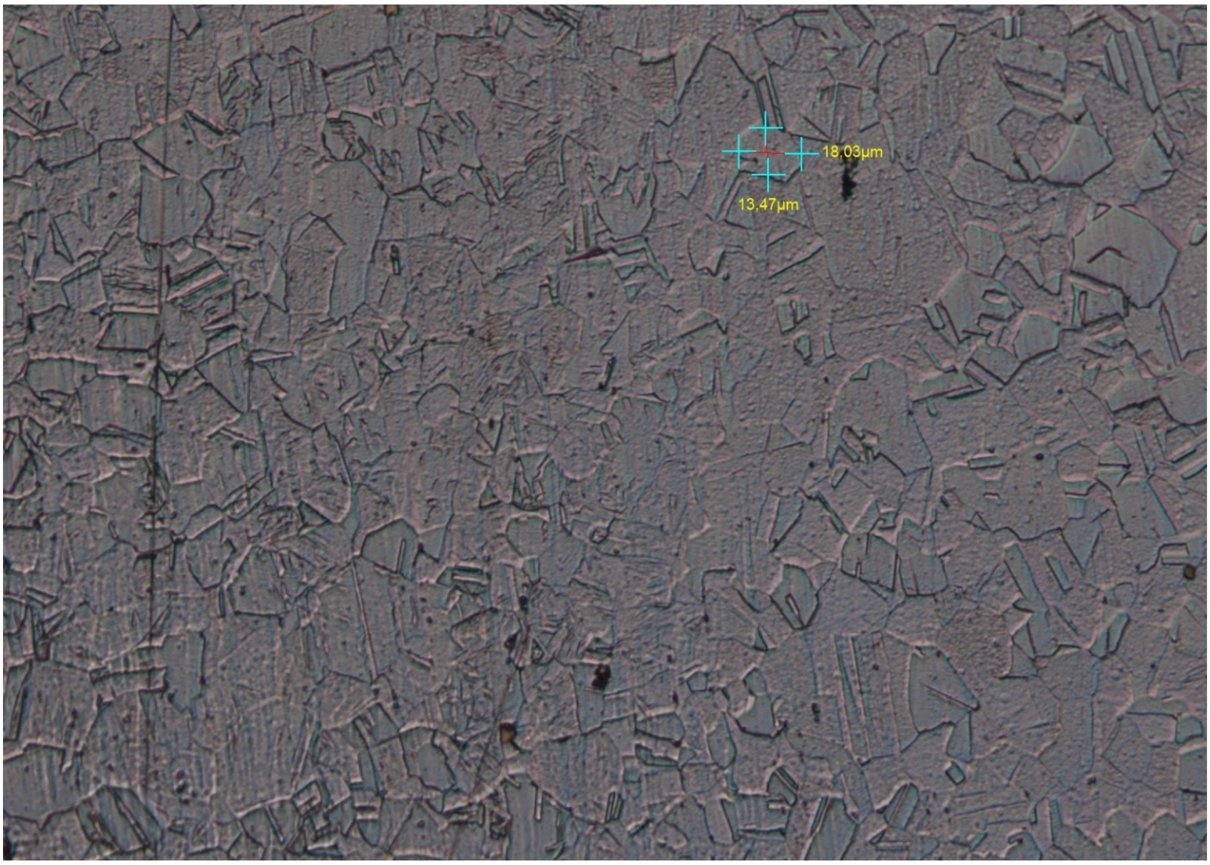

Figure C.9*: Cross section of the y-direction, sample 321H.*

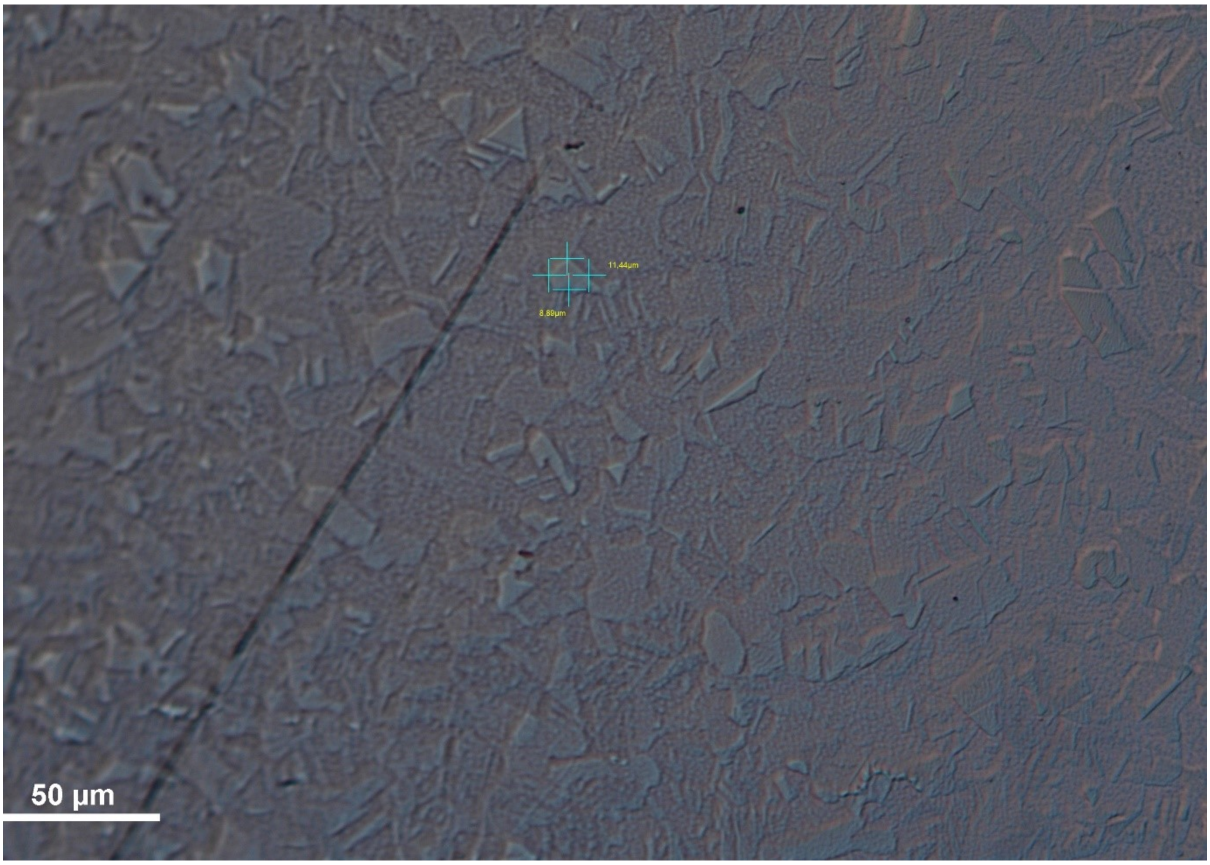

Figure C.10*: Cross section of the planar view, sample 347H.*

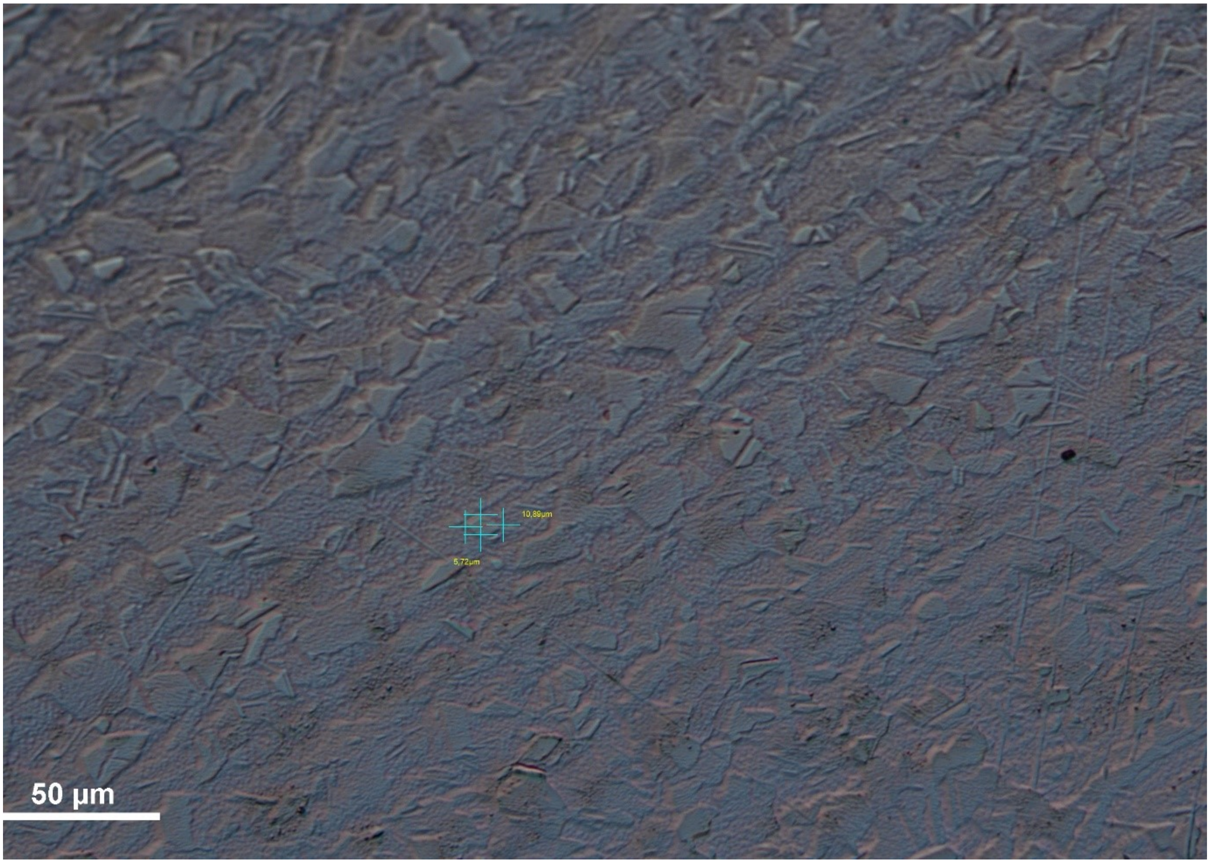

Figure C.11*: Cross section of the x-direction, sample 347H.*

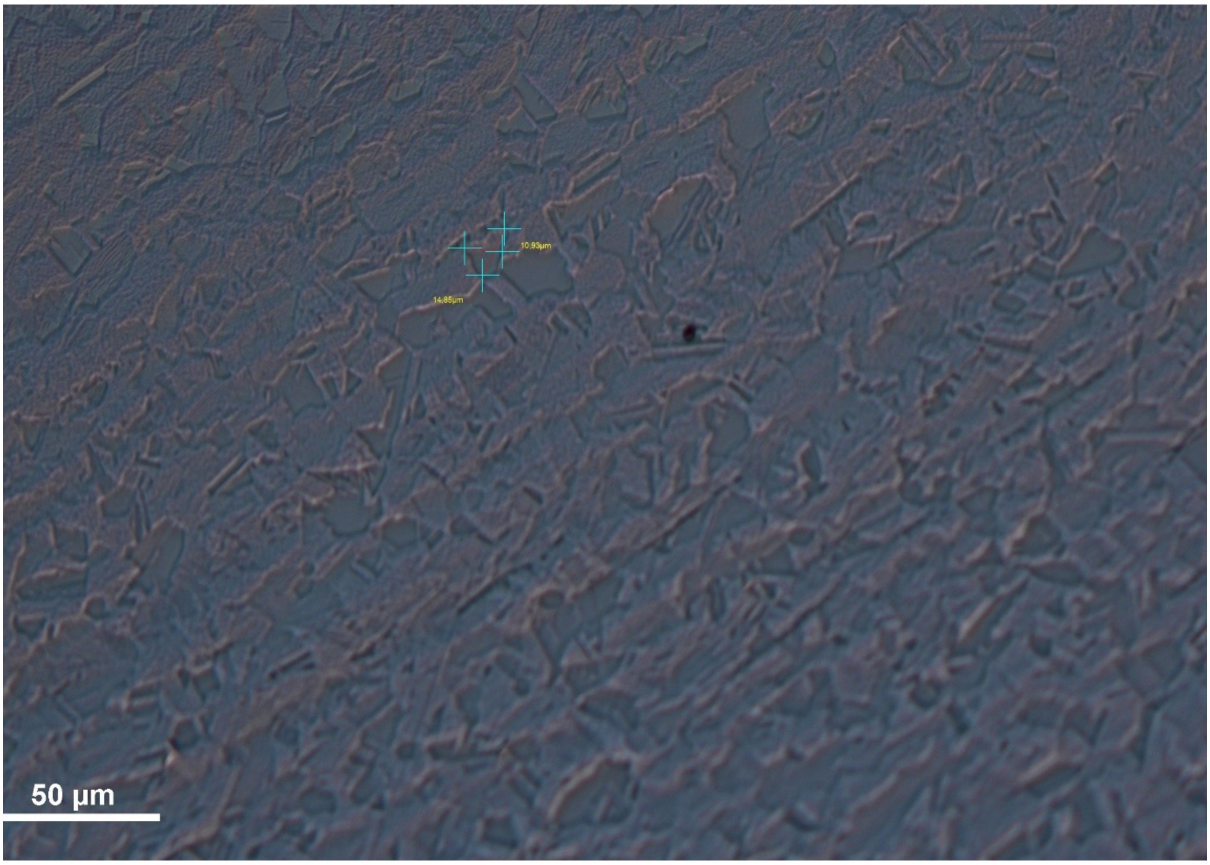

Figure C.12*: Cross section of the y-direction, sample 347H.*

Appendix D

Heat treated samples, investigated of their grain size through the ASTM E112-11 method.

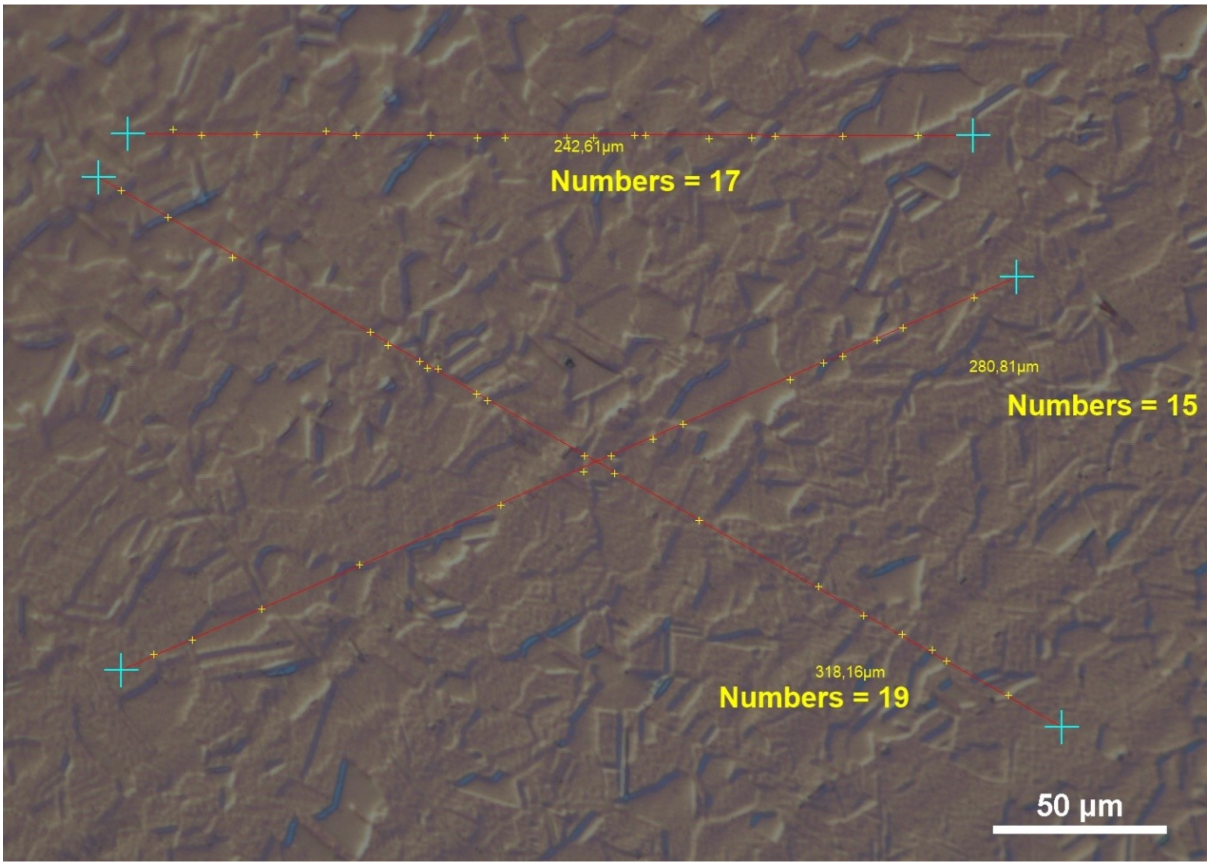

Figure D.1: *347H in the cross-sectional direction, heat treated at 1020°C*

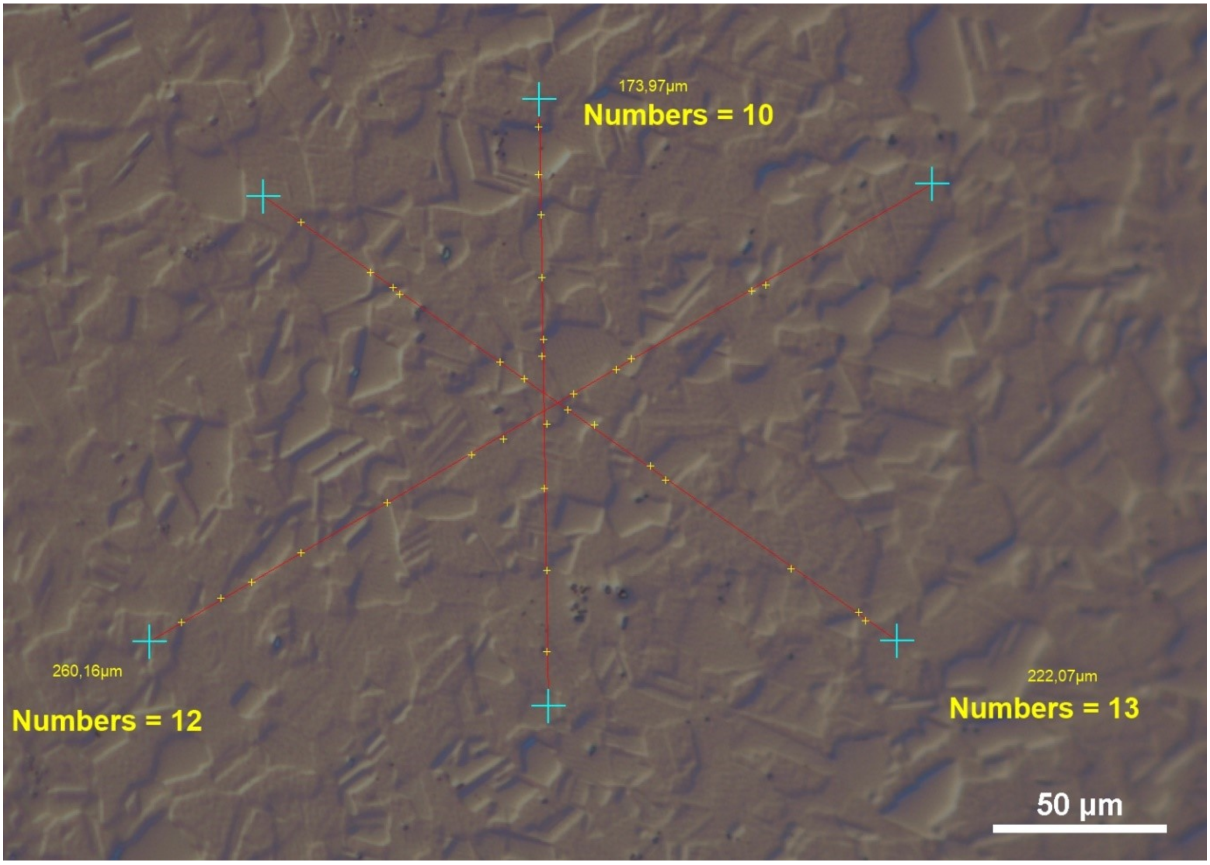

Figure D.2: *347H in the planar direction, heat treated at 1020°C*

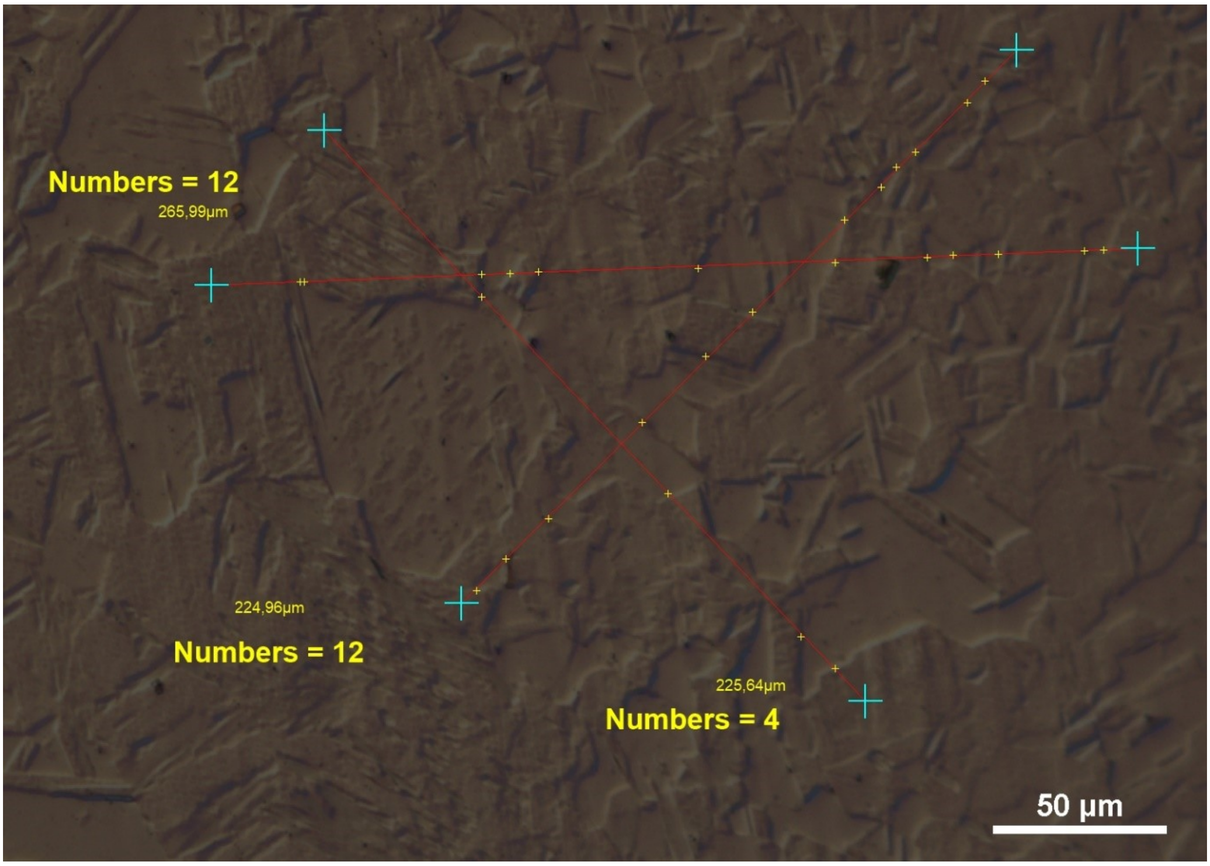

Figure D.3: *321H in the cross-sectional direction, heat treated at 1020*°C

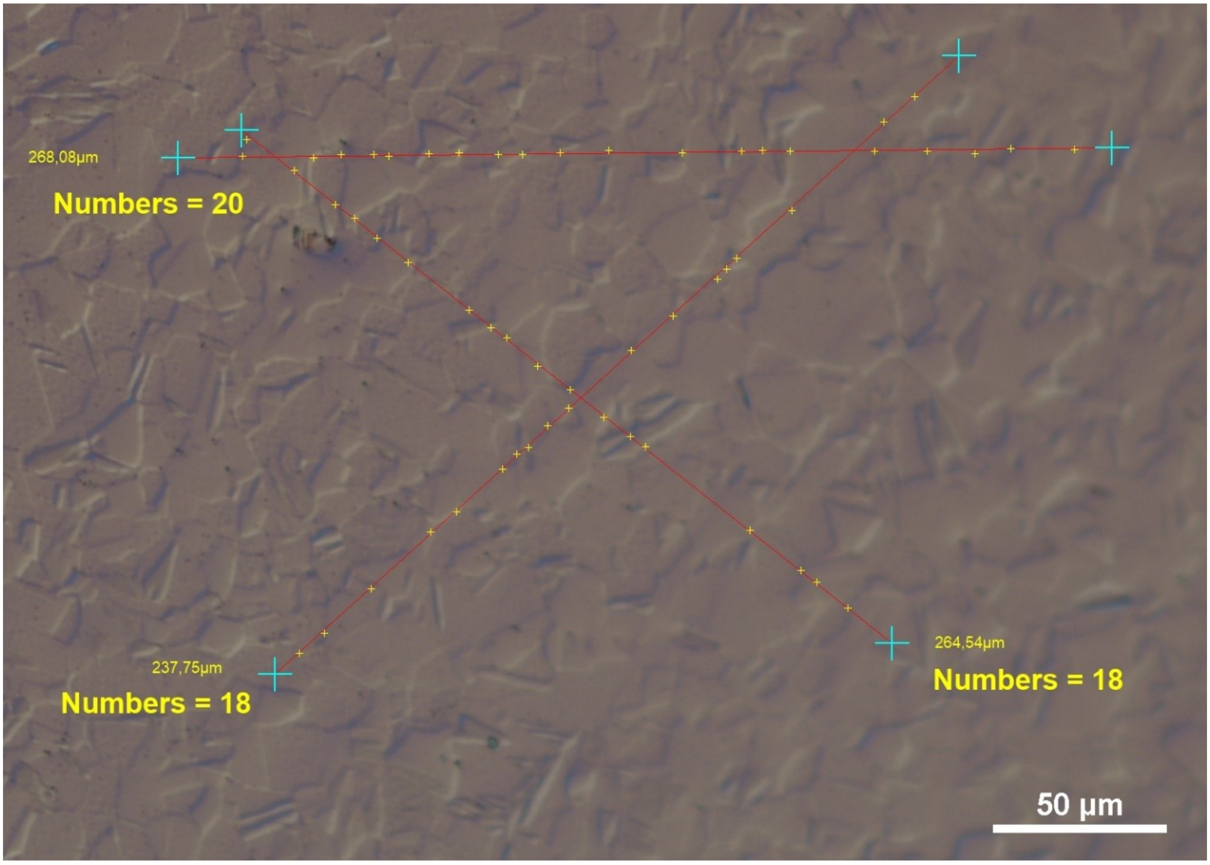

Figure D.4: *321H in the planar direction, heat treated at 1020*°C

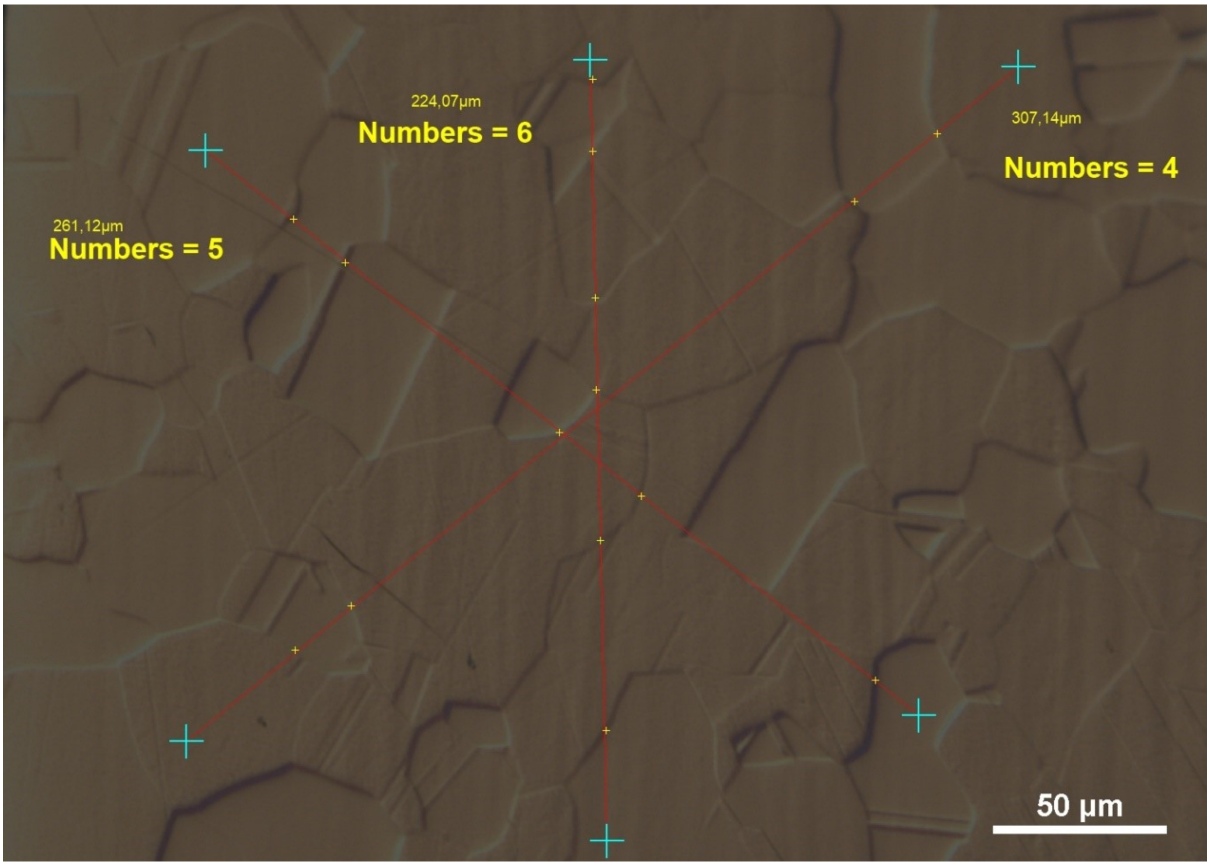

Figure D.5: *316 in the cross-sectional direction, heat treated at 1020°C*

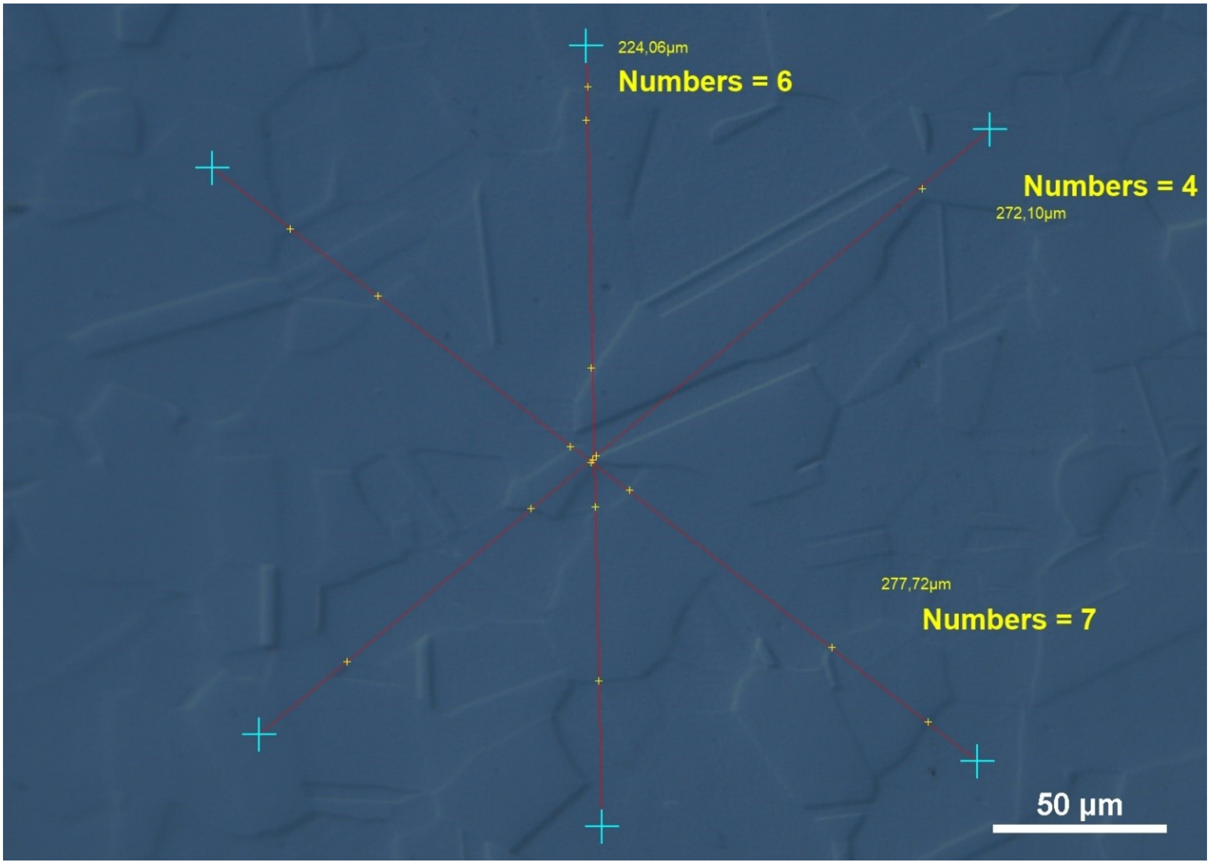

Figure D.6: *316 in the planar direction, heat treated at 1020°C*

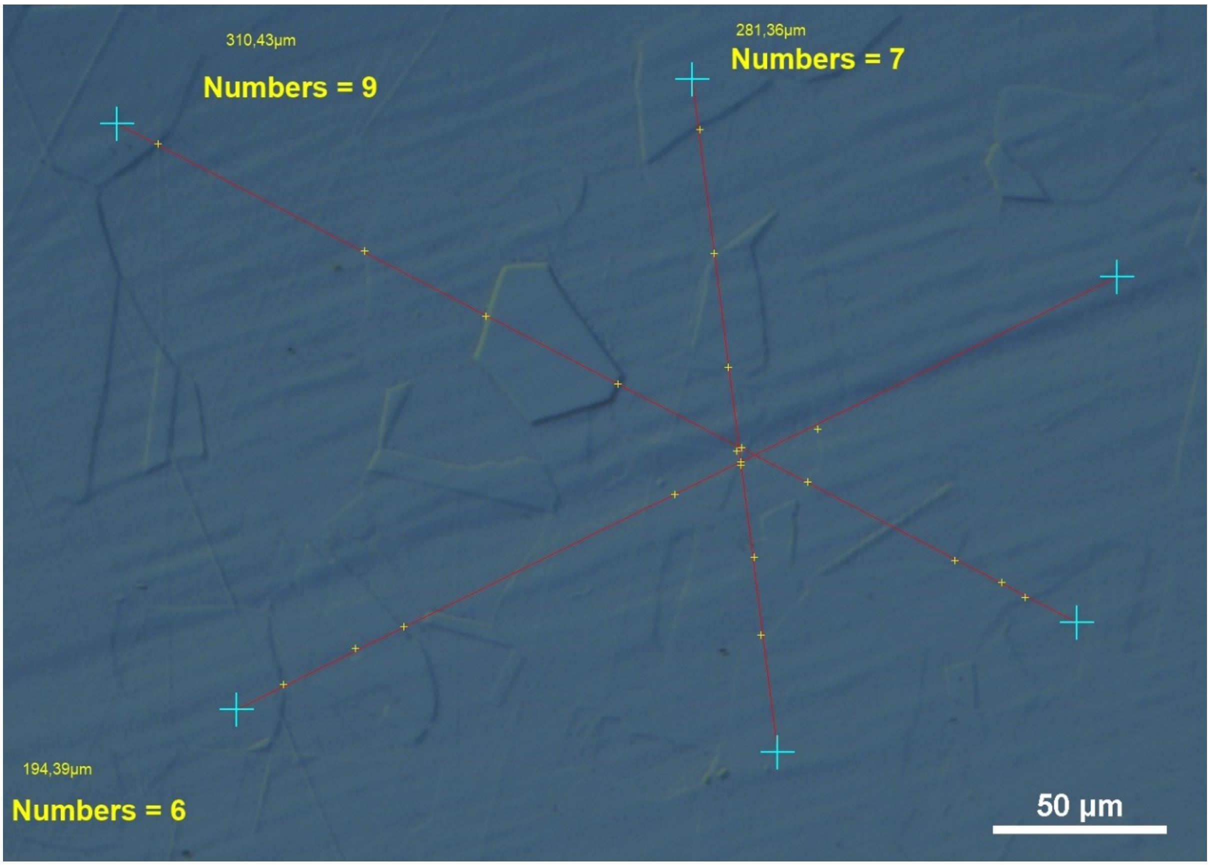

Figure D.7: *304 in the cross-sectional direction, heat treated at 1020℃*

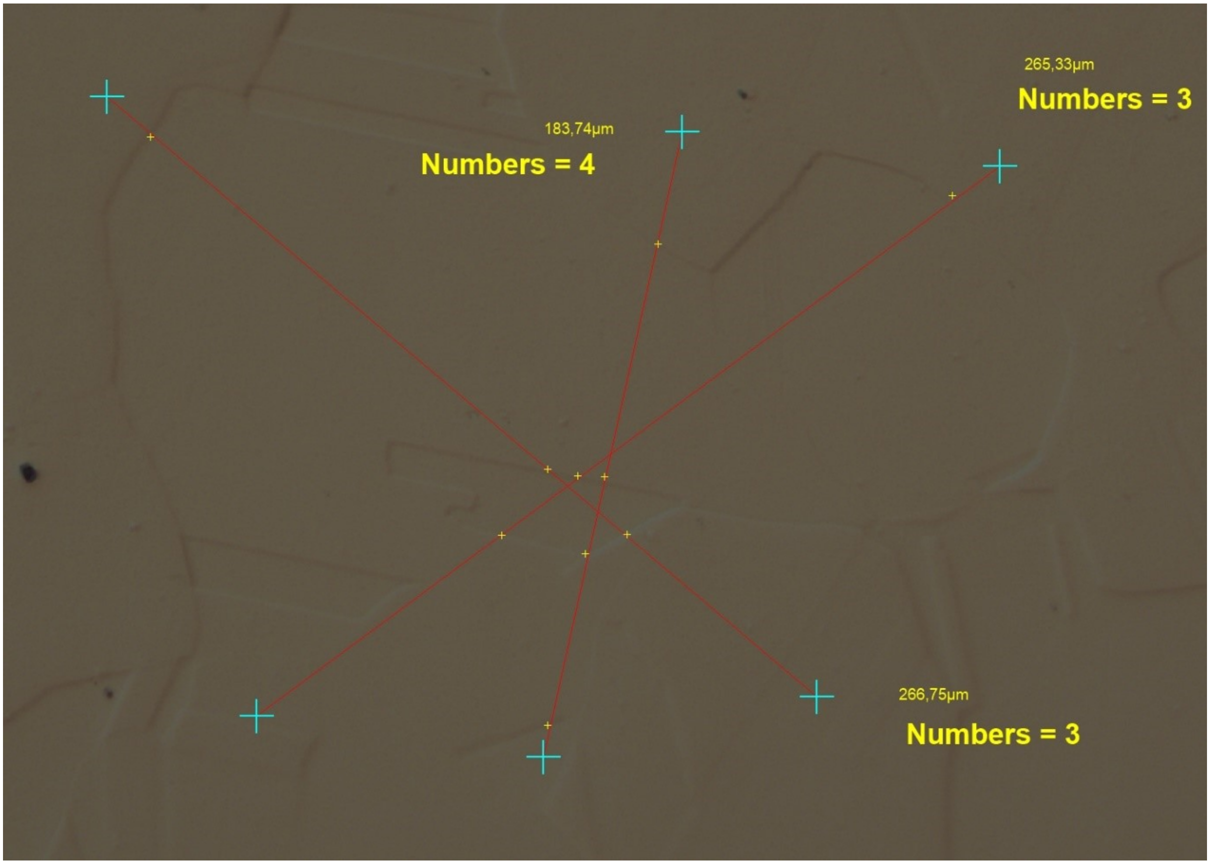

Figure D.8: *304 in the planar direction, heat treated at 1020℃*

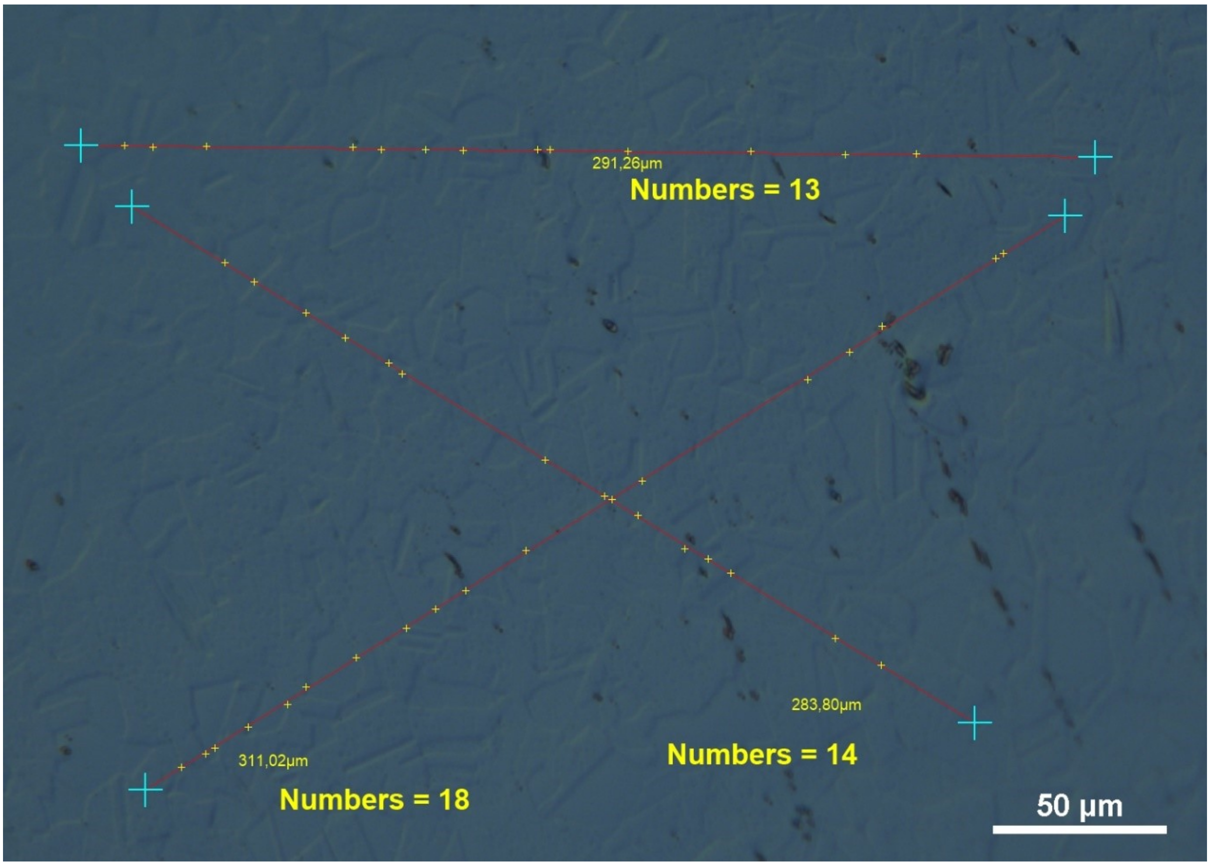
291,26µm
Numbers = 13
283,80µm
Numbers = 14
311,02µm
Numbers = 18
50 µm

Figure D.9: *347H in the cross-sectional direction, heat treated at 1130℃*

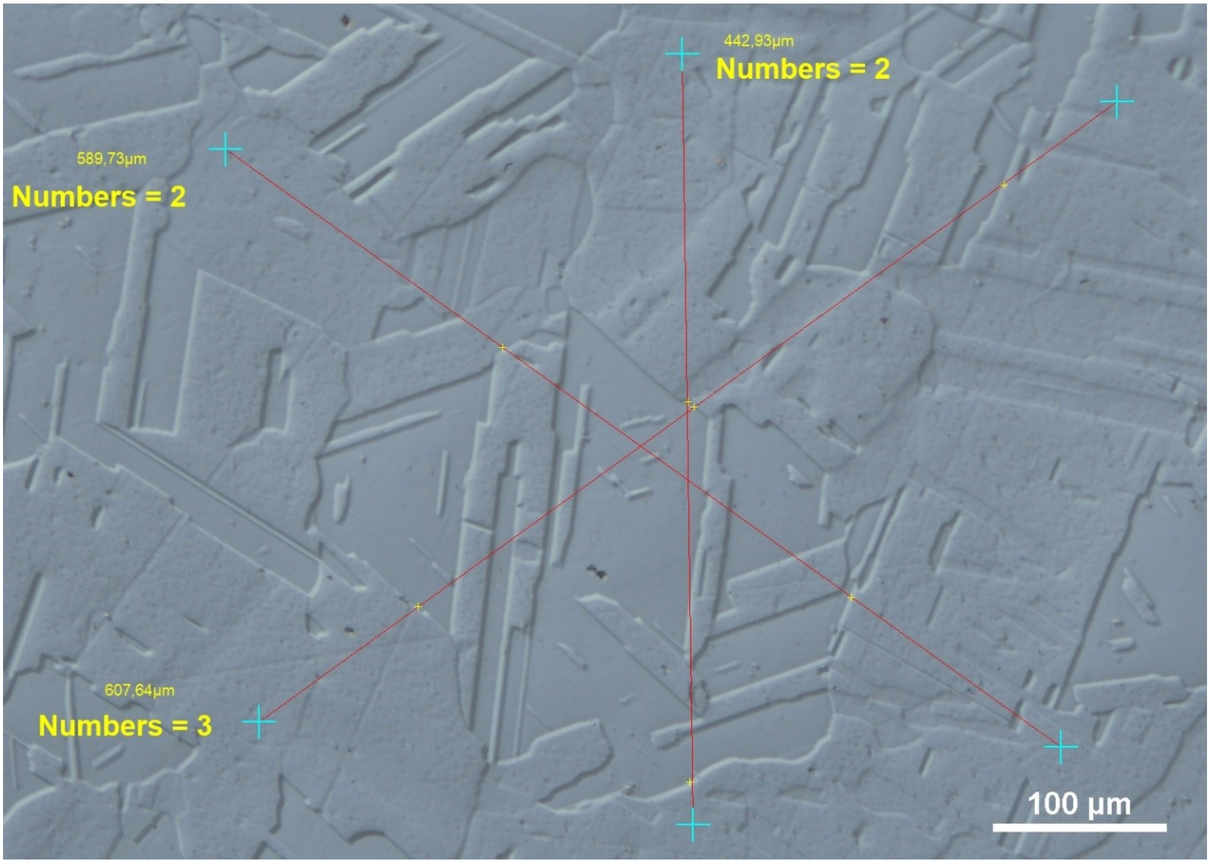

Figure D.10: *347H in the planar direction, heat treated at 1130℃*

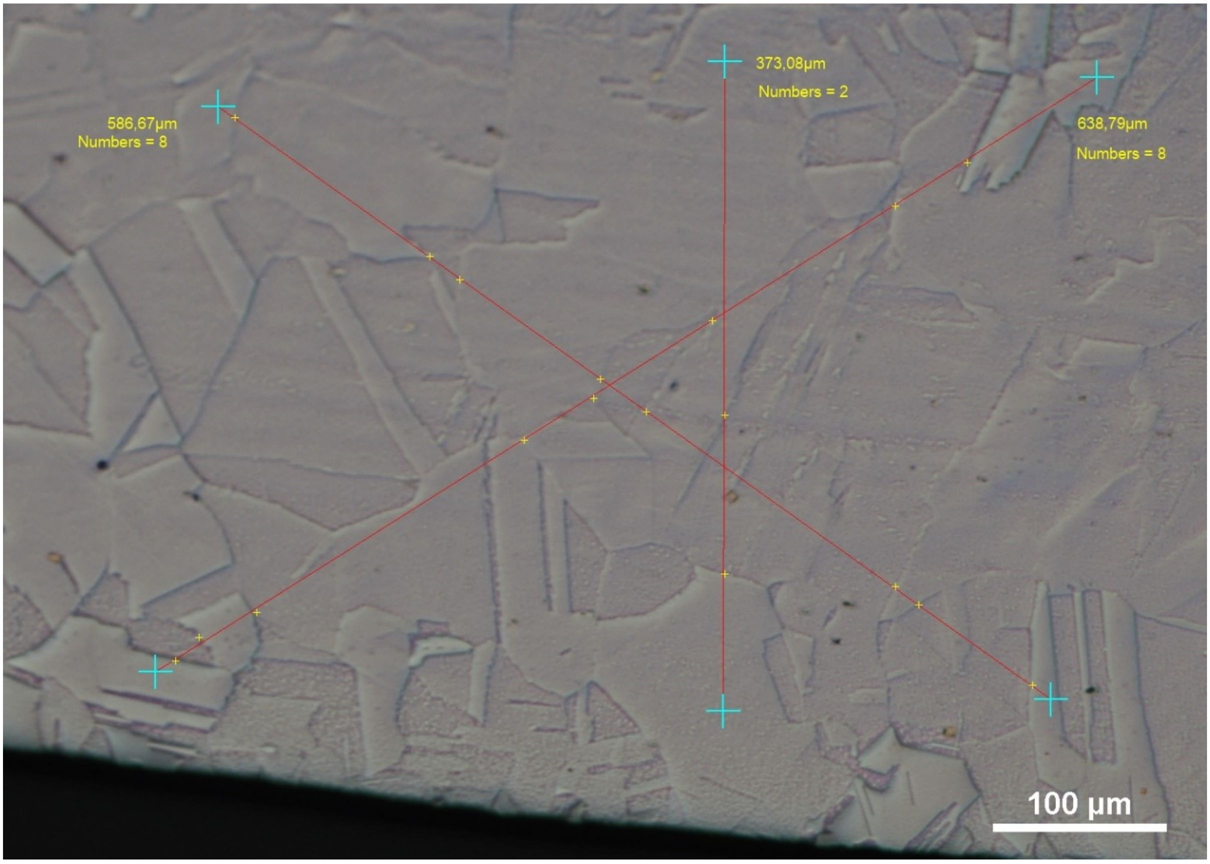

Figure D.11: *321H in the cross-sectional direction, heat treated at 1130℃*

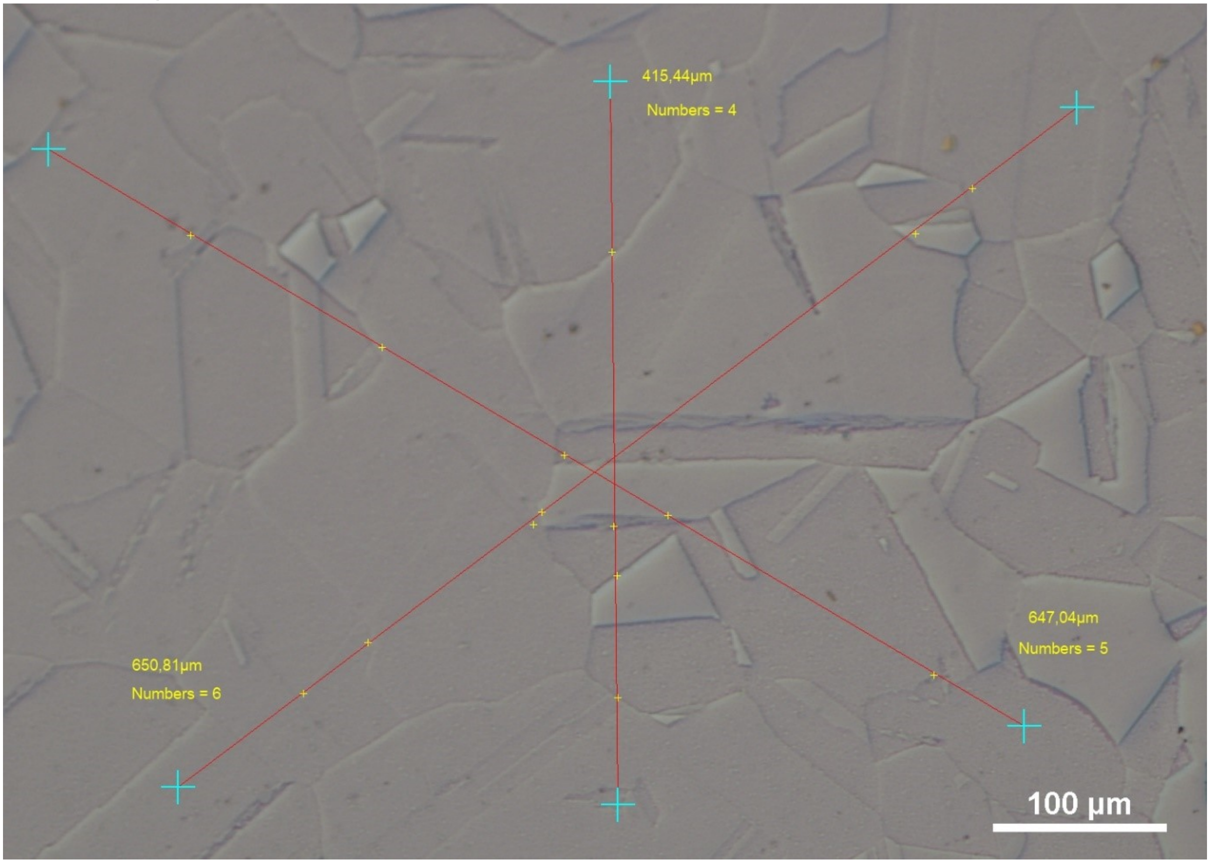

Figure D.12: *321H in the planar direction, heat treated at 1130℃*

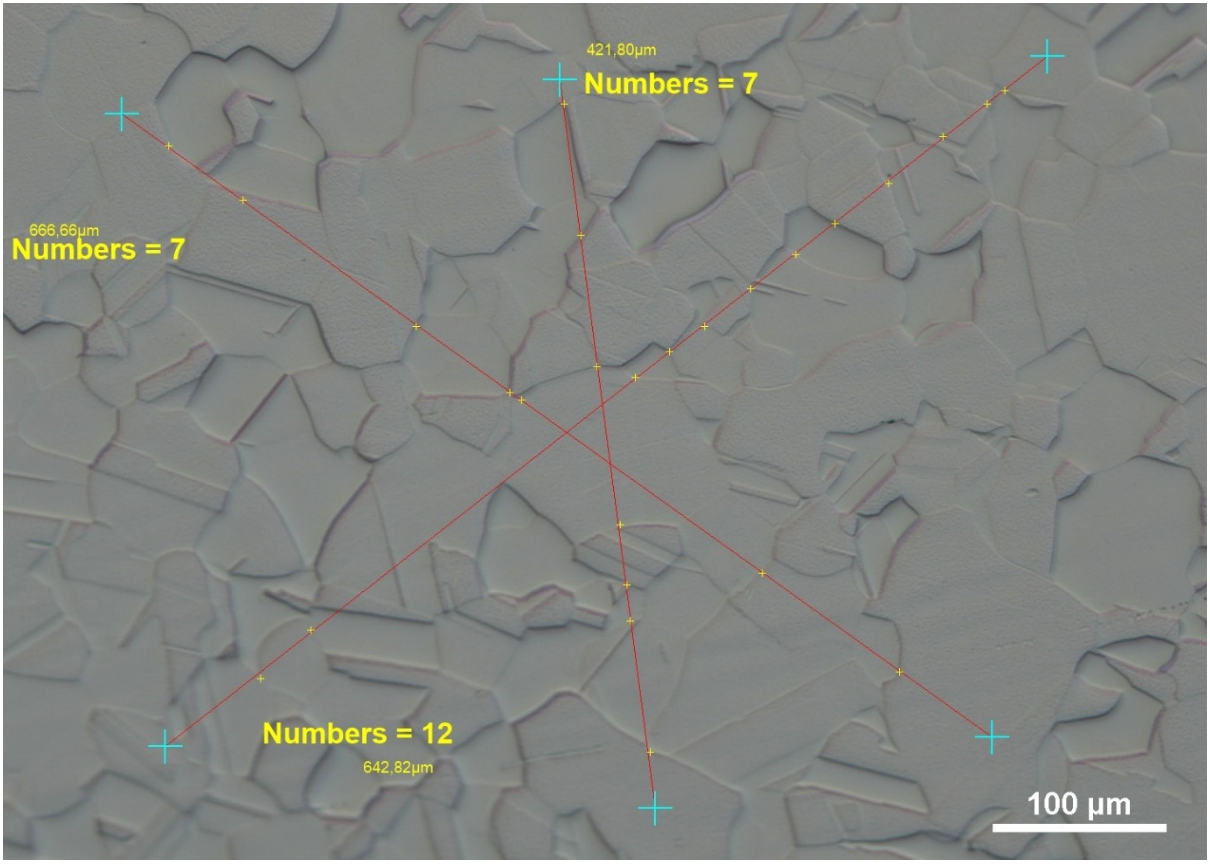

Figure D.13: *316 in the cross-sectional direction, heat treated at 1130℃*

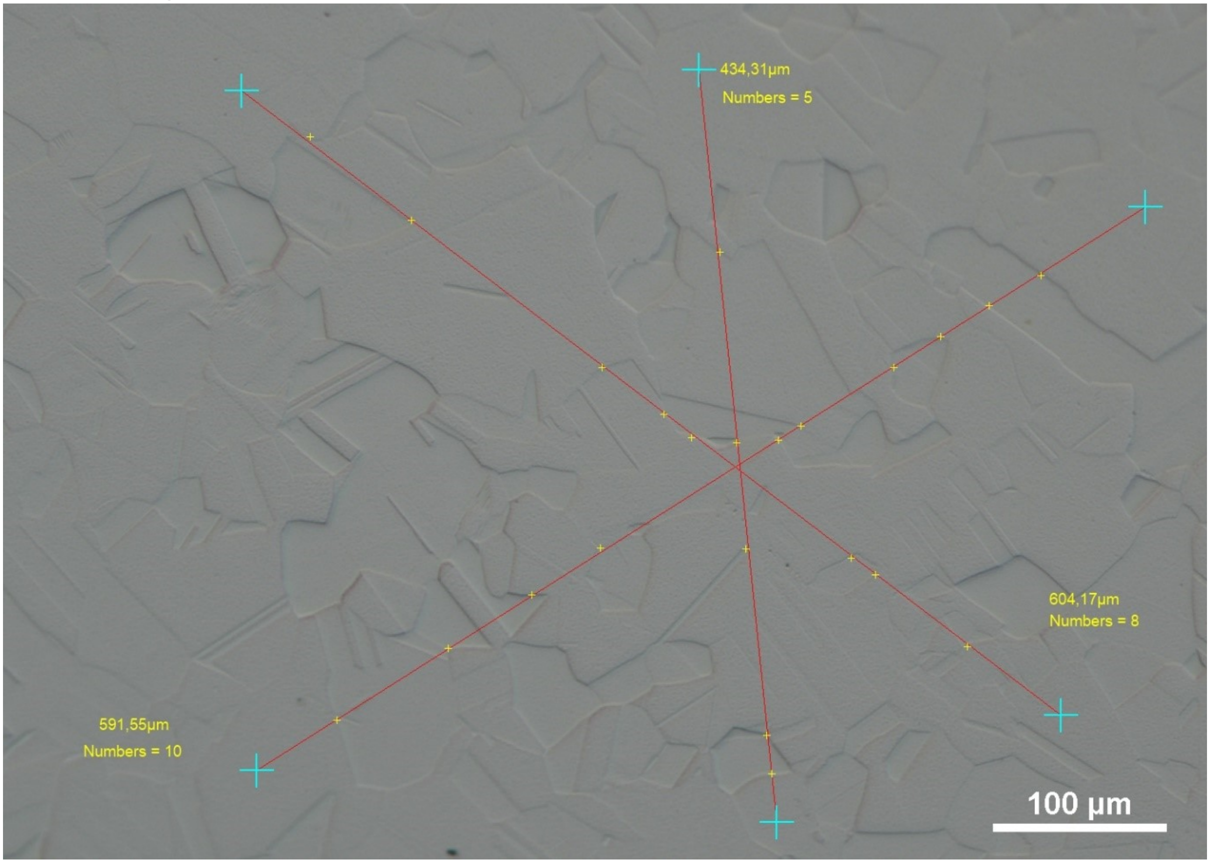

Figure D.14: *316 in the planar direction, heat treated at 1130℃*

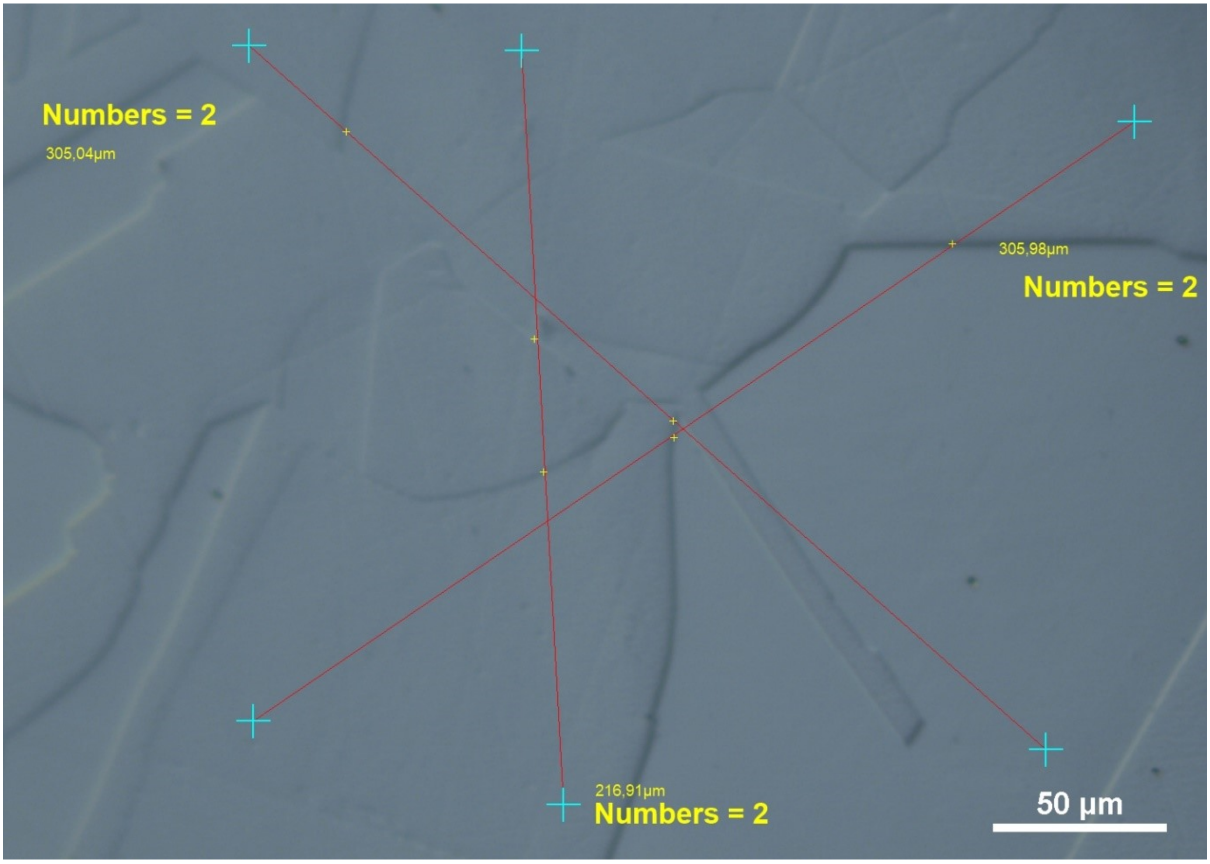

Figure D.15: *304 in the cross-sectional direction, heat treated at 1130℃*

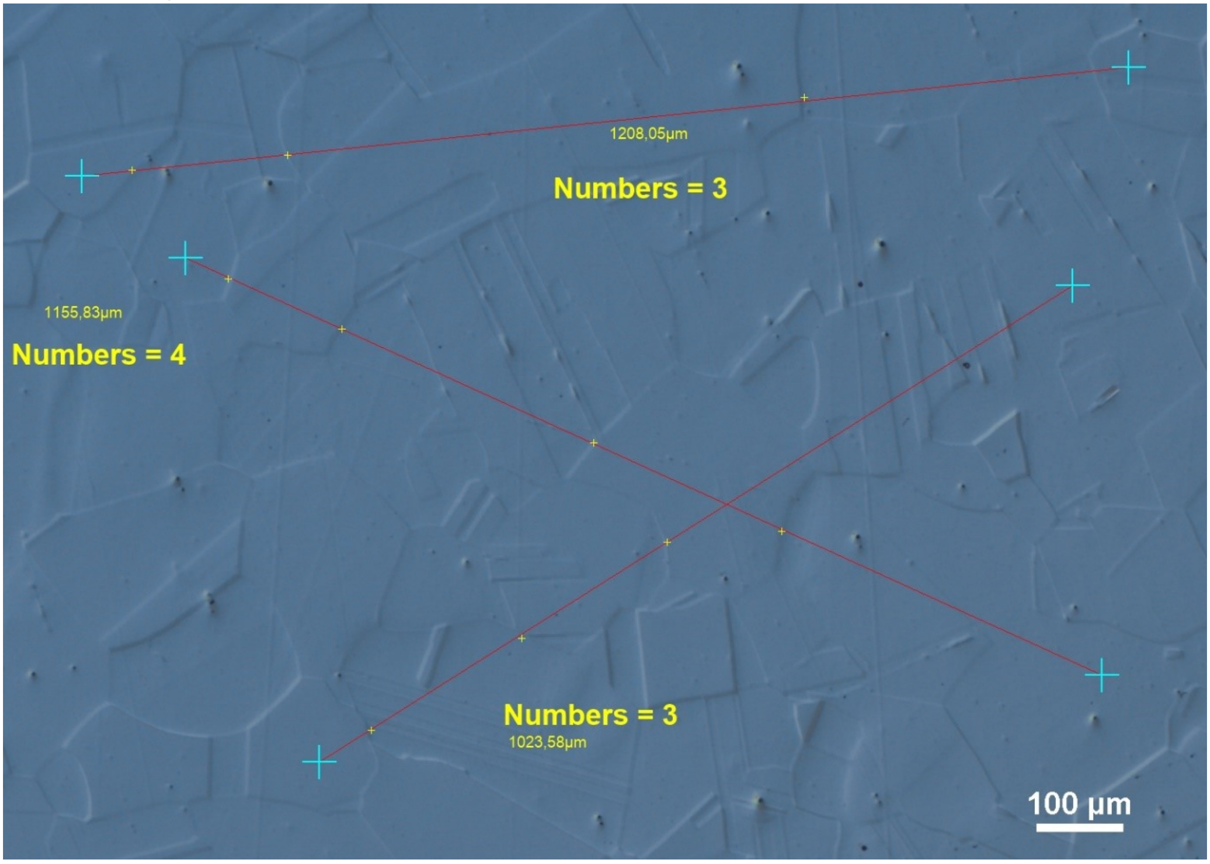

Figure D.16: *304 in the planar direction, heat treated at 1130℃*

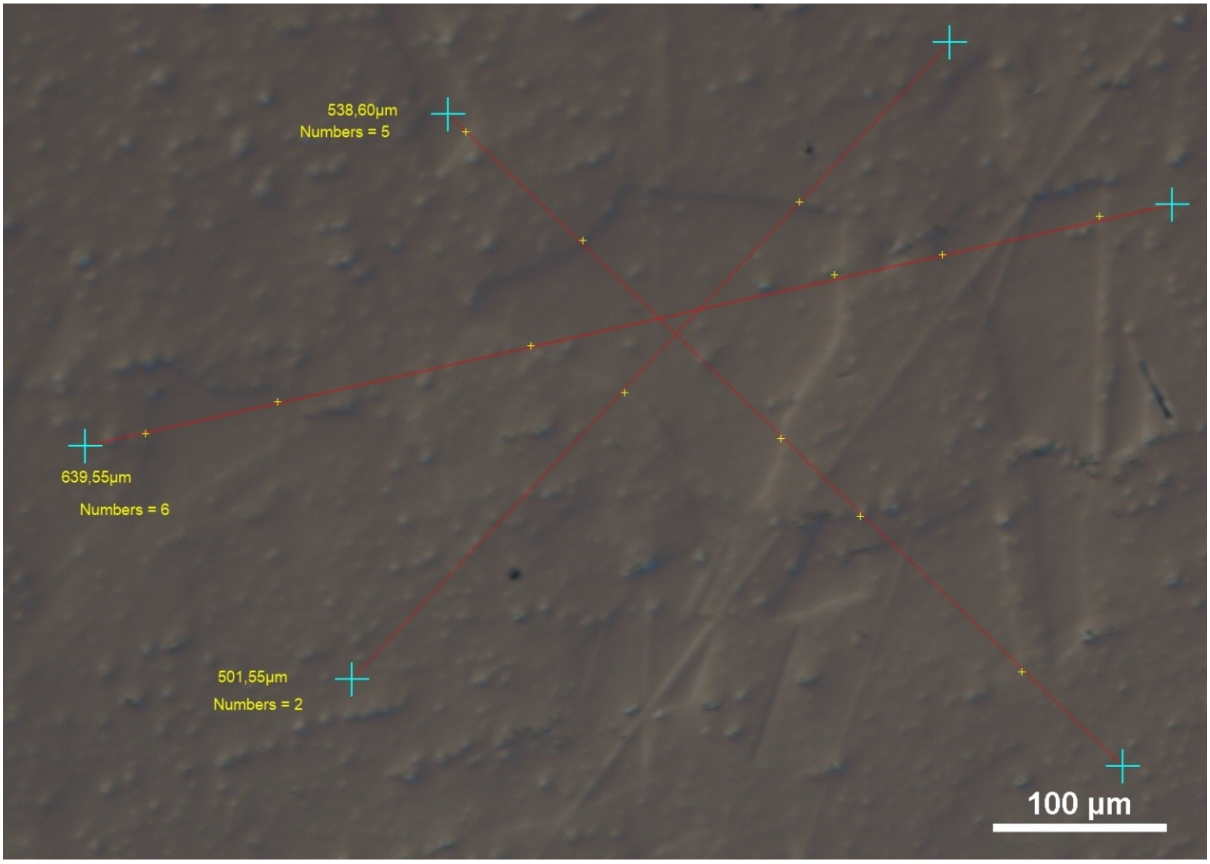

Figure D.17: *347H in the cross-sectional direction, heat treated at 1230℃, with no exposure to nitrogen gas*

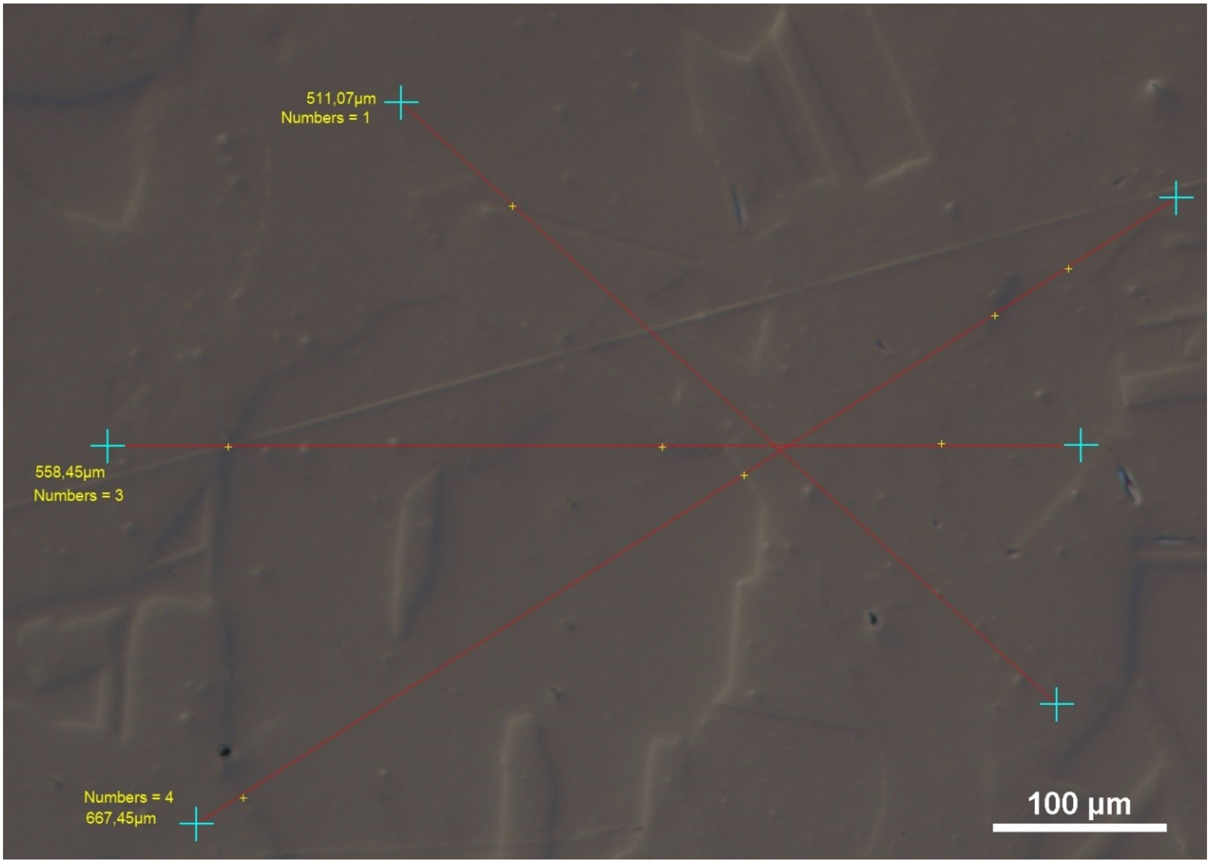

Figure D.18: *347H in the planar direction, heat treated at 1230℃, with no exposure to nitrogen gas*

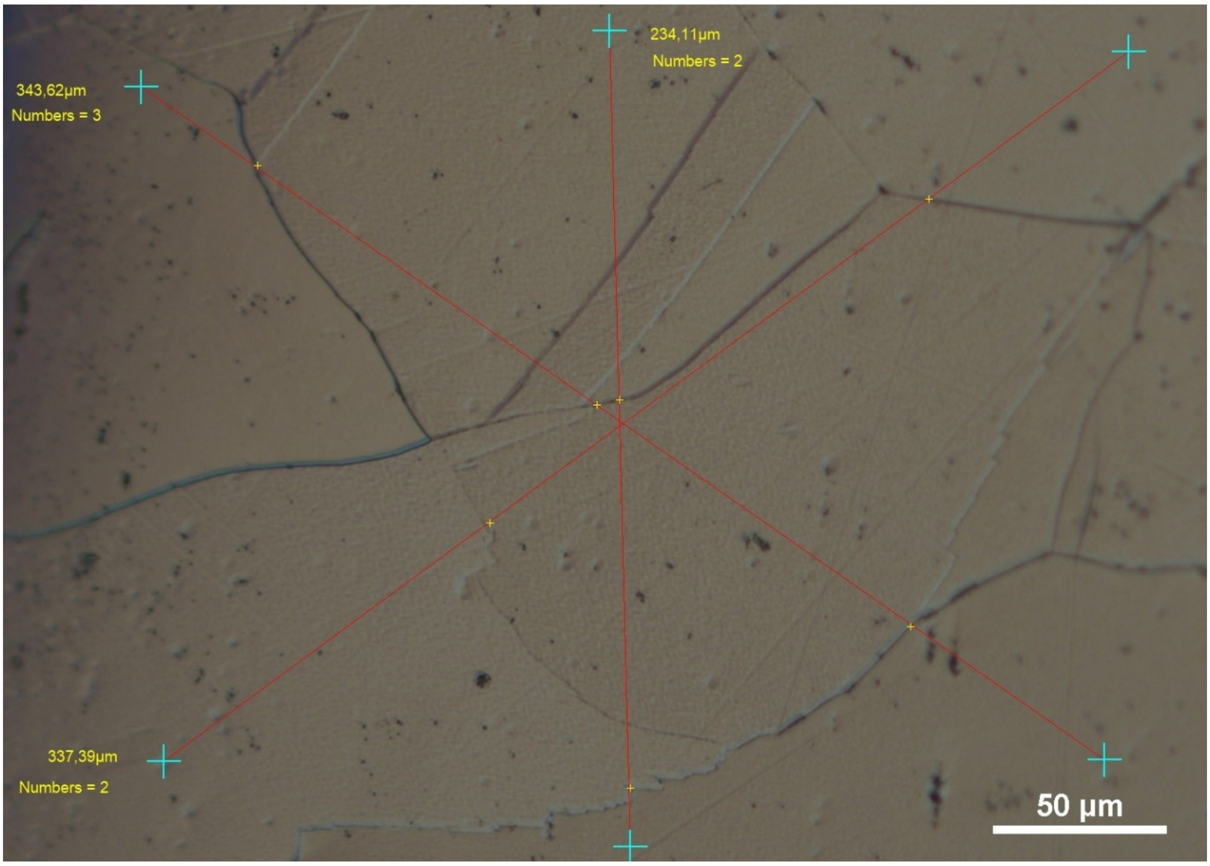

Figure D.19: *321H in the cross-sectional direction, heat treated at 1230℃, with no exposure to nitrogen gas*

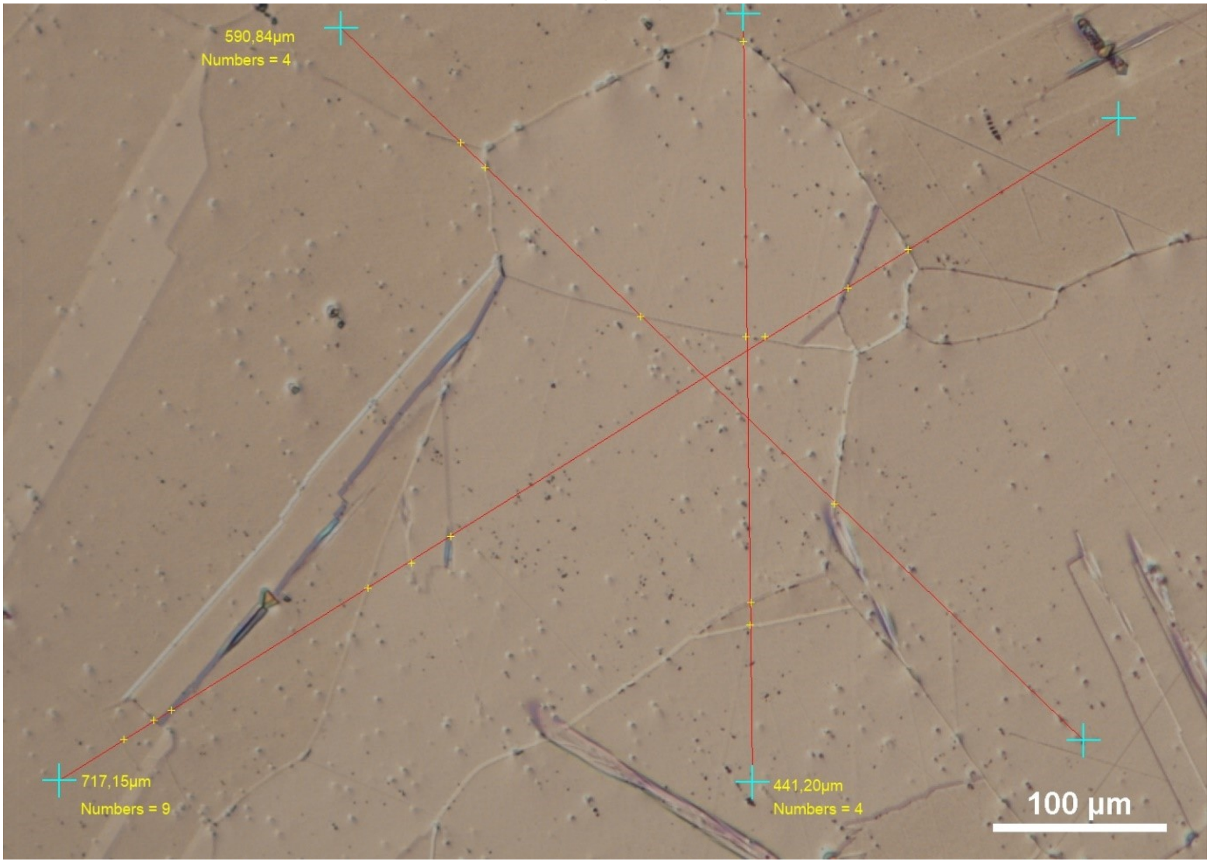

Figure D.20: *321H in the planar direction, heat treated at 1230℃, with no exposure to nitrogen gas*

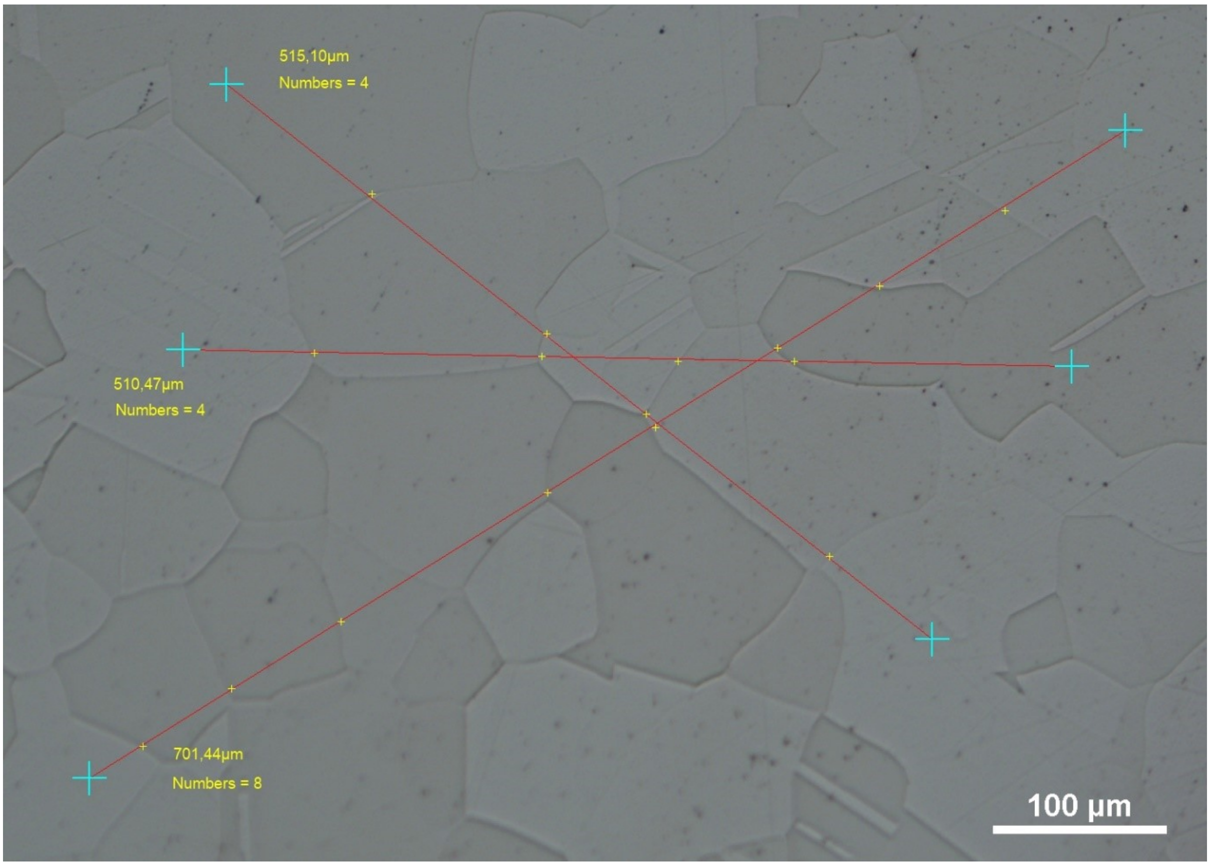

Figure D.21: *316 in the cross-sectional direction, heat treated at 1230℃, with no exposure to nitrogen gas*

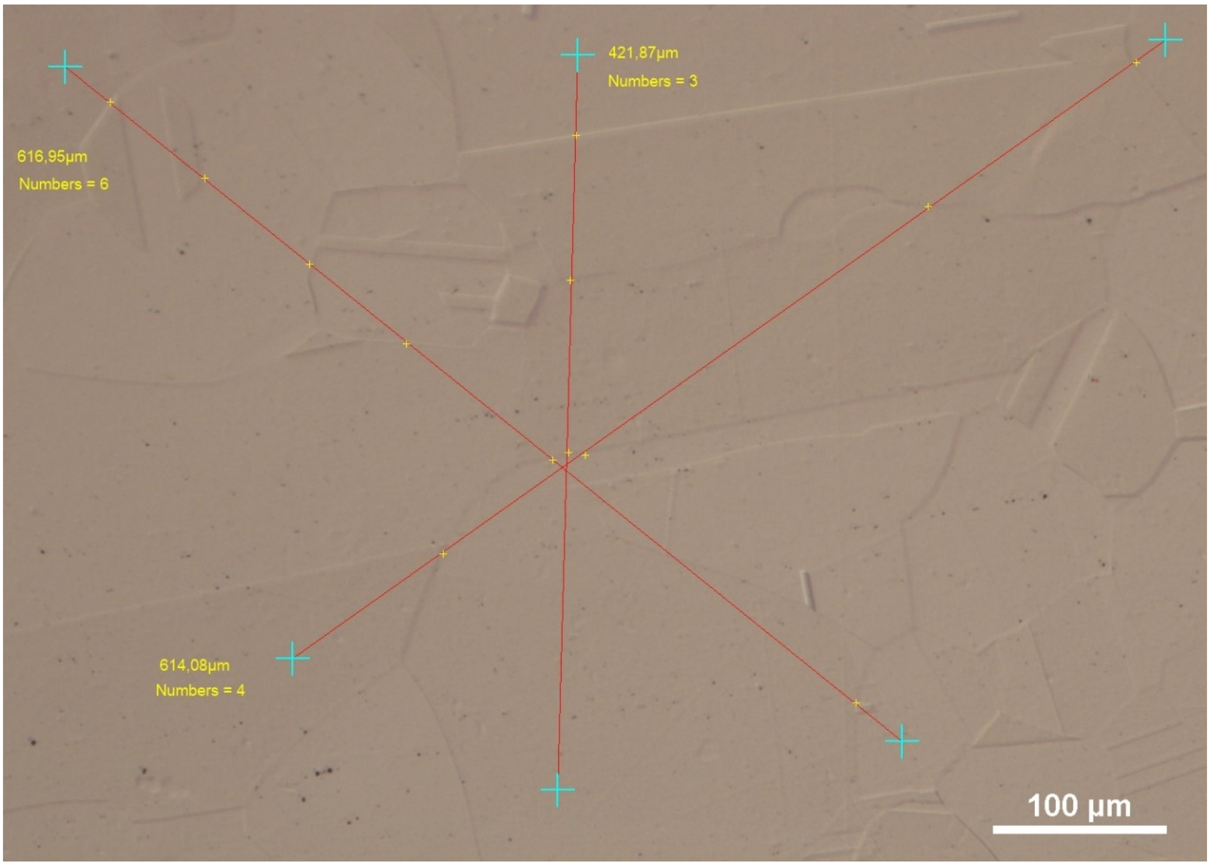

Figure D.22: *316 in the planar direction, heat treated at 1230°C, with no exposure to nitrogen gas*

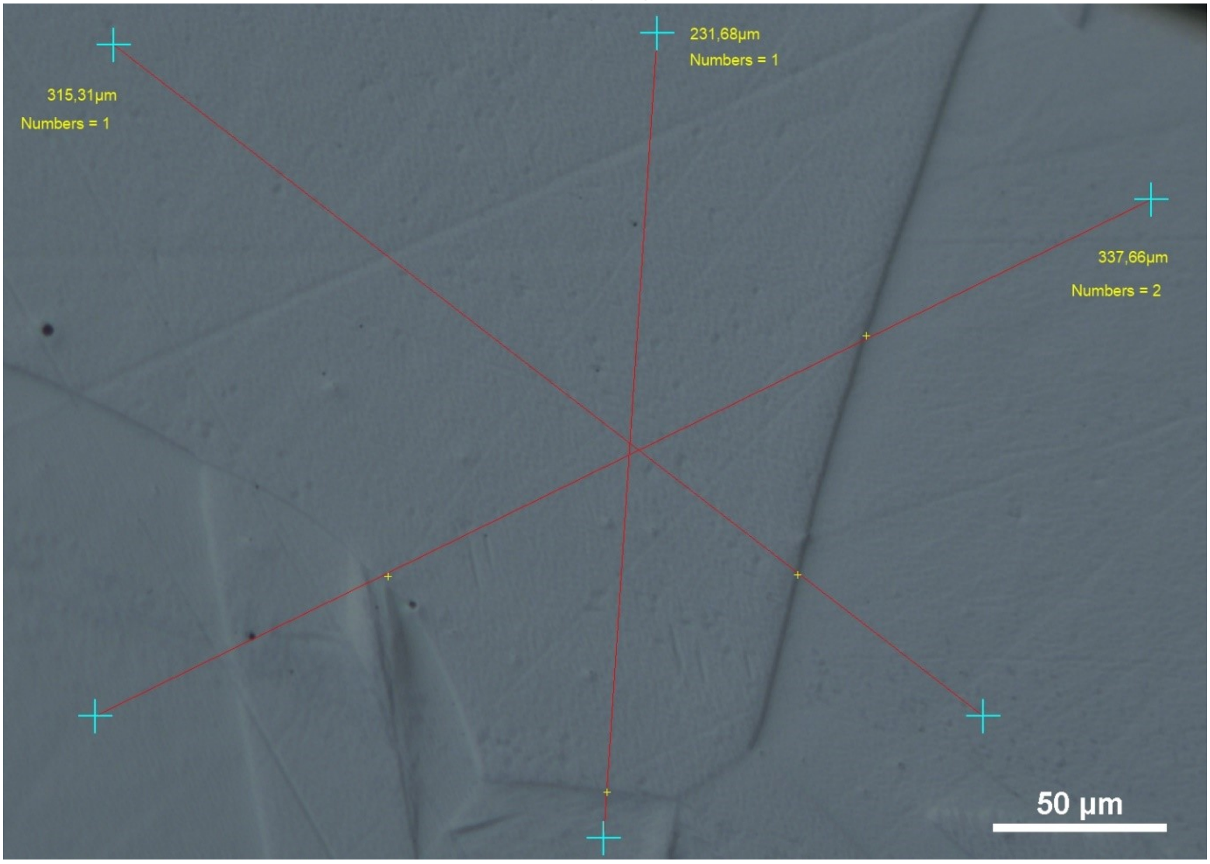

Figure D.23: *304 in the cross-sectional direction, heat treated at 1230℃, with no exposure to nitrogen gas*

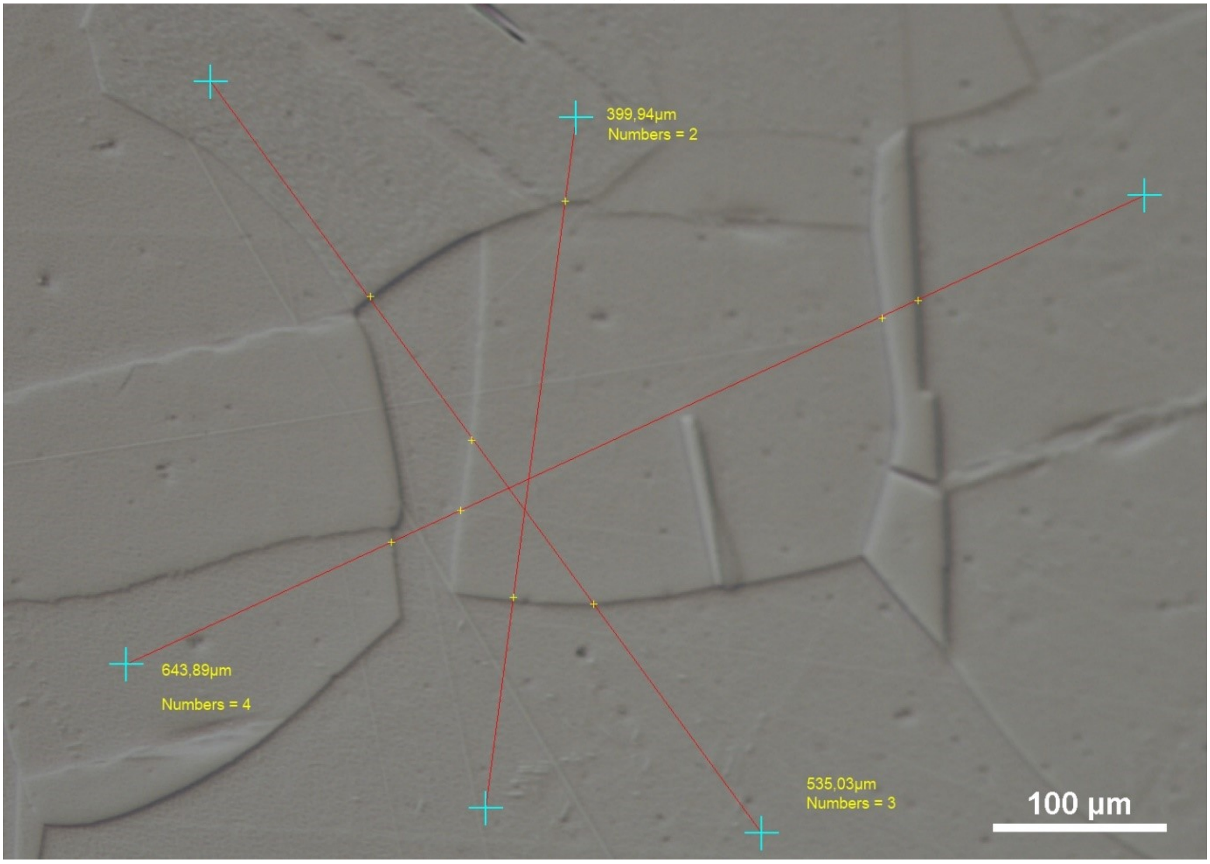

Figure D.24: *304 in the planar direction, heat treated at 1230℃, with no exposure to nitrogen gas*

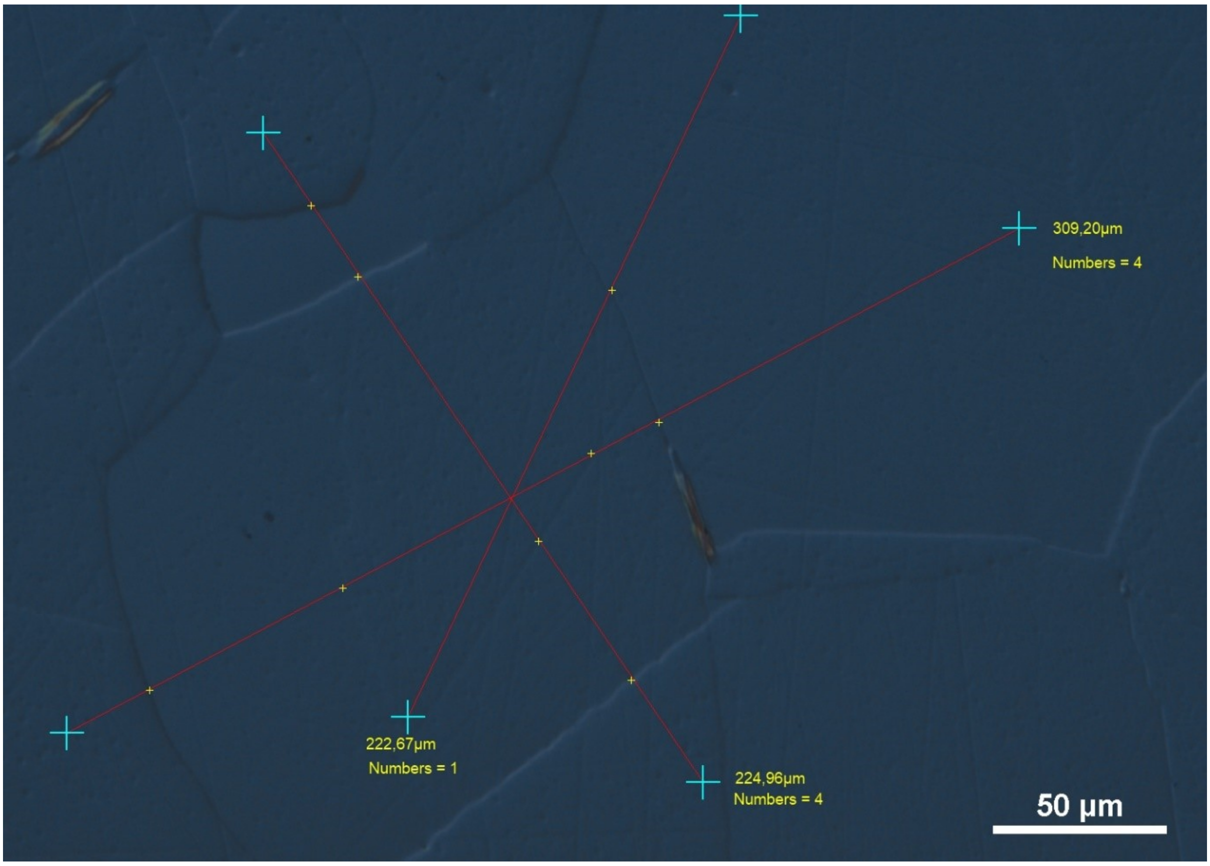

Figure D.25: *347H in the cross-sectional direction, heat treated at 1230℃, with exposure to nitrogen gas*

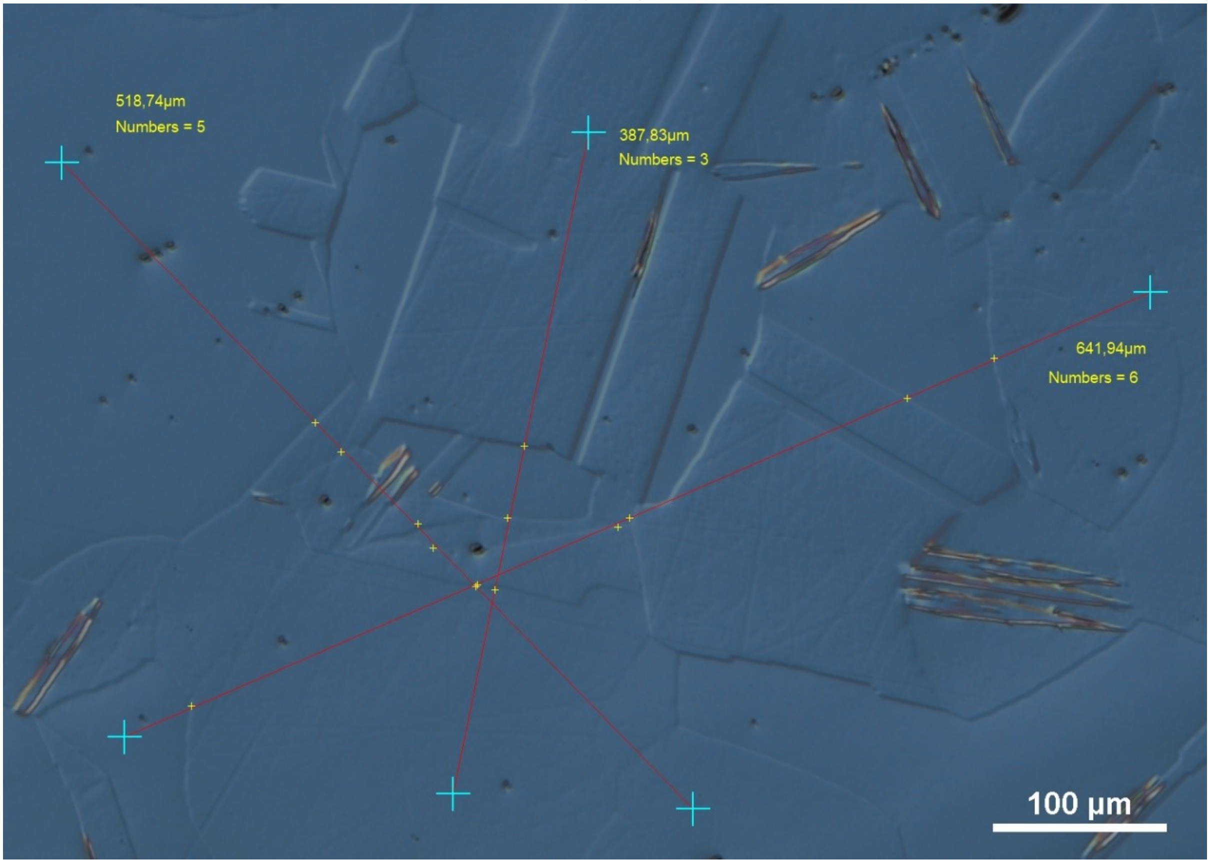

Figure D.26: *347H in the planar direction, heat treated at 1230℃, with exposure to nitrogen gas*

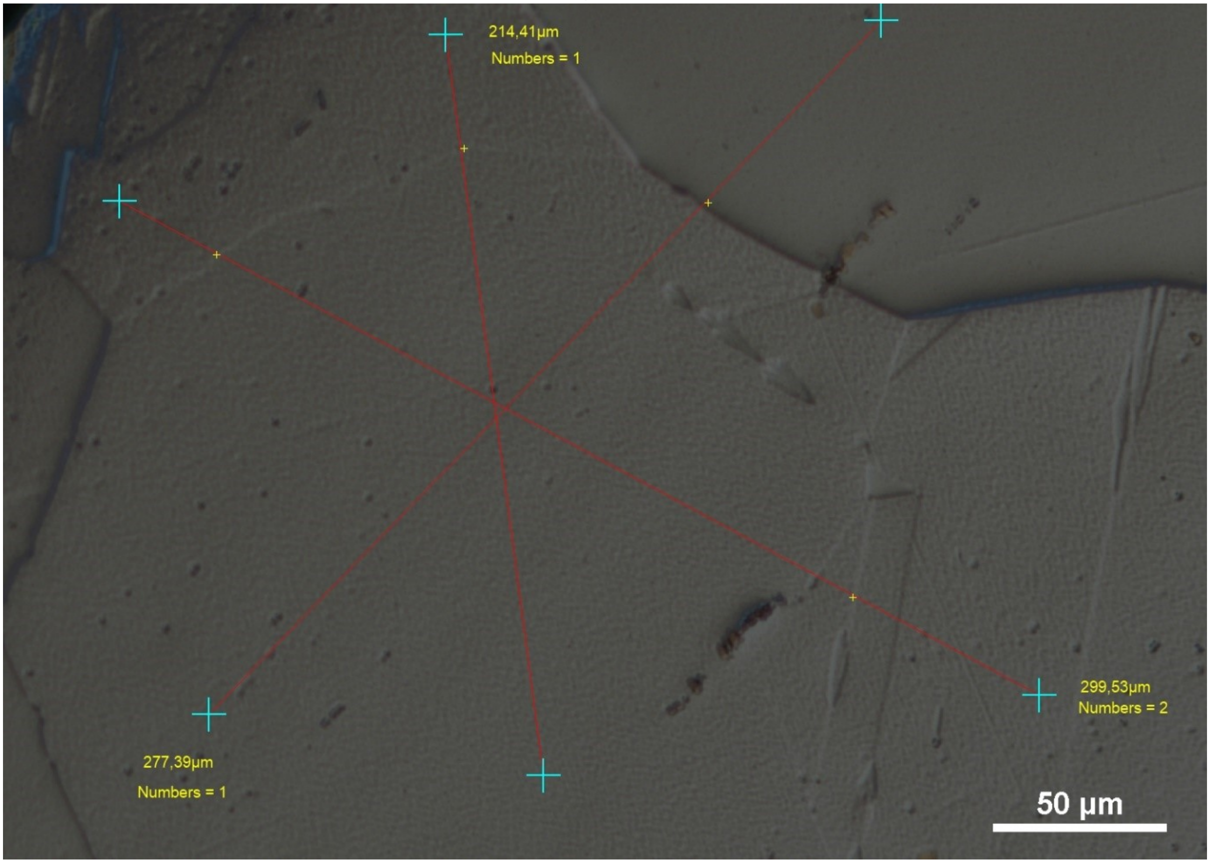

Figure D.27: *321H in the cross-sectional direction, heat treated at 1230℃, with exposure to nitrogen gas*

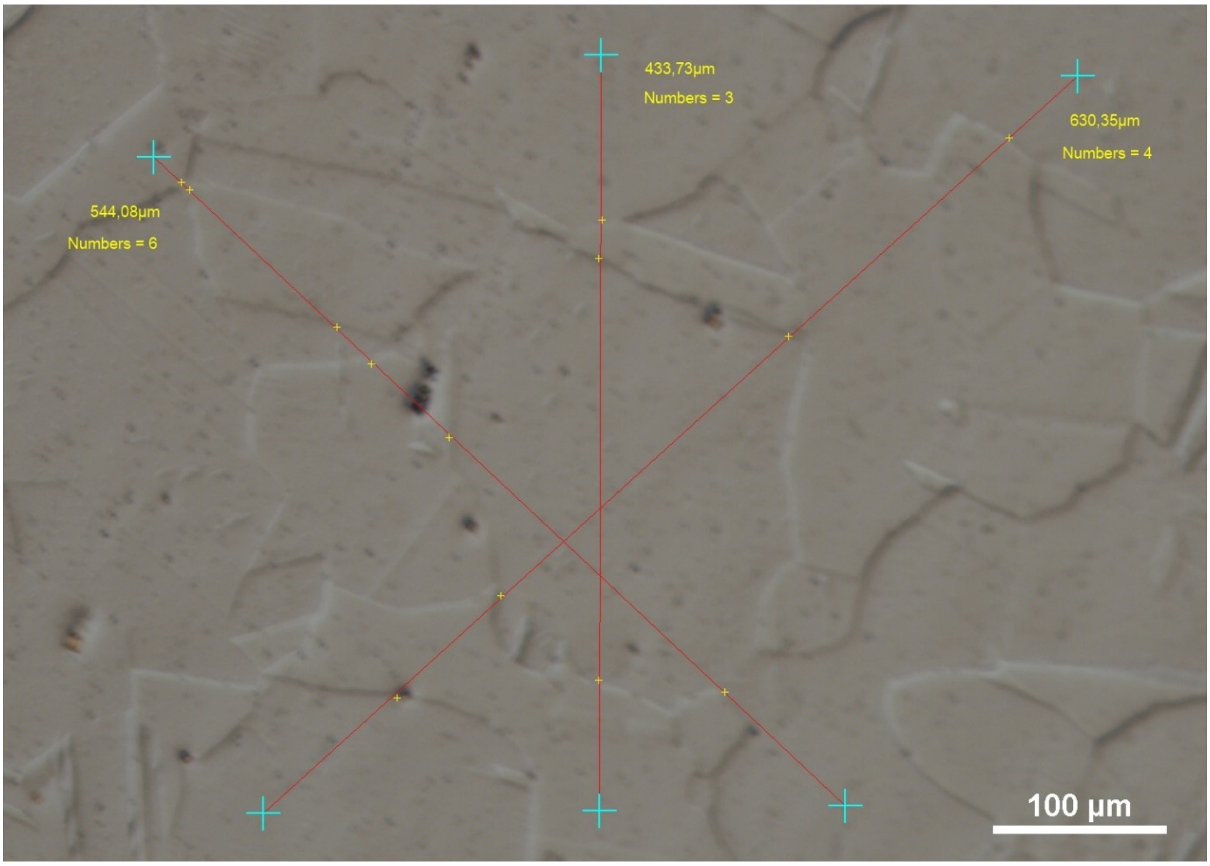

Figure D.28: *321H in the planar direction, heat treated at 1230℃, with exposure to nitrogen gas*

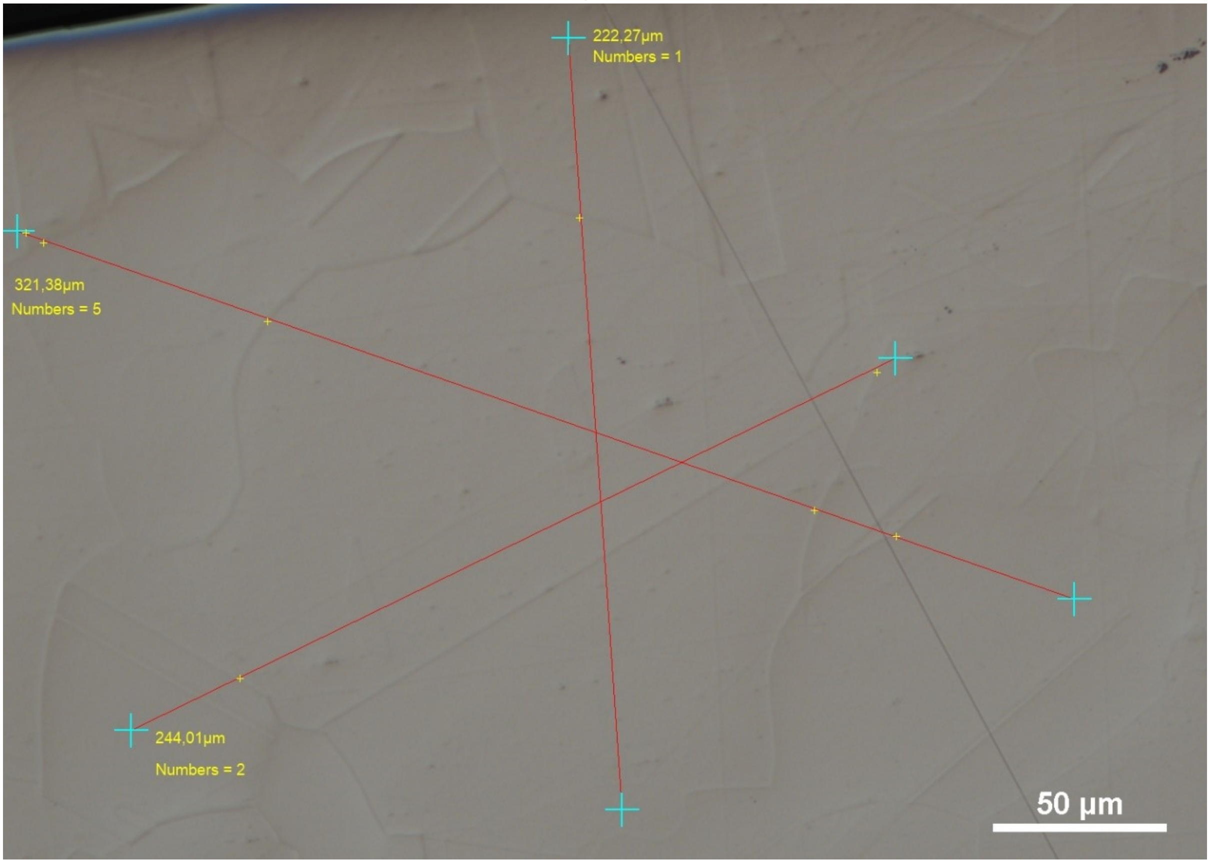

Figure D.29: *316 in the cross-sectional direction, heat treated at 1230℃, with exposure to* *nitrogen gas*

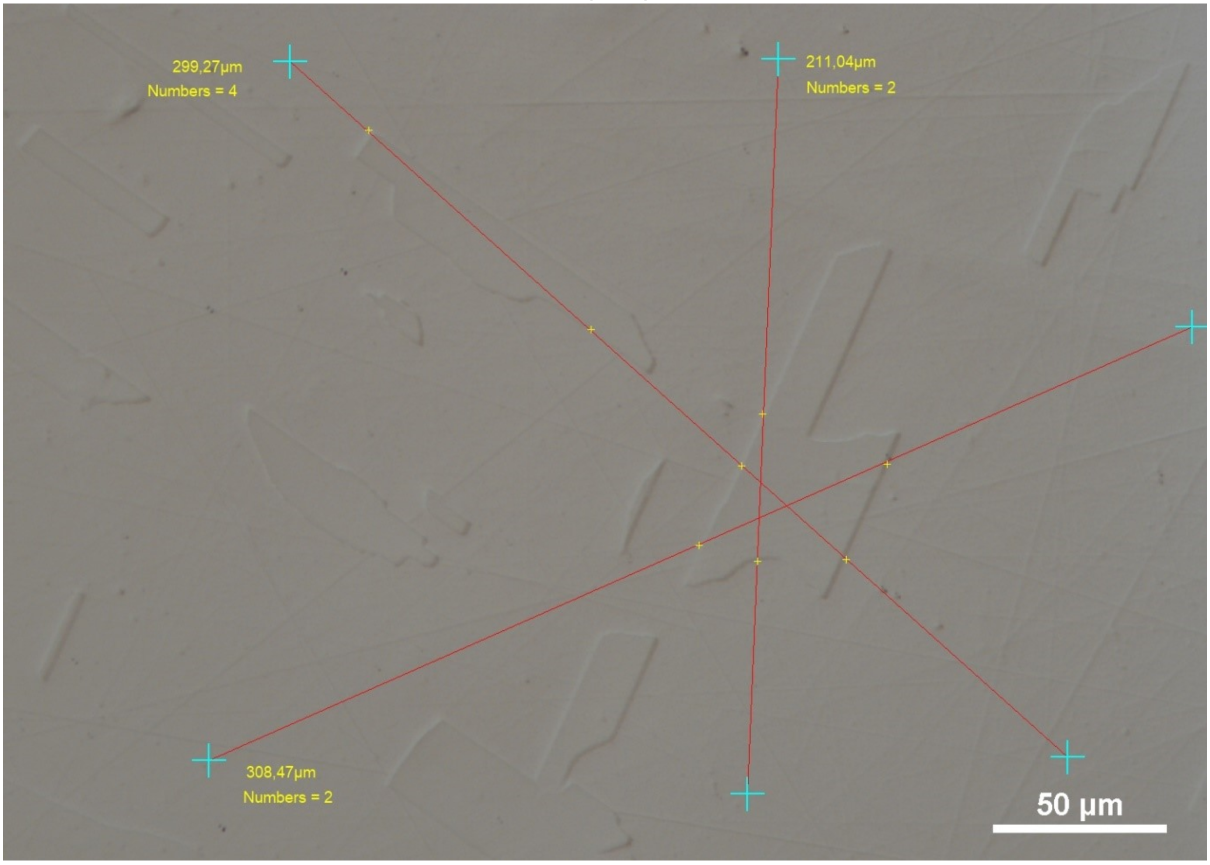

Figure D.30: *316 in the planar direction, heat treated at 1230°C, with exposure to nitrogen gas*

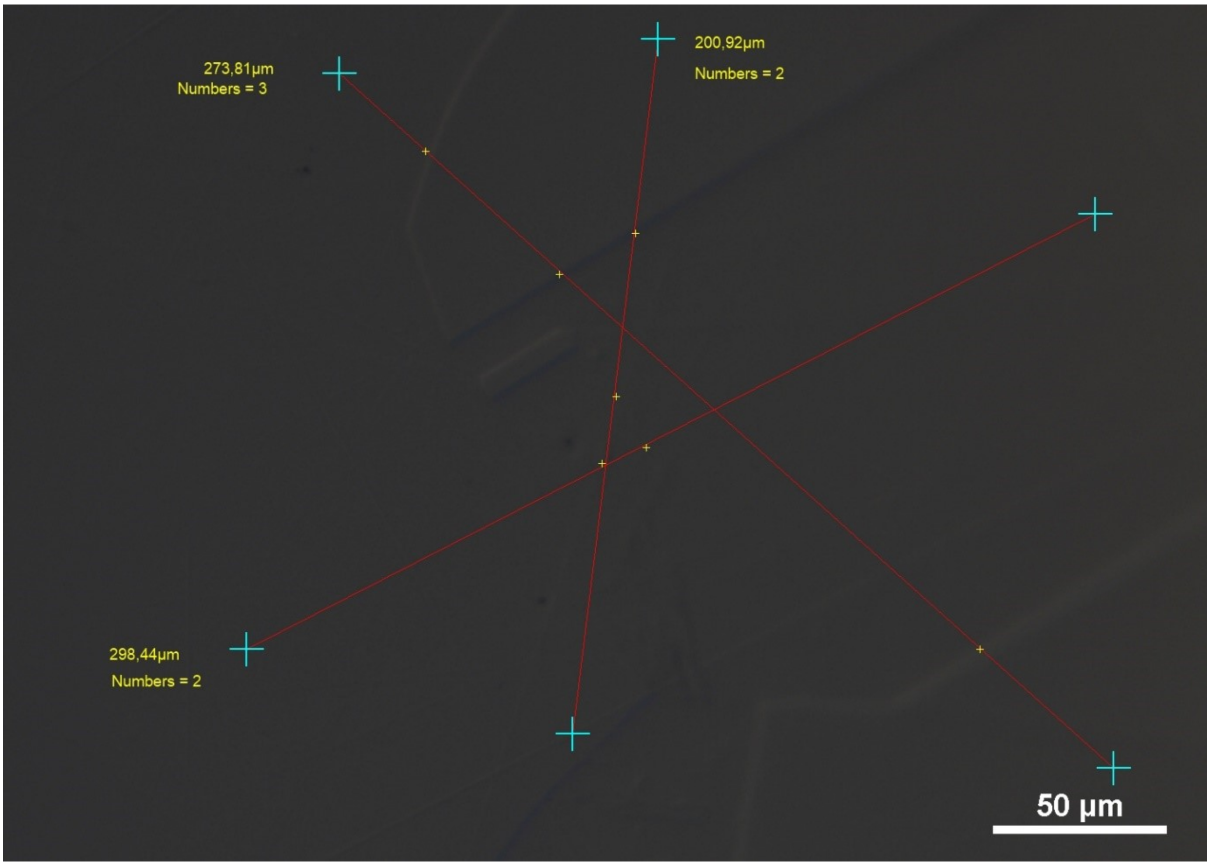

Figure D.31: *304 in the cross-sectional direction, heat treated at 1230℃, with exposure to nitrogen gas*

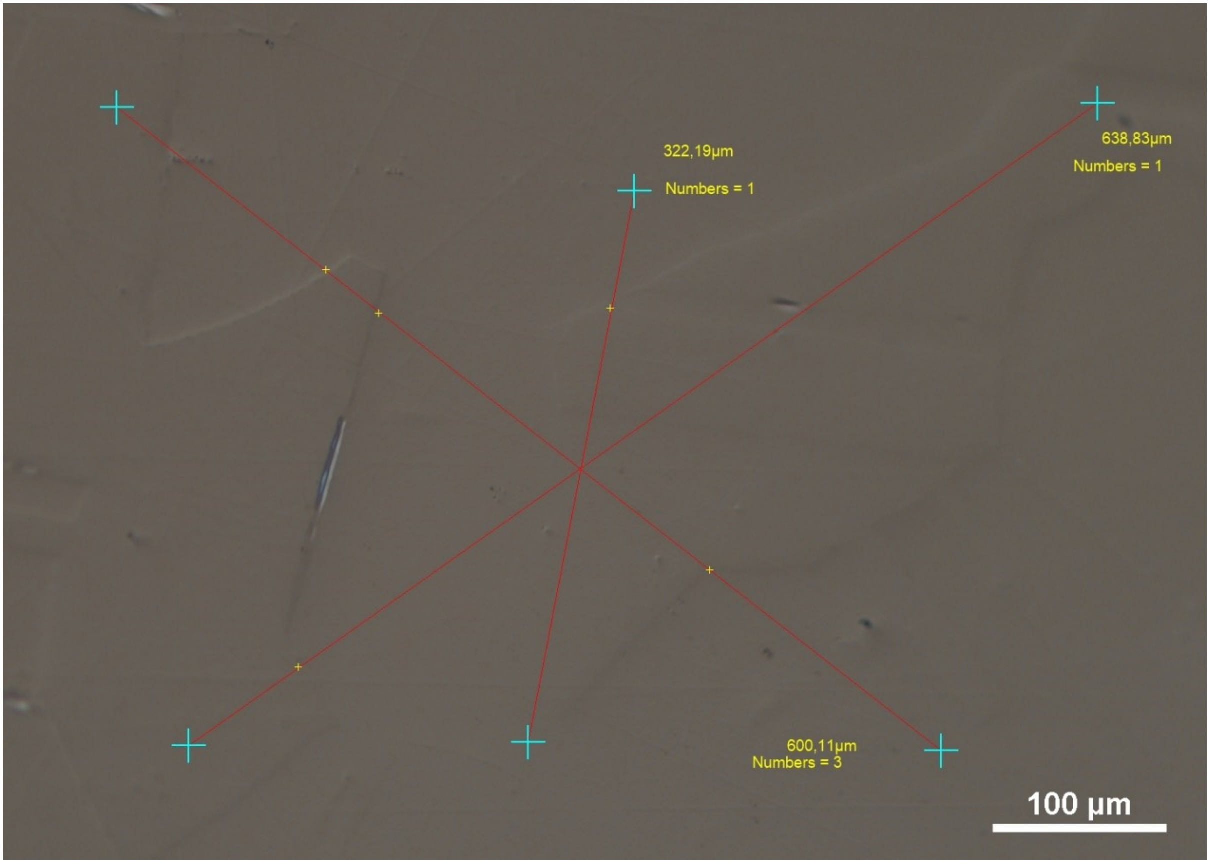

Figure D.32: *304 in the planar direction, heat treated at 1230℃, with exposure to nitrogen gas*

Appendix E

There are two areas investigated for each sample, named as the first and secondary area given in the following figures.

321H

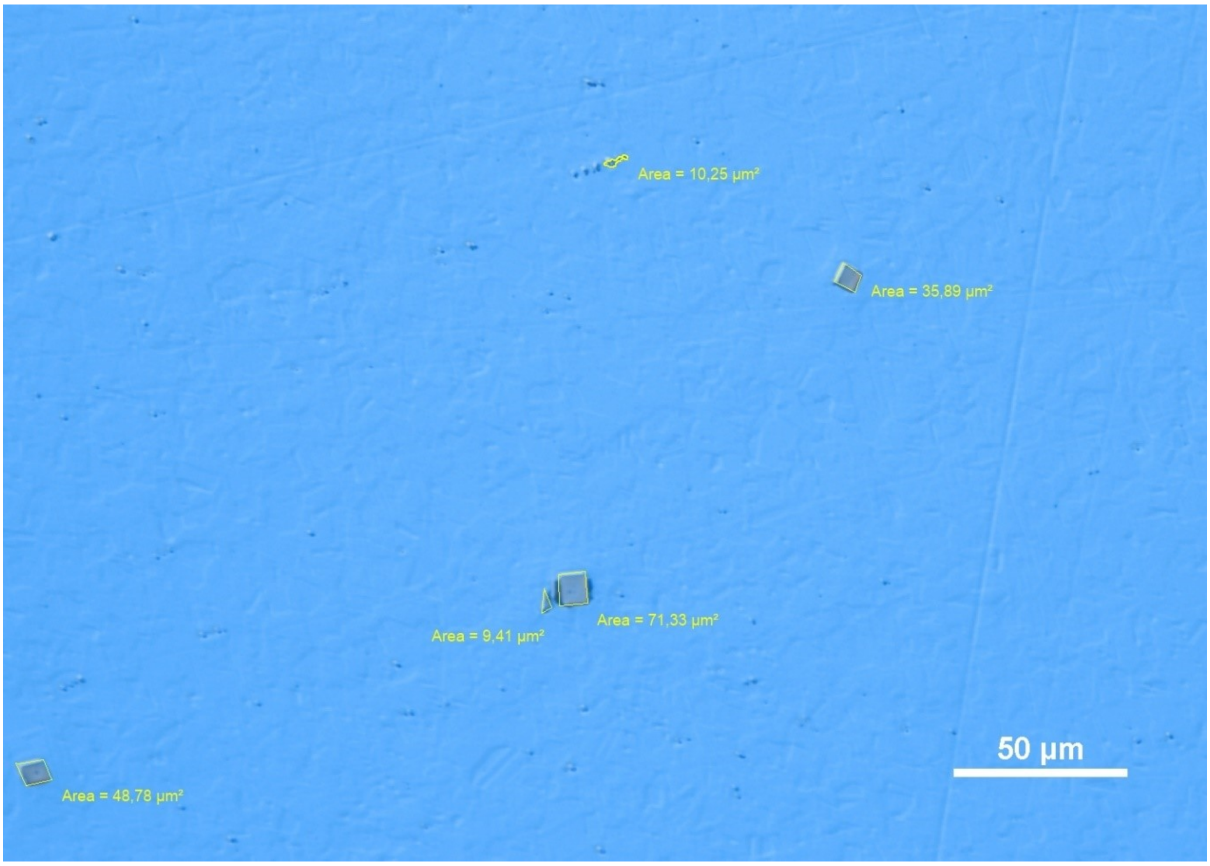

Figure E.1: *321H first area particles, kept at room temperature. Planar view*

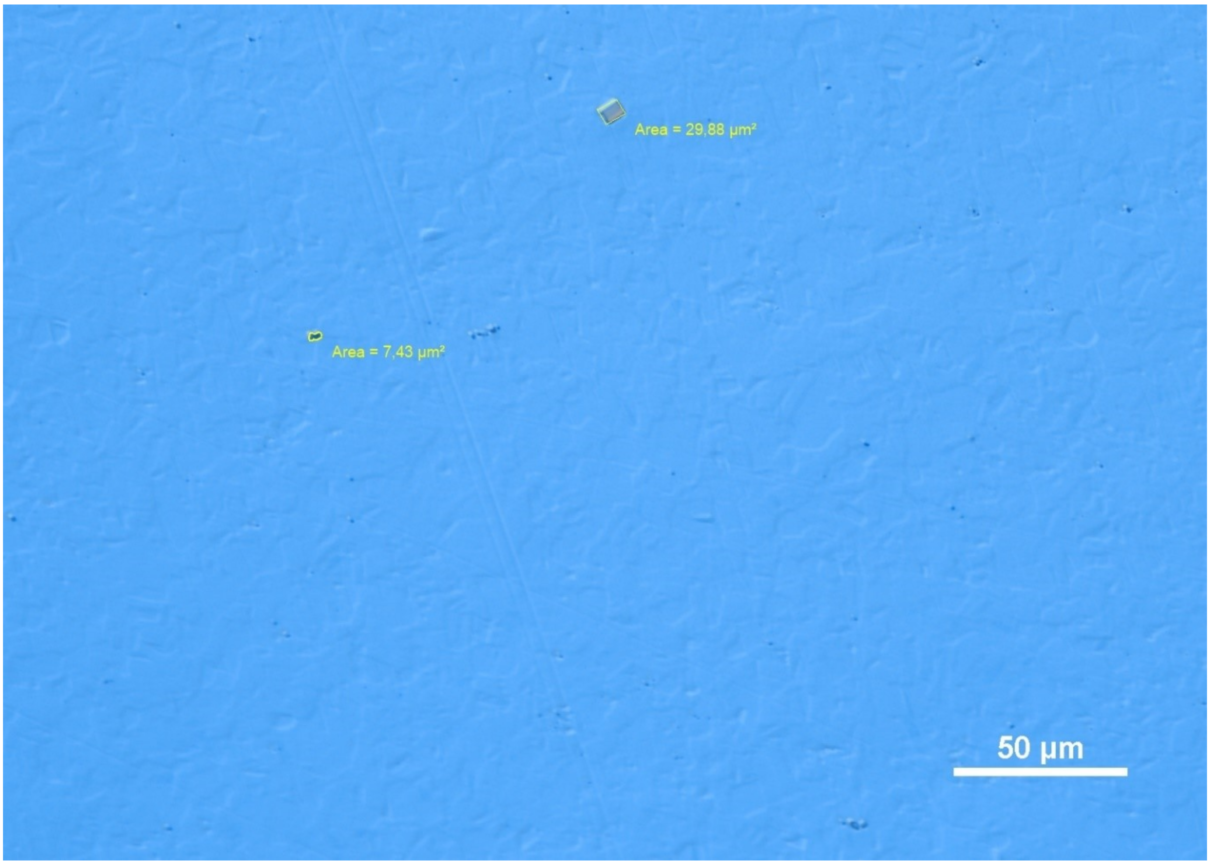

Figure E.2: *321H secondary area particles, kept at room temperature. Planar view*

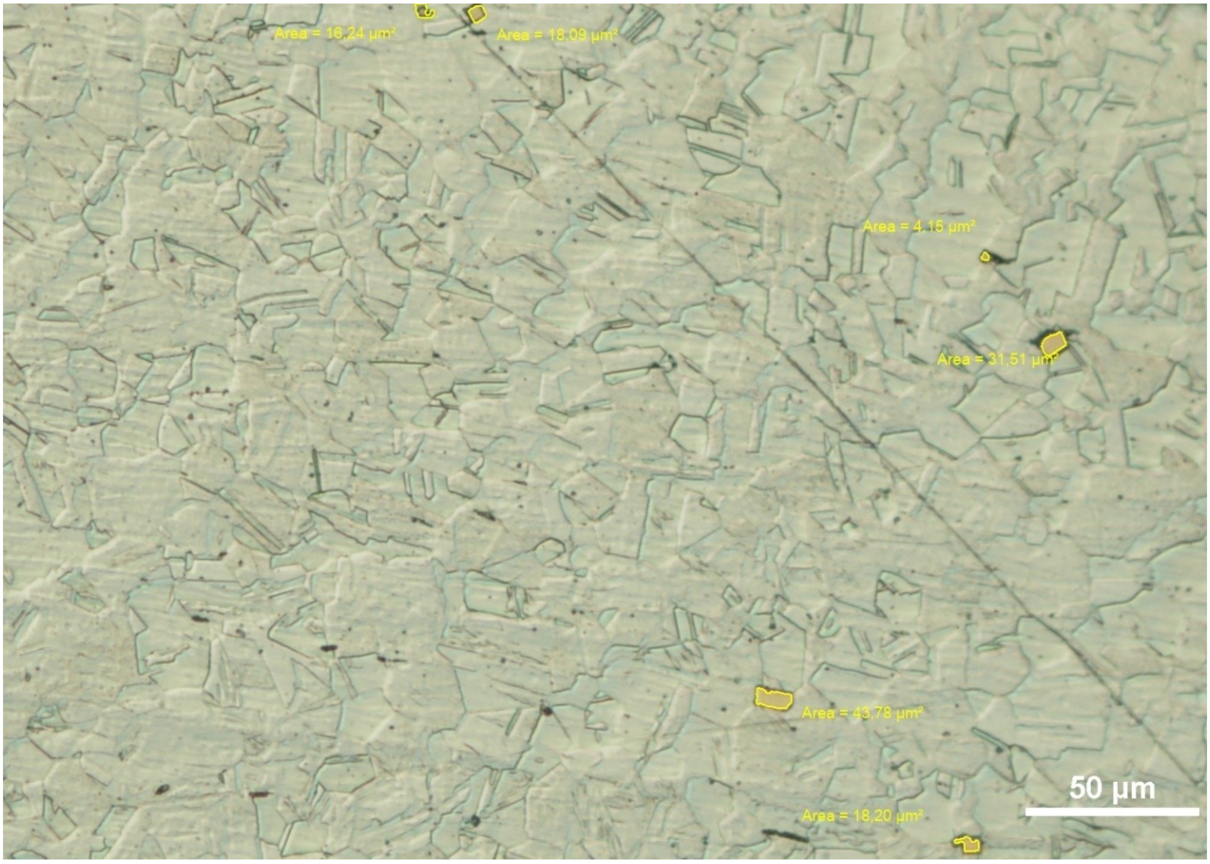

Figure E.3: *321H first area particles, kept at room temperature. Cross-sectional view*

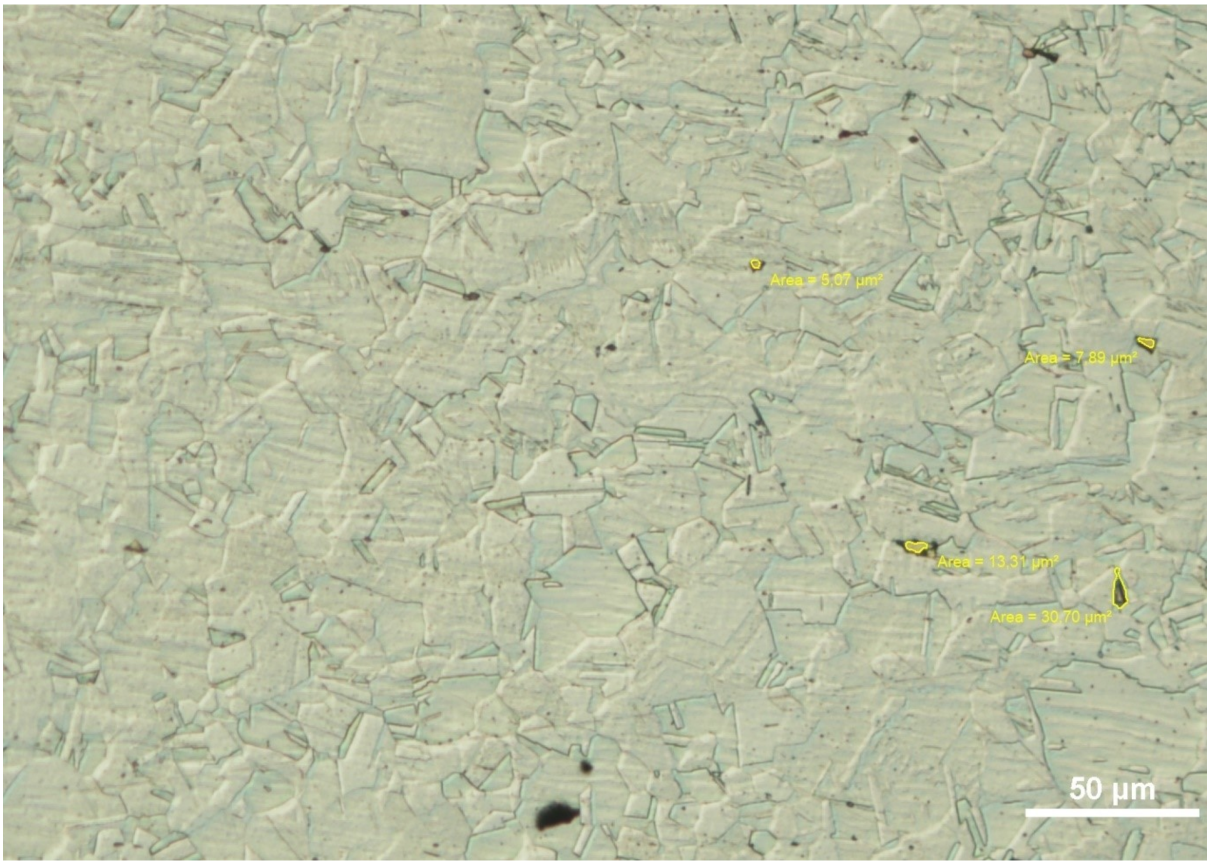

Figure E.4: *321H secondary area particles, kept at room temperature. Cross-sectional view*

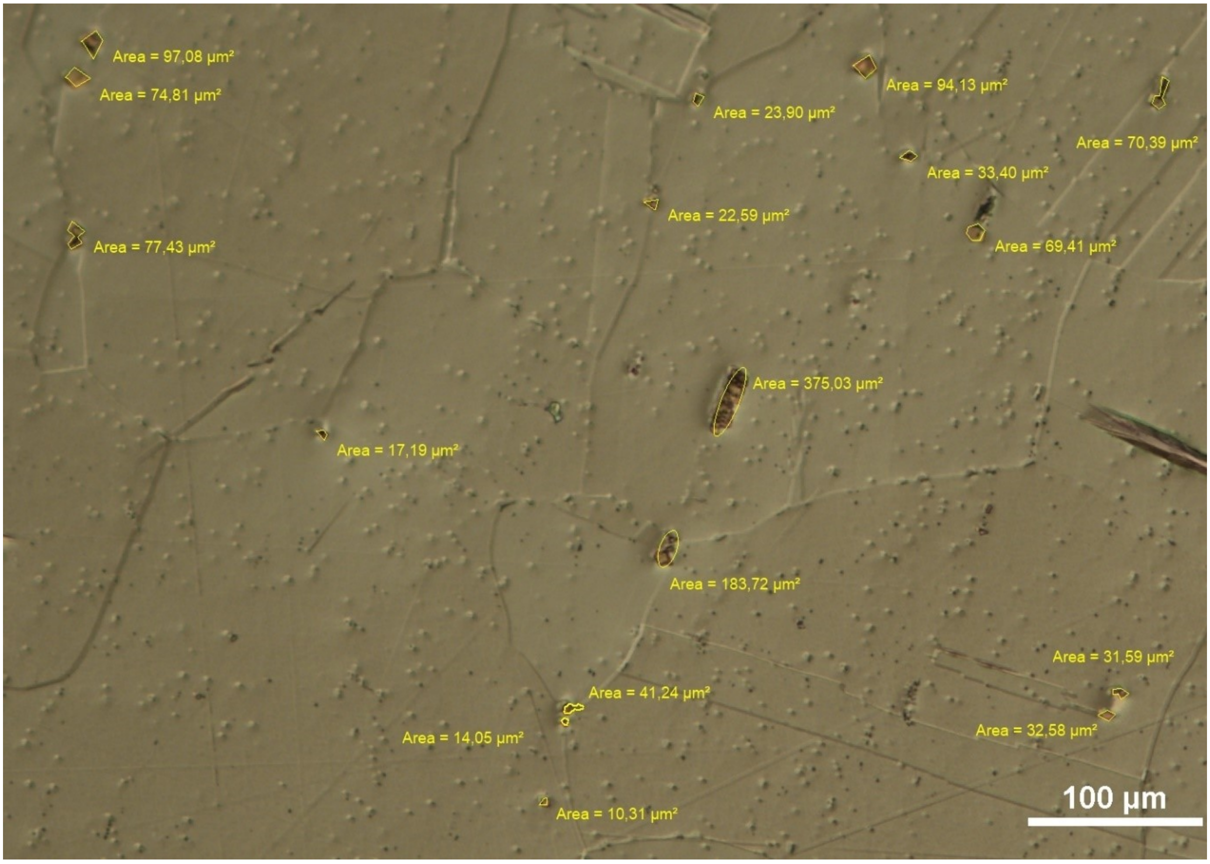

Figure E.5: *321H first area particles, heat treated at 1230°C. Planar view*

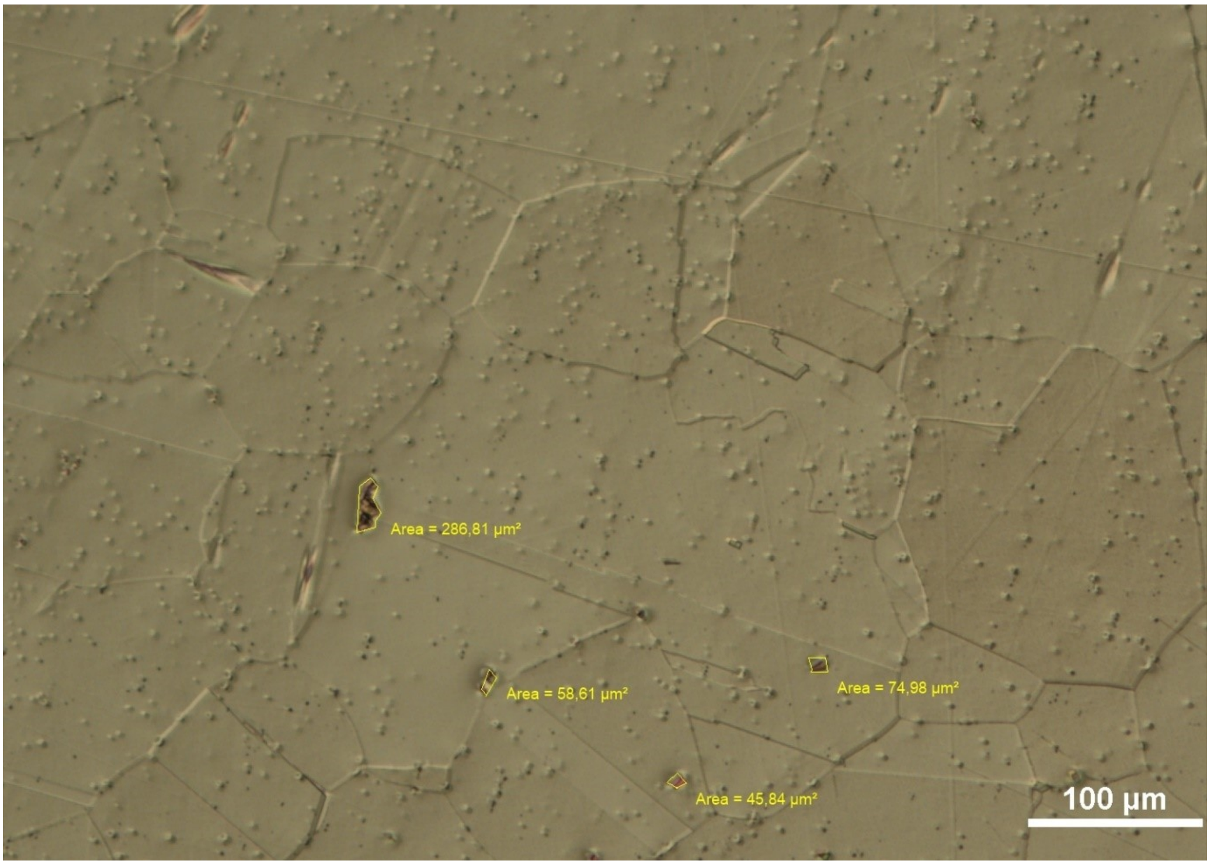

Figure E.6: *321H secondary area particles, heat treated at 1230℃. Planar view*

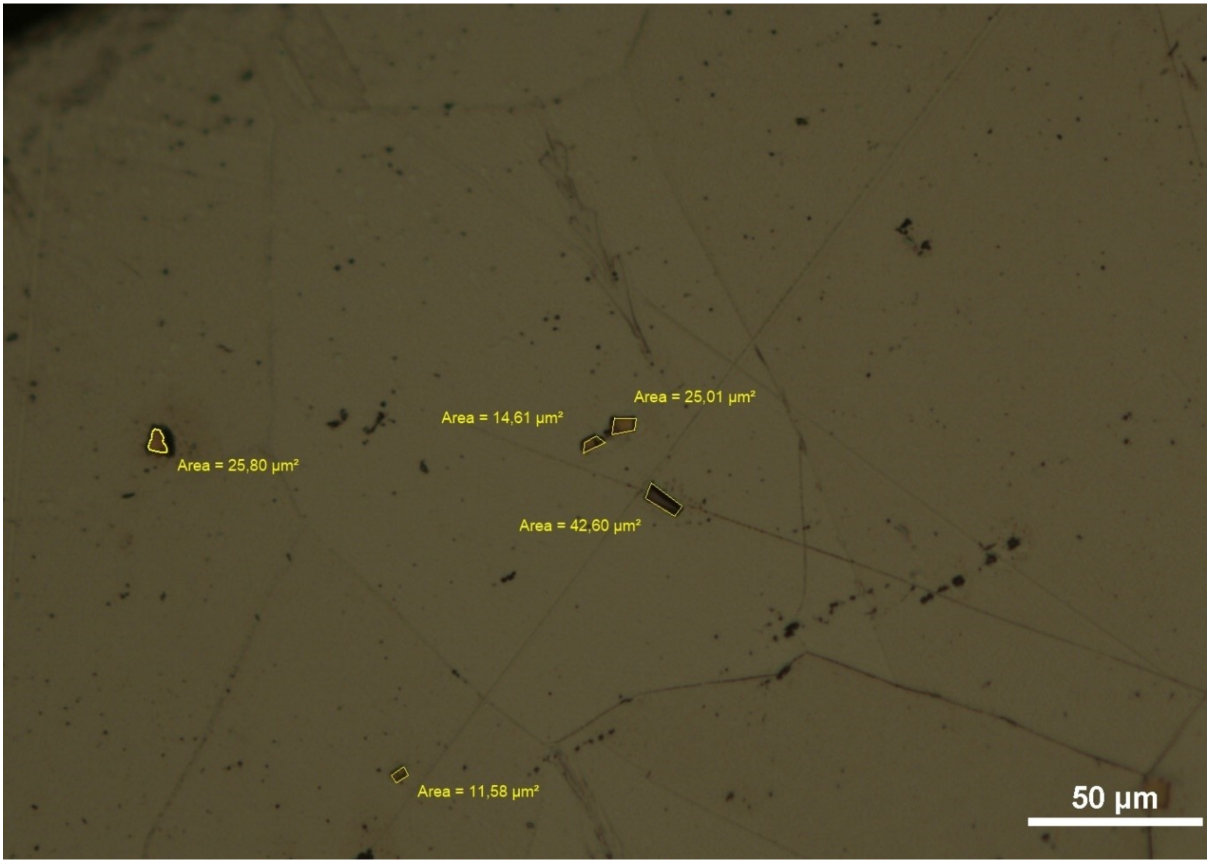

Figure E.7: *321H first area particles, heat treated at 1230℃. Cross-sectional view*

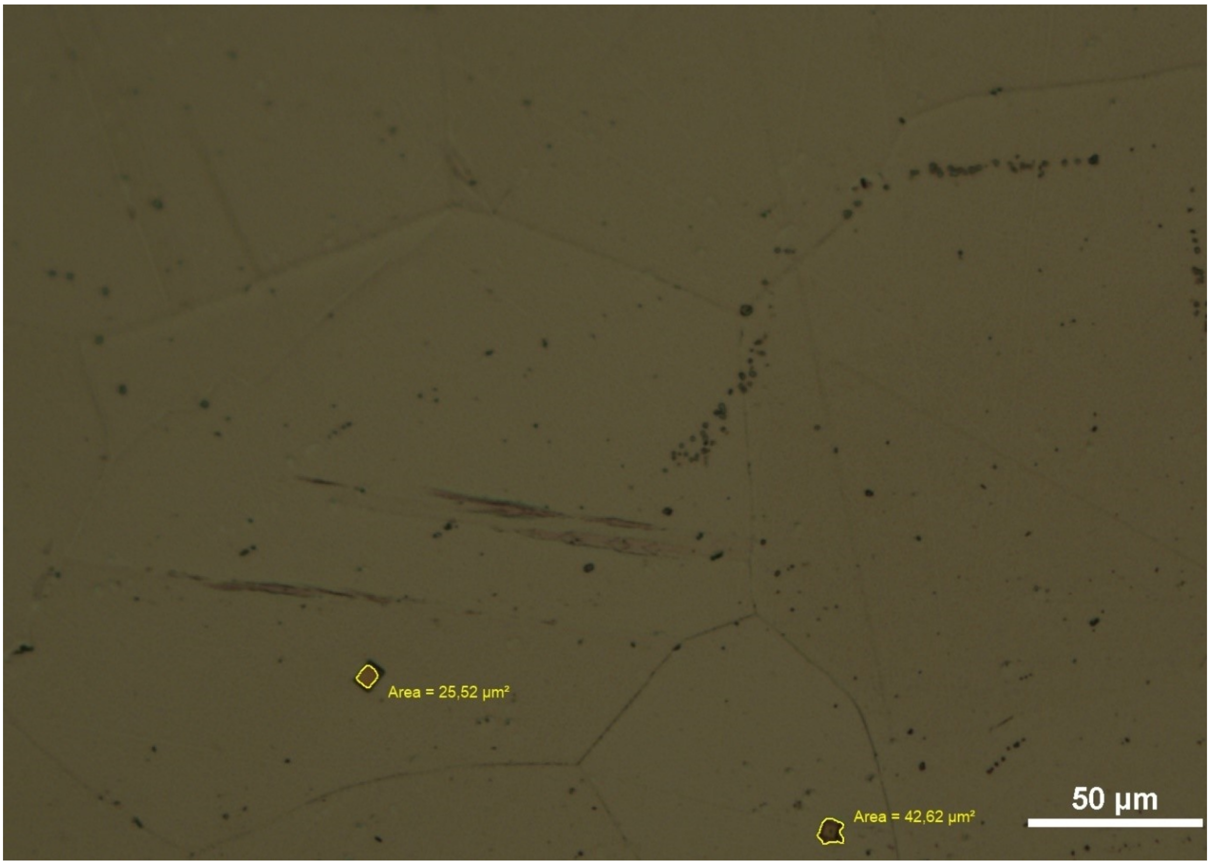

Figure E.8: *321H secondary area particles, heat treated at 1230°C. Cross-sectional view*

347H

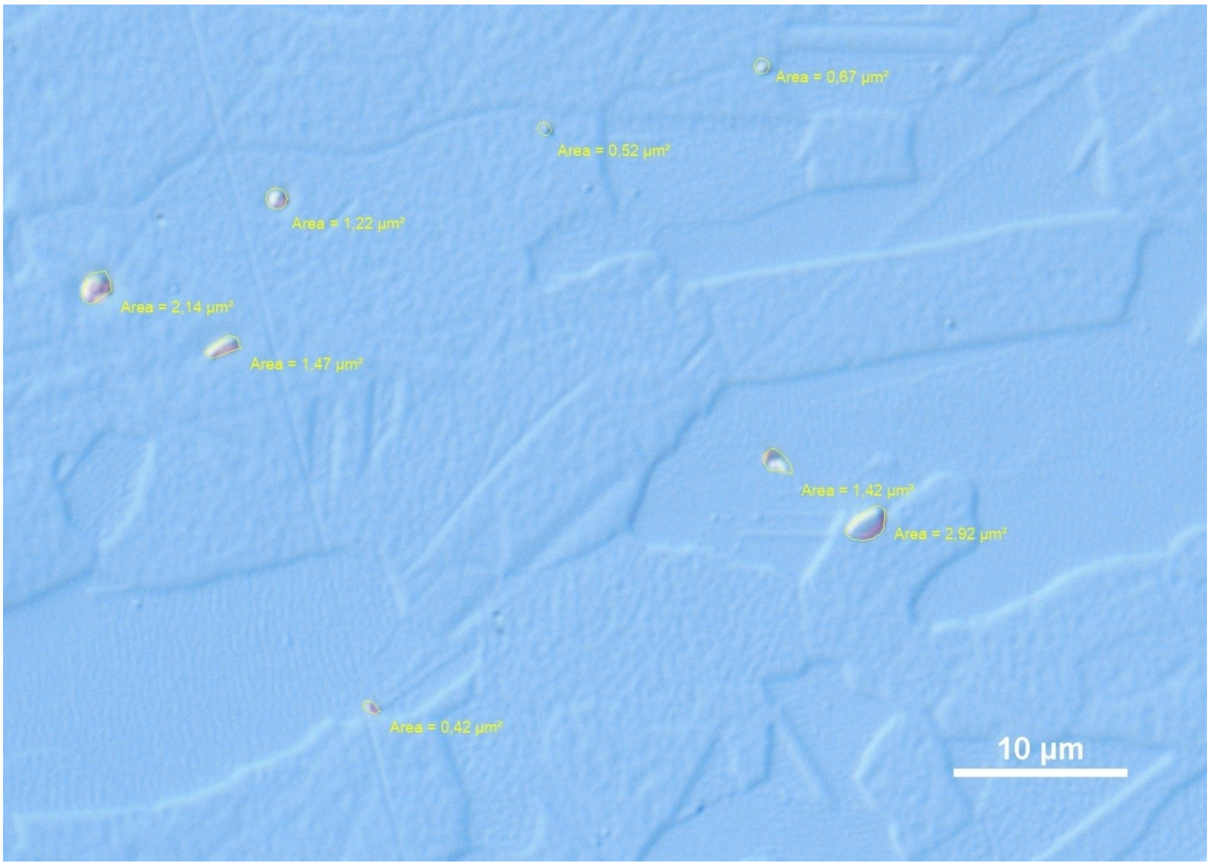

Figure E.9: *347H first area particles, kept at room temperature. Planar view*

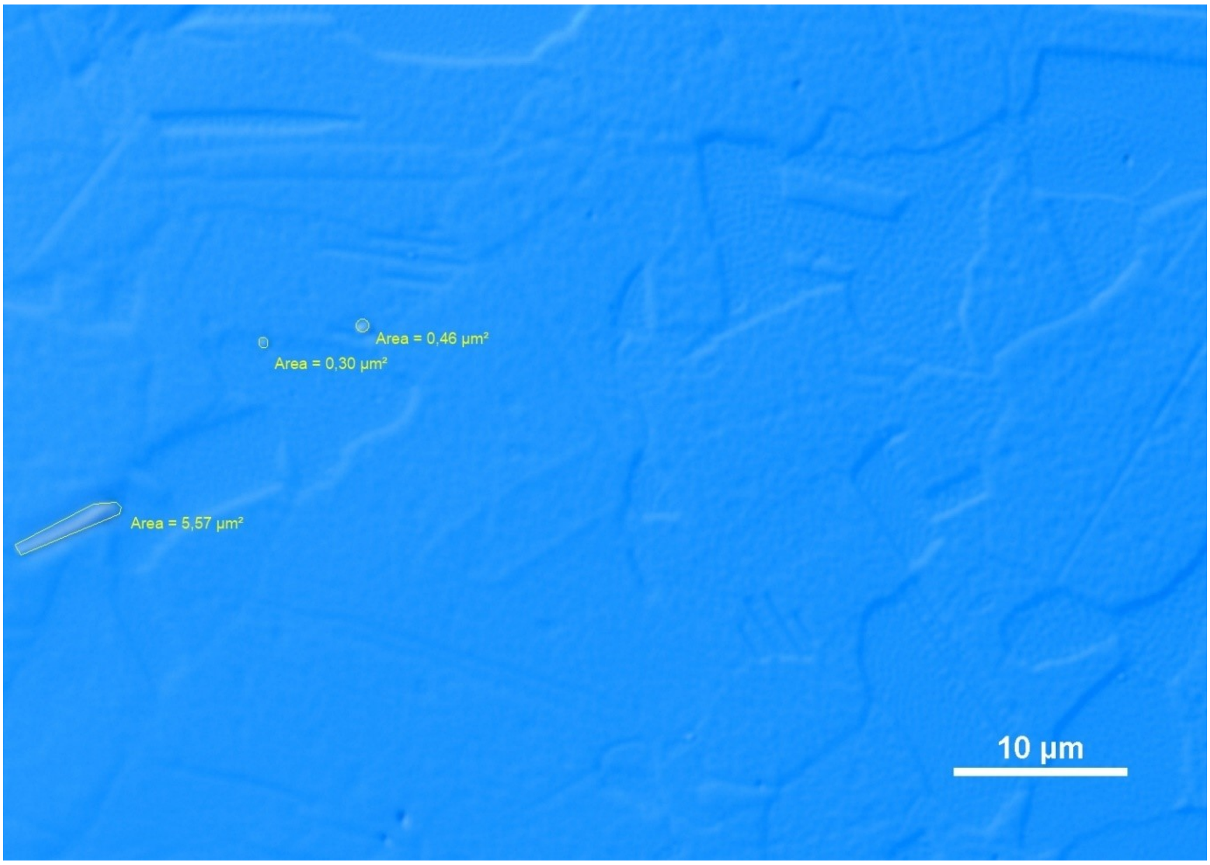

Figure E.10: *347H first area particles, kept at room temperature. Planar view*

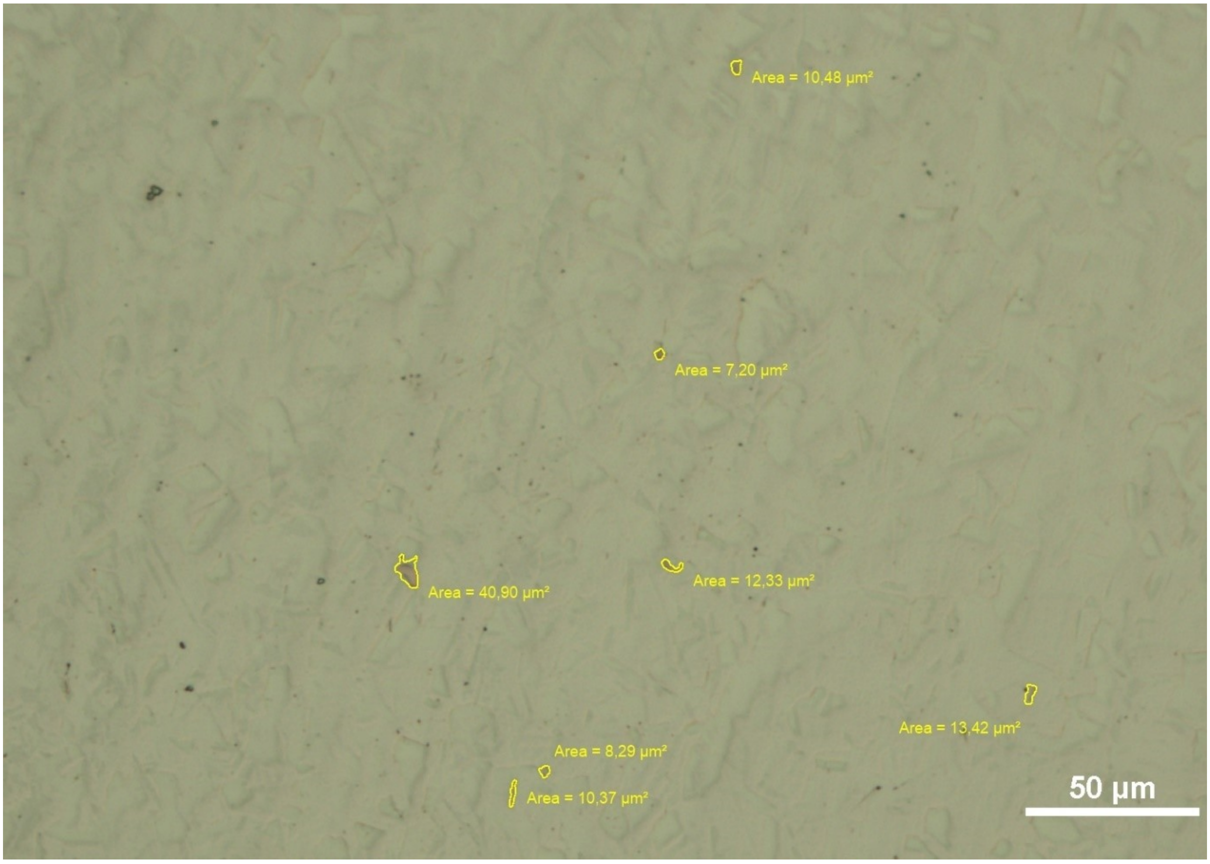

Figure E.11: *347H first area particles, kept at room temperature. Cross-sectional view*

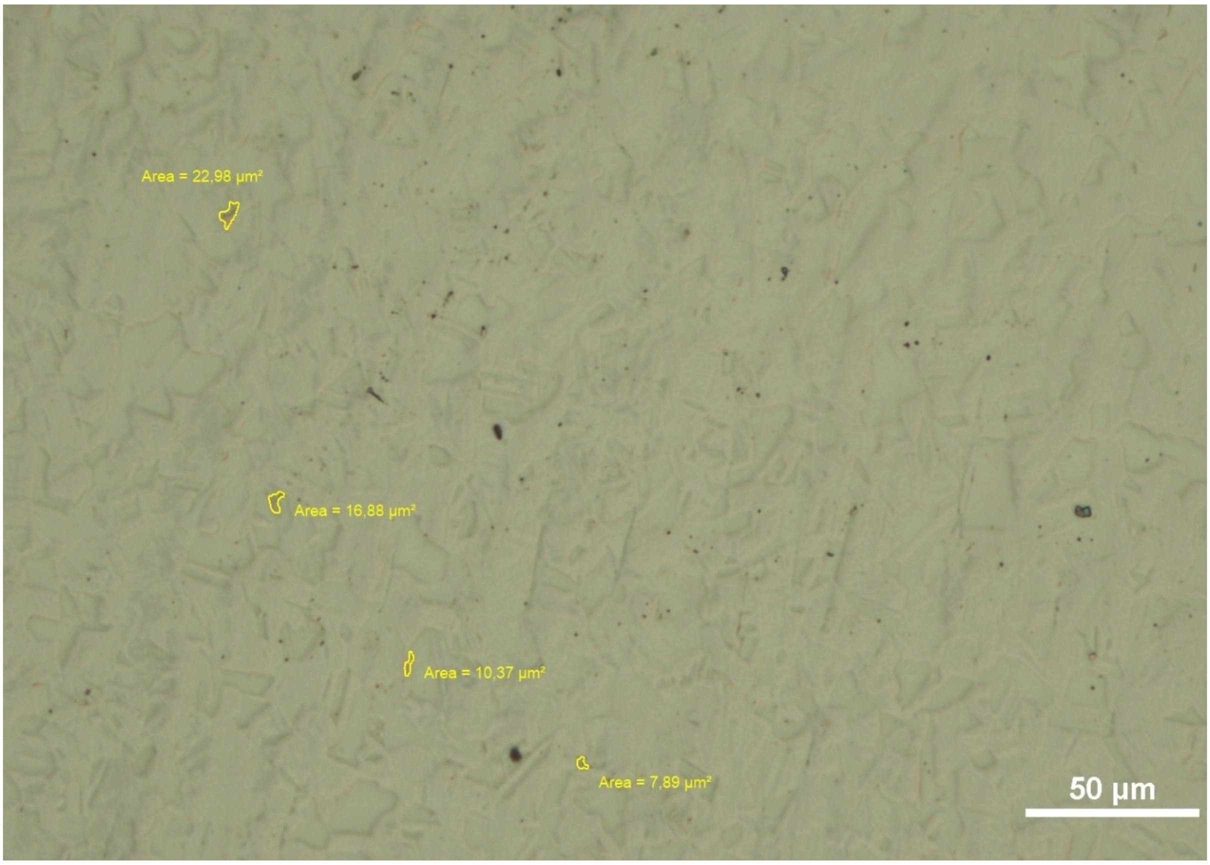

Figure E.12: *347H secondary area particles, kept at room temperature. Cross-sectional view*

Figure E.13: *347H first area particles, heat treated at 1230°C. Planar view*

Figure E.14: *347H secondary area particles, heat treated at 1230°C. Planar view*

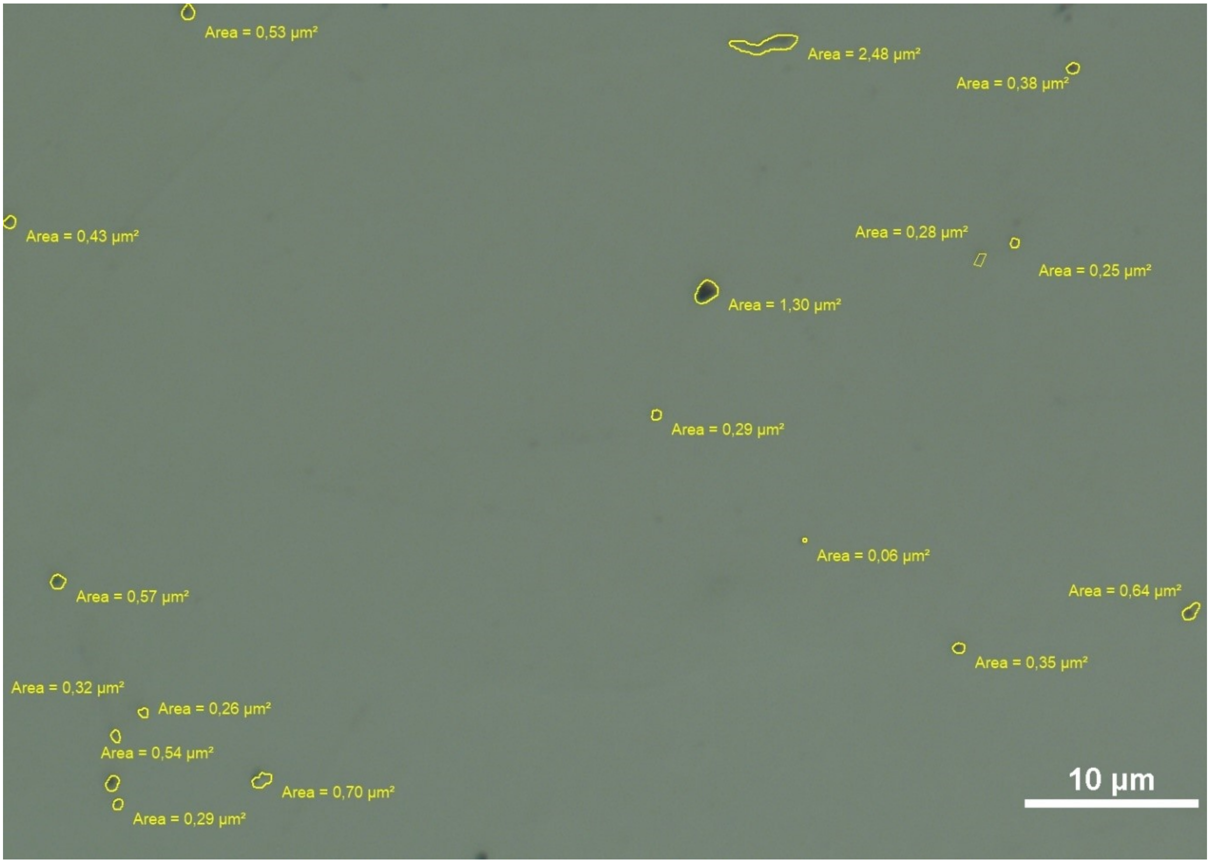

Figure E.15: *347H first area particles, heat treated at 1230°C. Cross-sectional view*

Figure E.16: *347H secondary area particles, heat treated at 1230℃. Cross-sectional view*

The size and the amount of the particles are presented below.

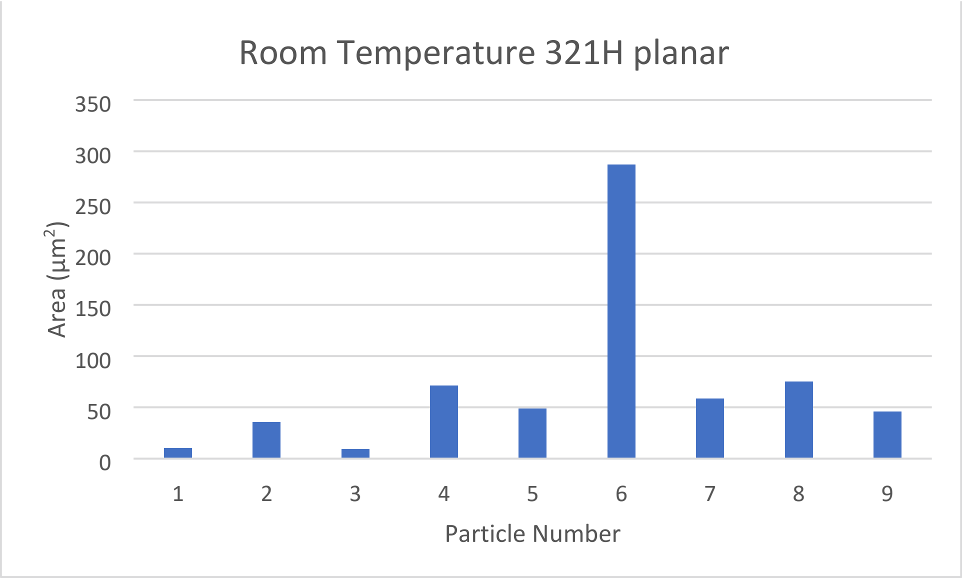

Figure E.17: *321H planar carbide area at room temperature*

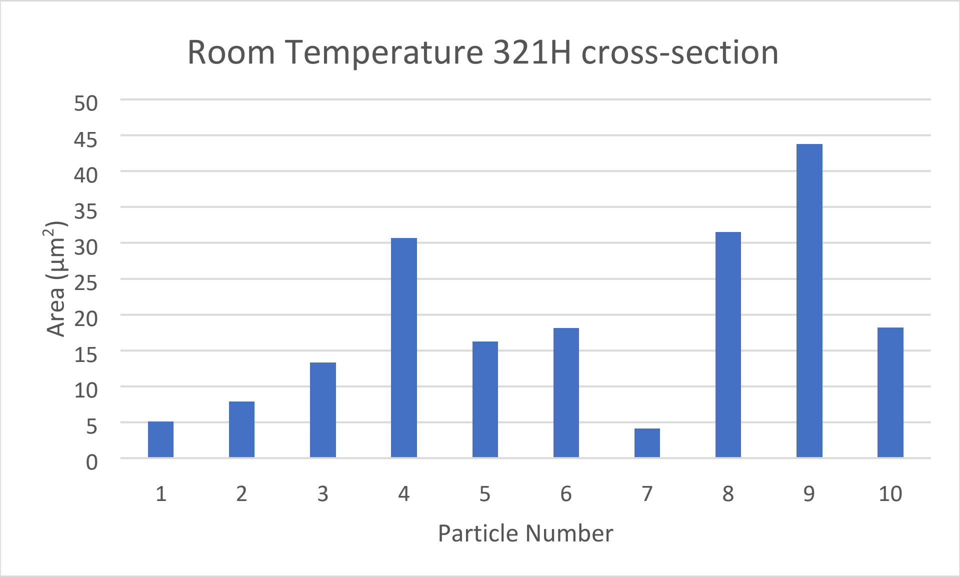

Figure E.18: *321H cross-sectional carbide area at room temperature*

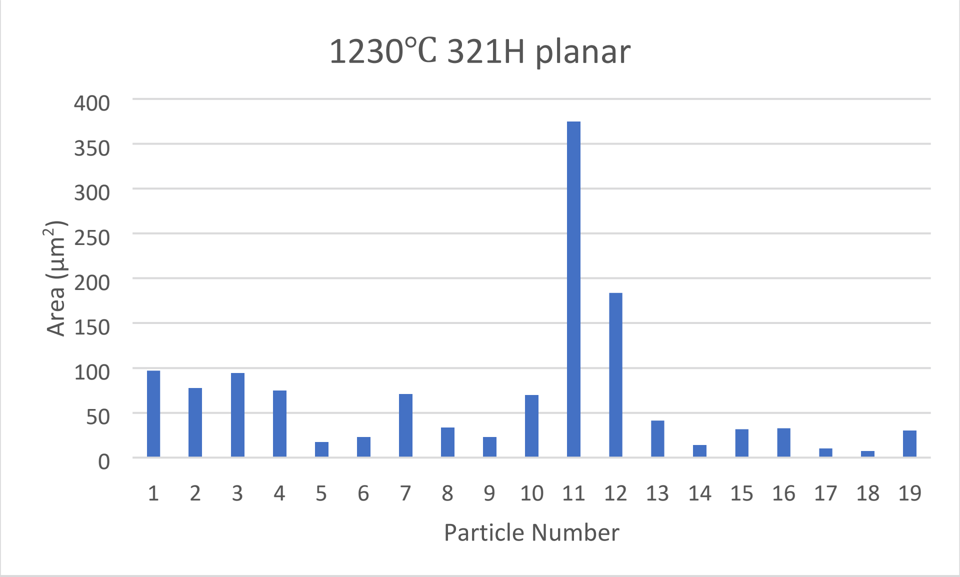

Figure E.19: *321H planar carbide area after heat treatment at 1230℃*

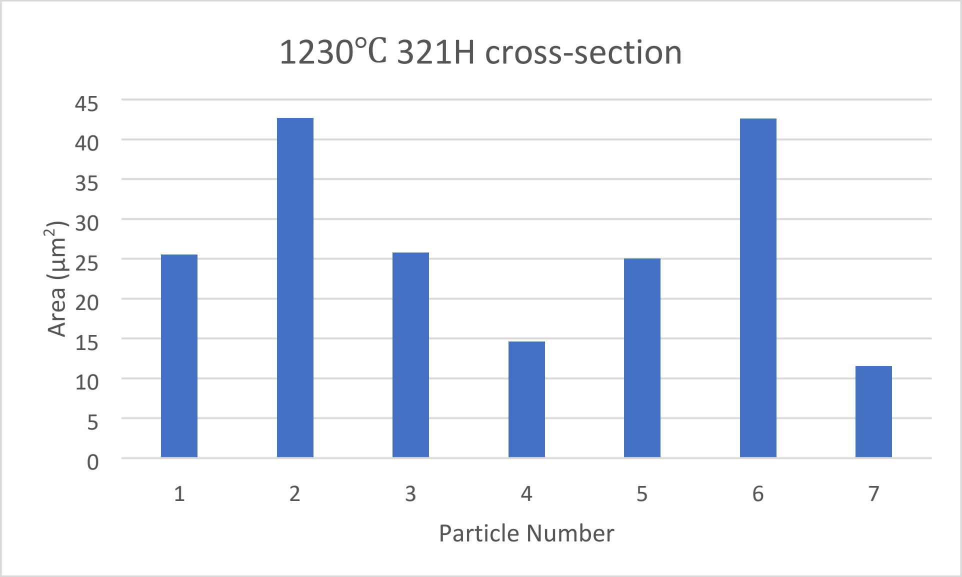

Figure E.20: *321H cross-sectional carbide area after heat treatment at 1230℃*

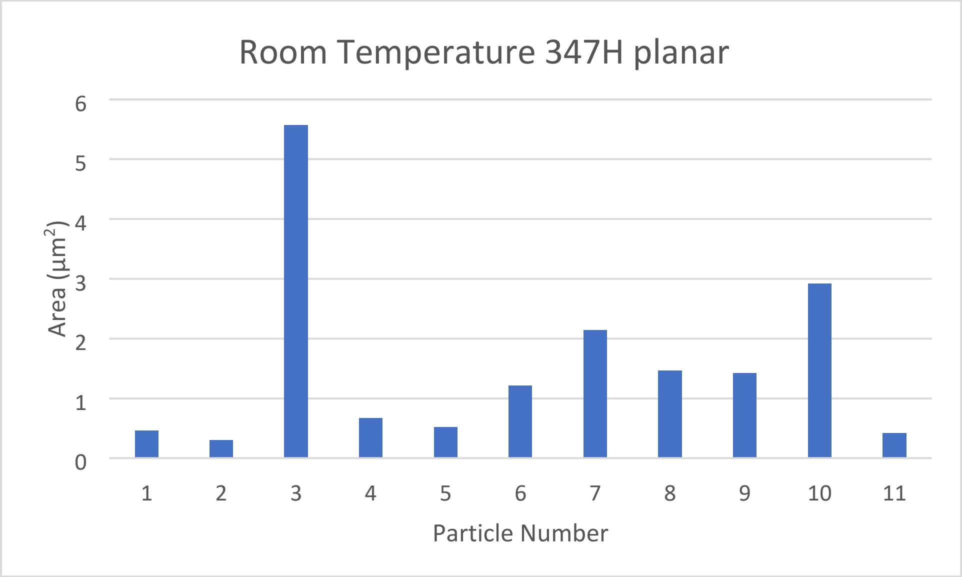

Figure E.21: *347H planar carbide area after heat treatment at room temperature*

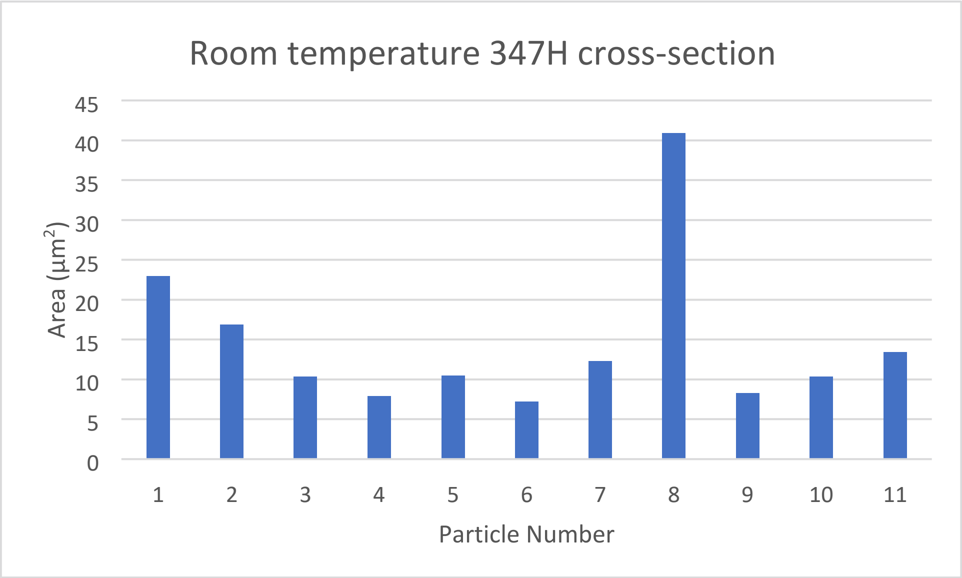

Figure E.22: *347H cross-sectional carbide area after heat treatment at room temperature*

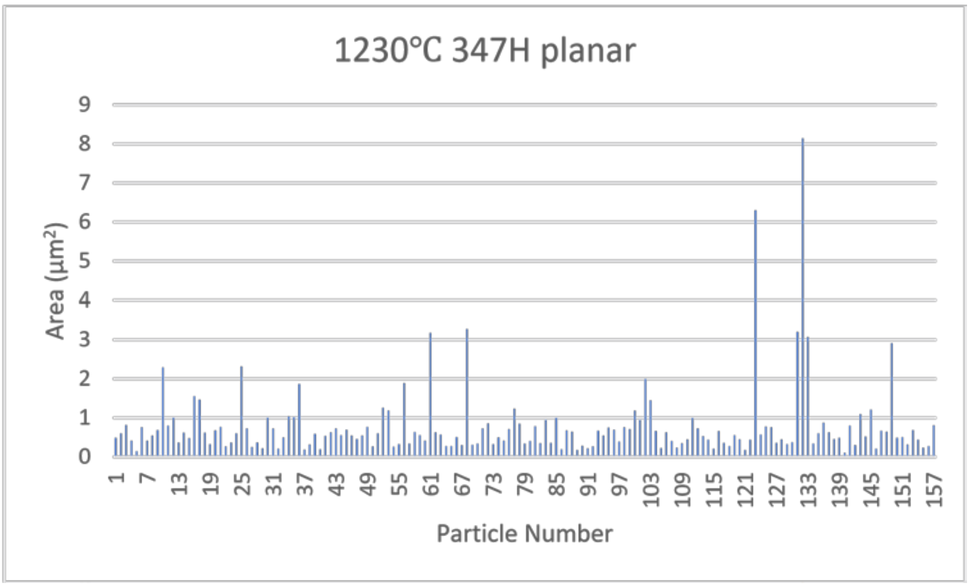

Figure E.23: *347H planar carbide area after heat treatment at 1230℃*

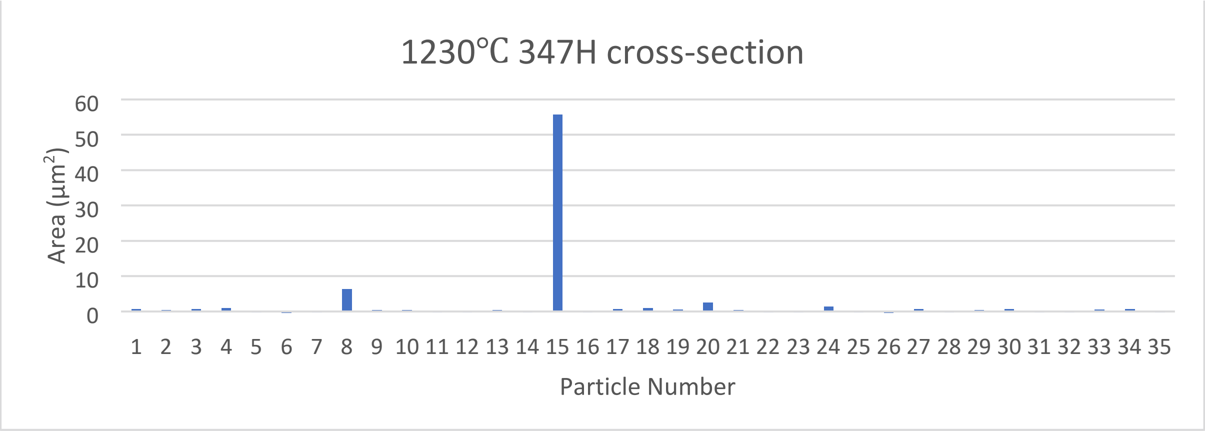

Figure E.24: *347H cross-sectional carbide area after heat treatment at 1230℃*

Appendix F

,

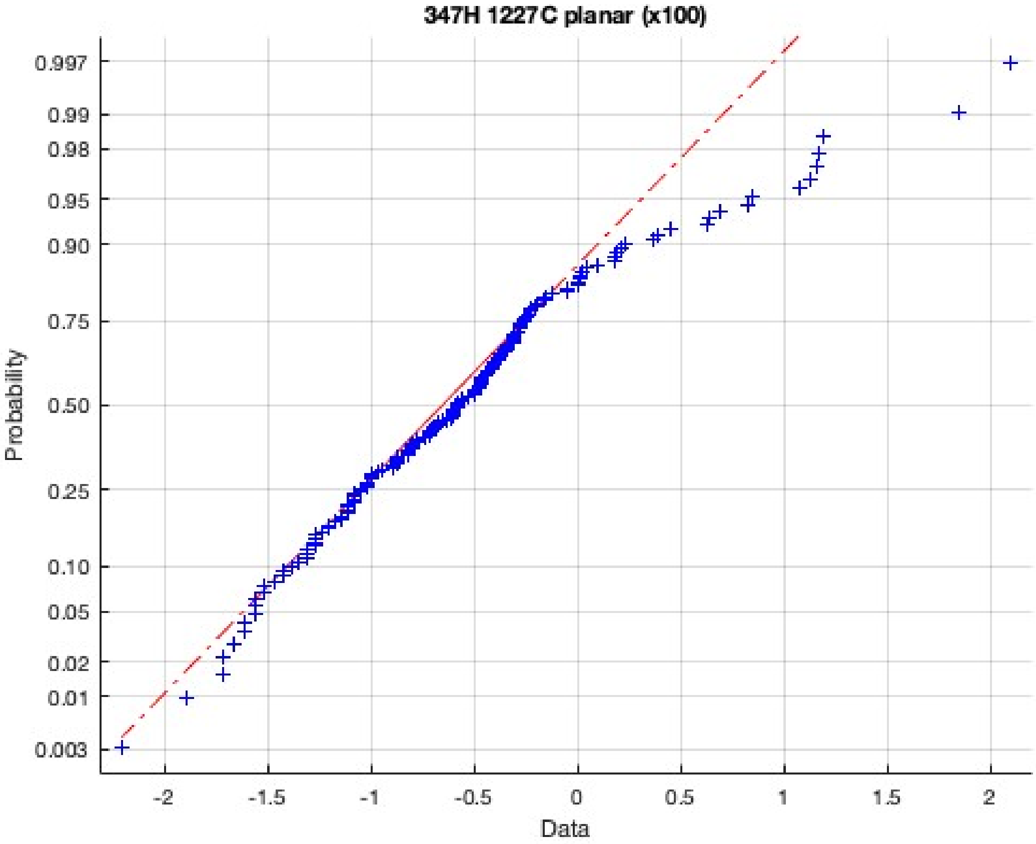

Figure F.1: *The particle distribution in a planar sample which has been exposed to 1230℃ and N_2-gas*

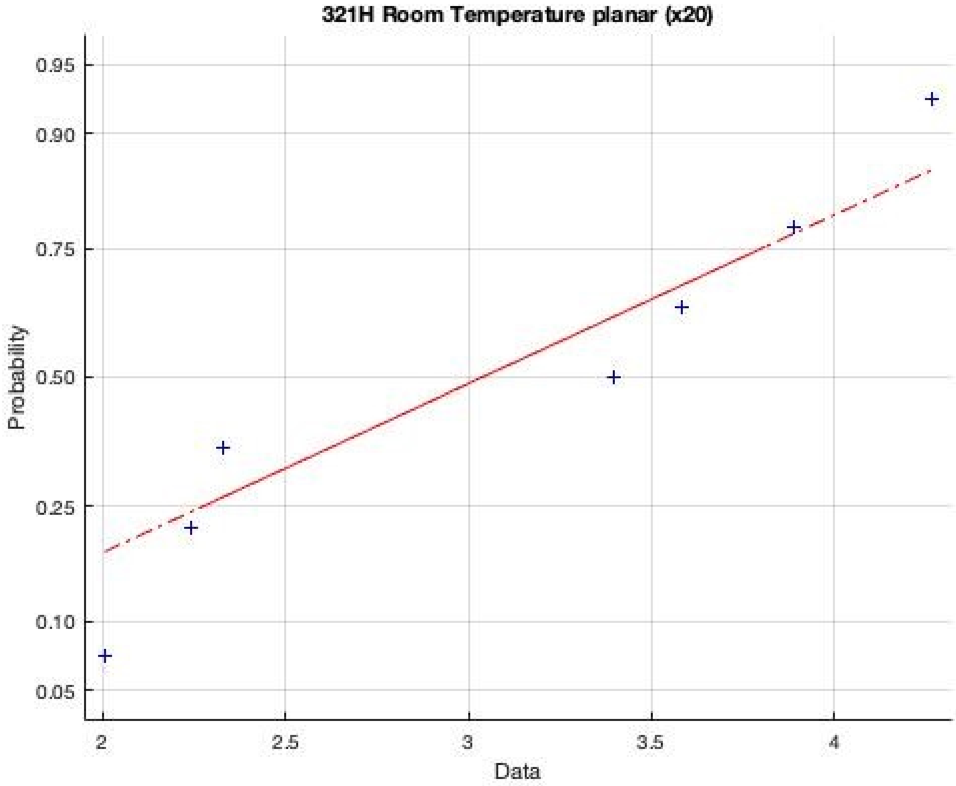

Figure F.2: *321H kept at room temperature, particle distribution from the planar view*

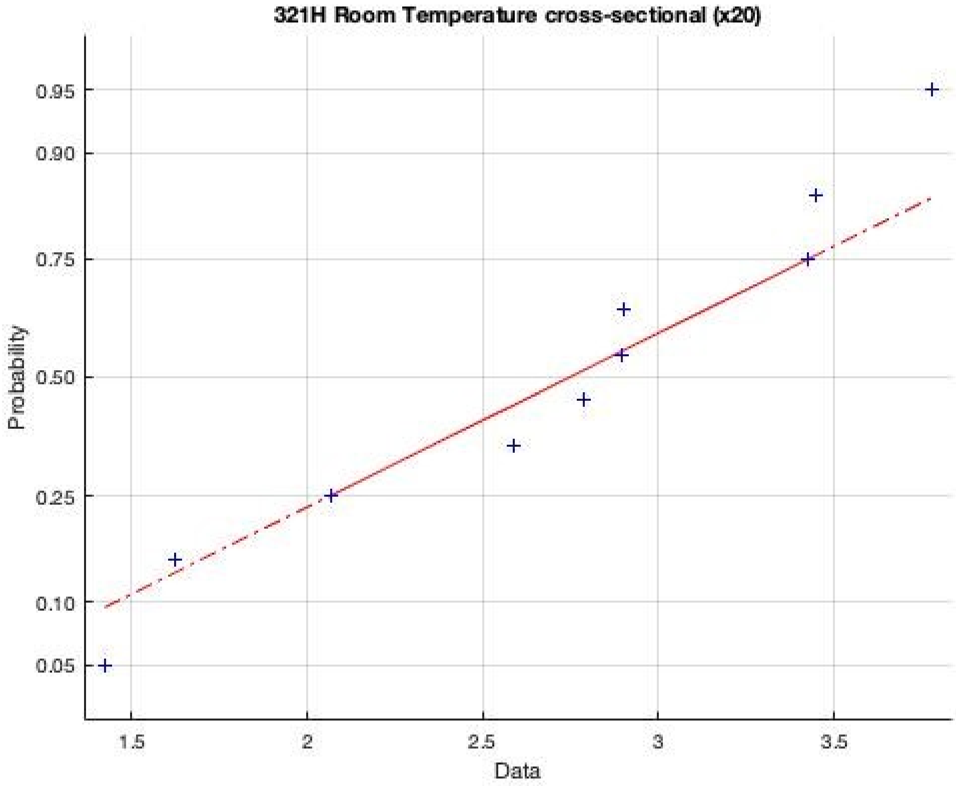

Figure F.3: *321H kept at room temperature, particle distribution from the cross-sectional view*

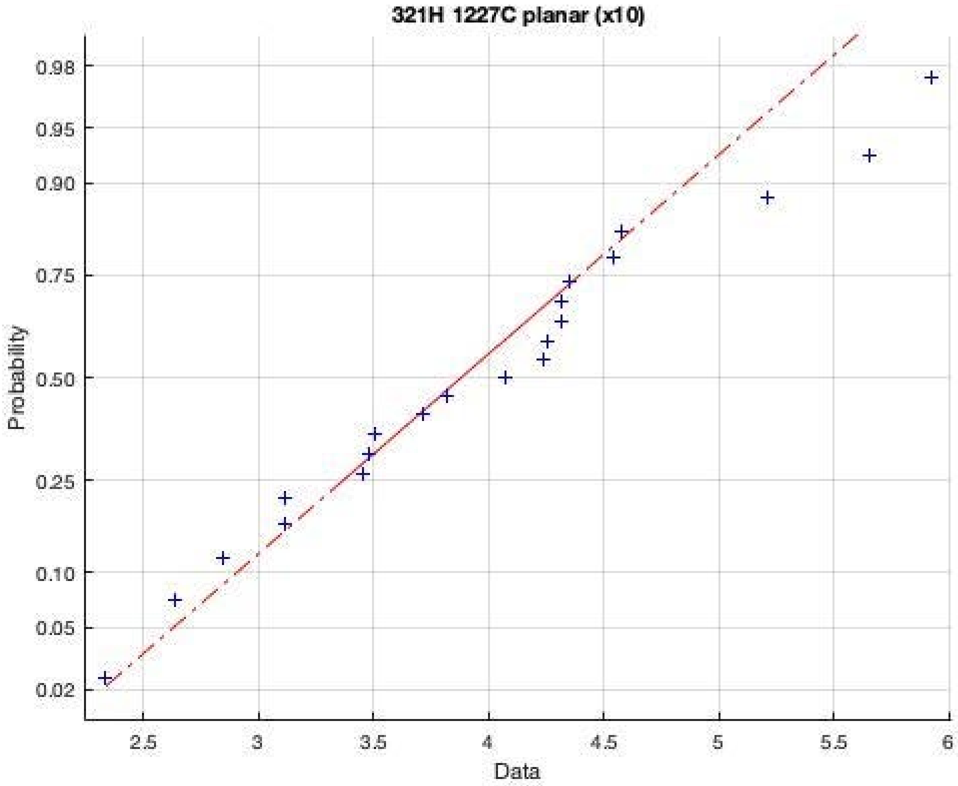

Figure F.4: *321H heat treated at 1230*℃*, particle distribution from the planar view*

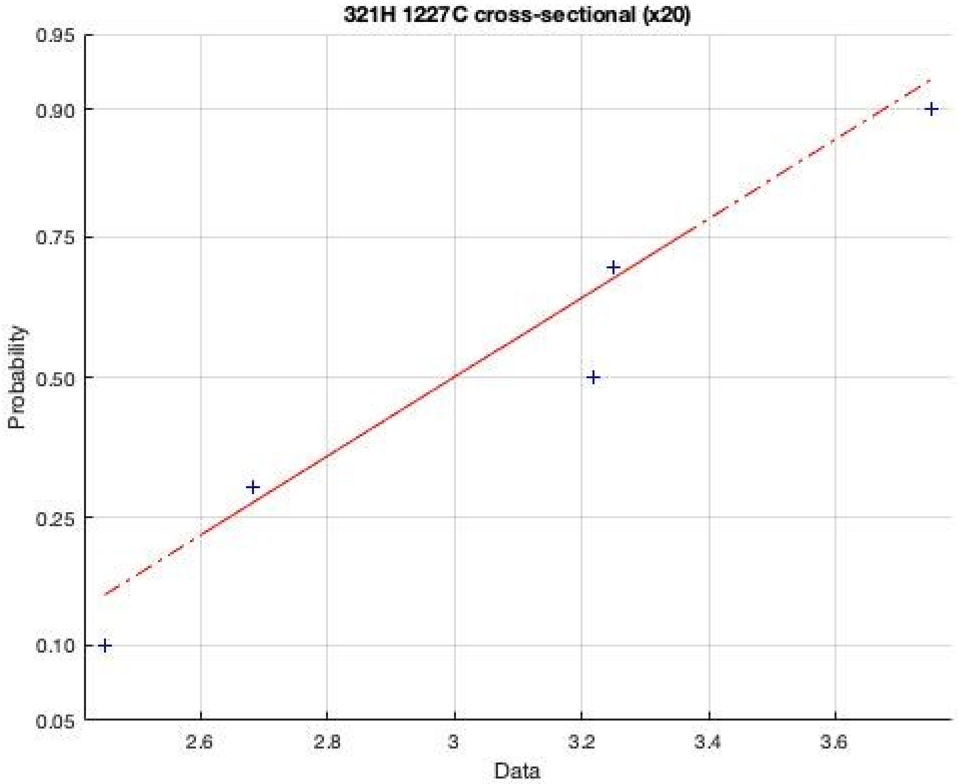

Figure F.5: *321H heat treated at 1230*℃*, particle distribution from the cross-sectional view*

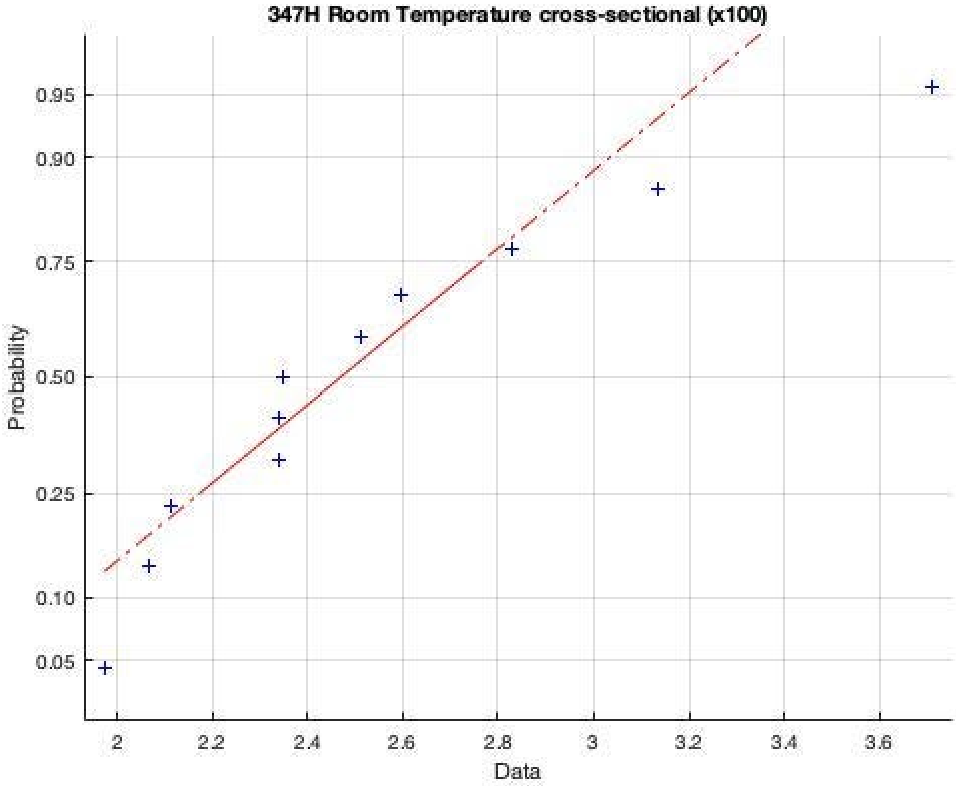

Figure F.6: *347H kept at room temperature, particle distribution from the cross-sectional view*

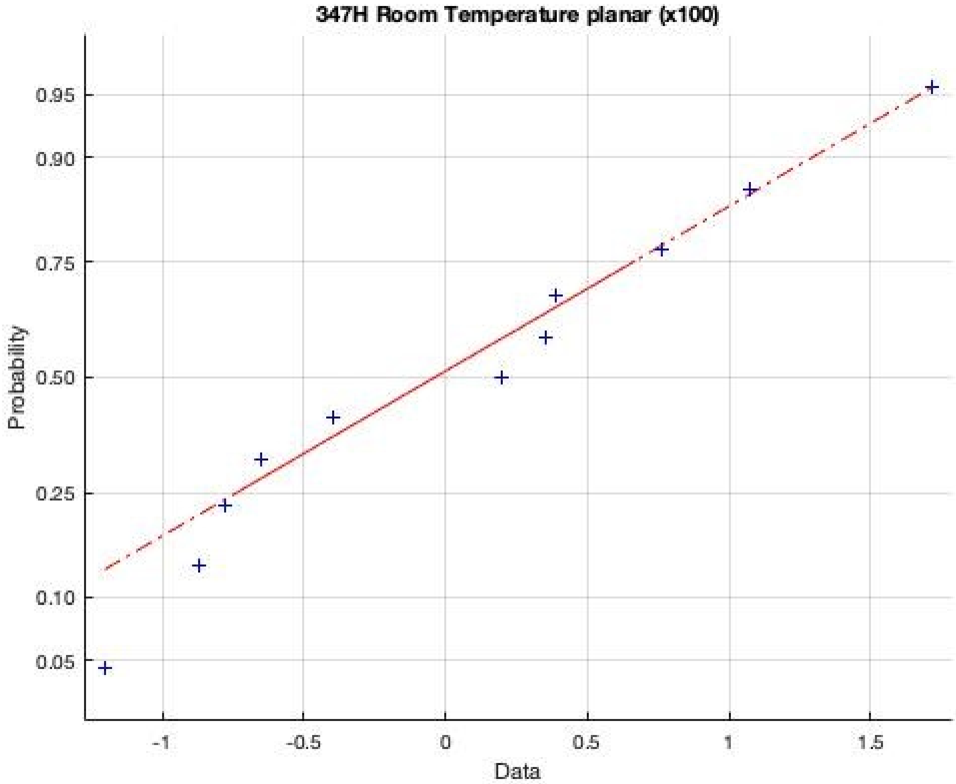

Figure F.7: *347H kept at room temperature, particle distribution from the planar view*

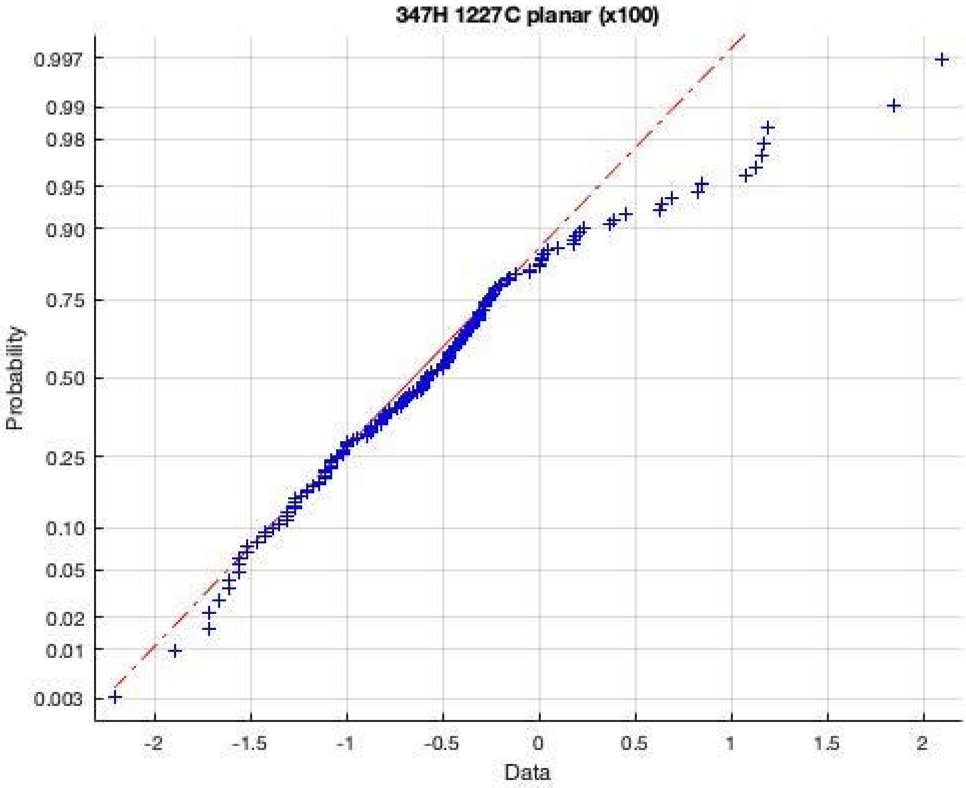

Figure F.8: *347H heat treated at 1230°C, particle distribution from the planar view*

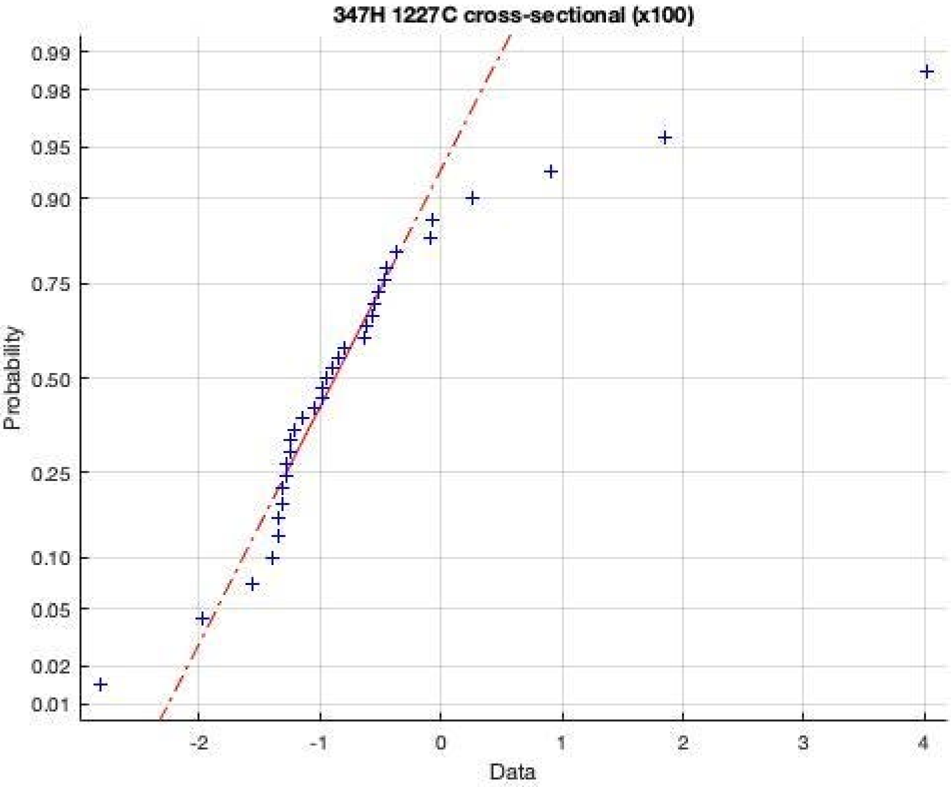

Figure F.9: *347H heat treated at 1230°C, particle distribution from the cross-sectional view*

Appendix G

The force applied on the samples to achieve different levels of plastic deformation.

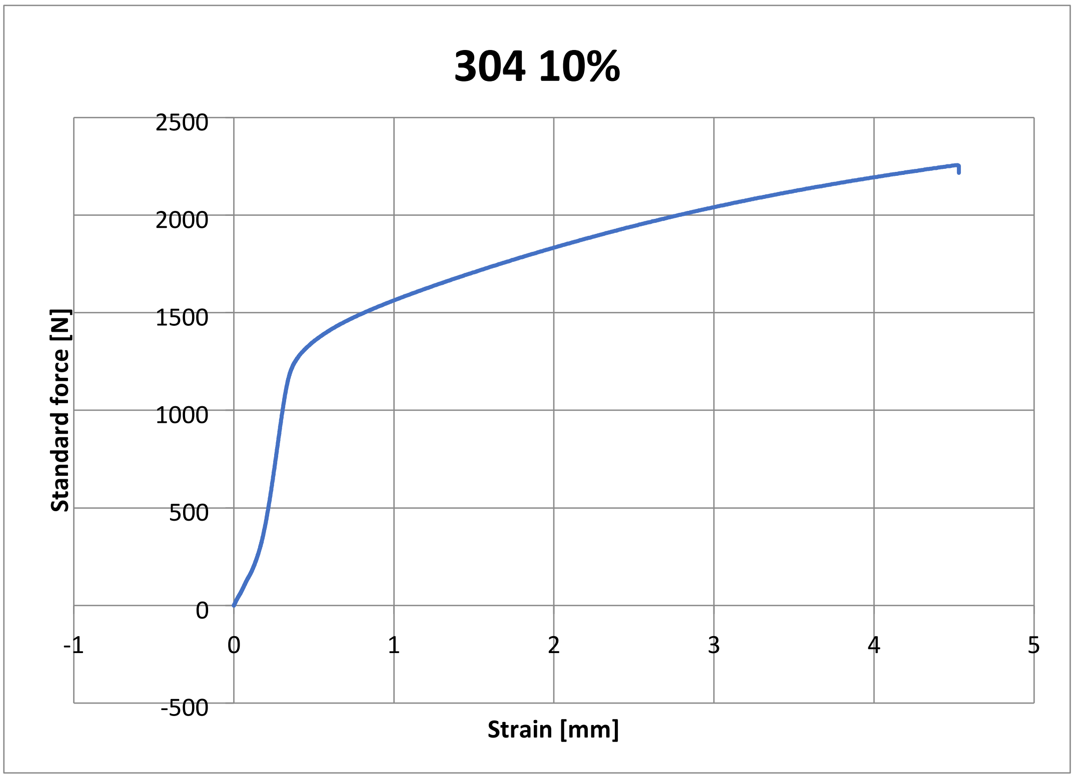

Figure G.1: *304 stainless steel deformed to 10% plastic deformation*

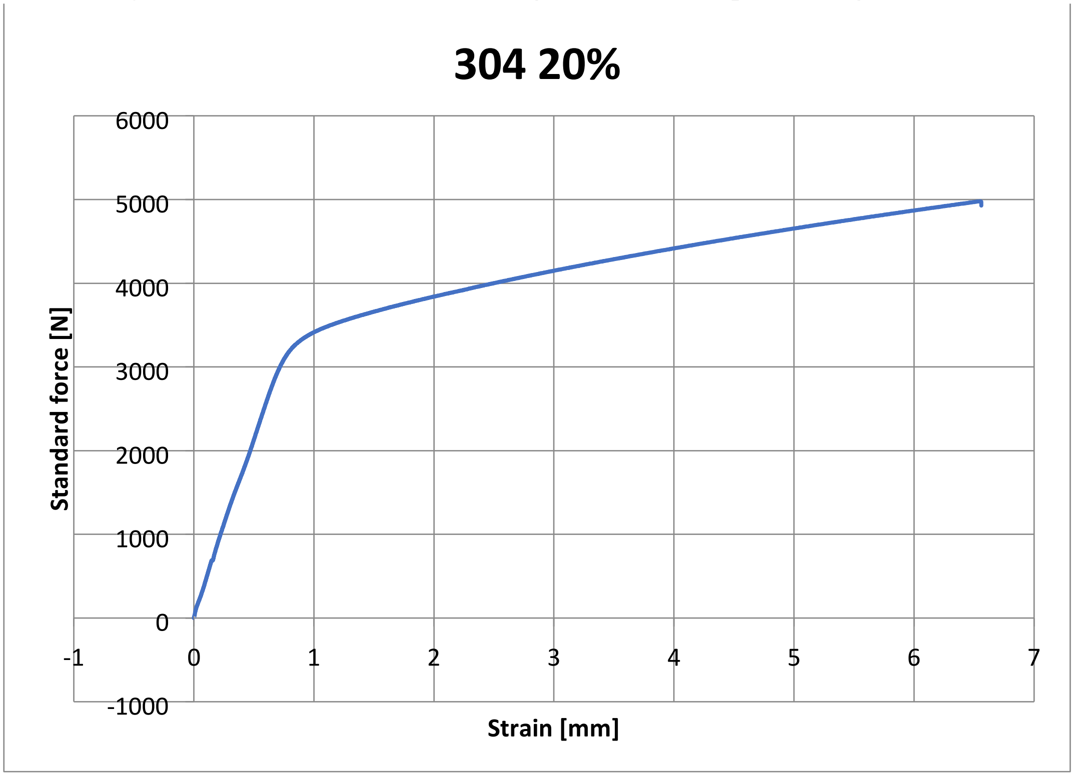

Figure G.2: *304 stainless steel deformed to 20% plastic deformation*

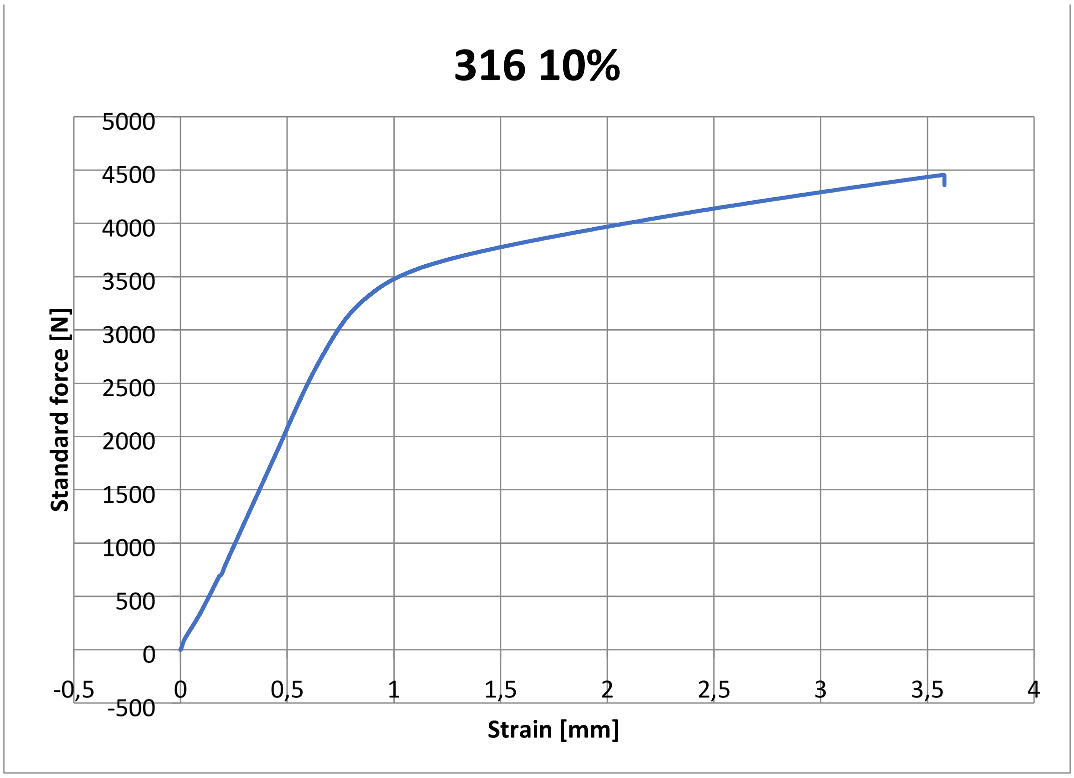

Figure G.3: *316 stainless steel deformed to 10% plastic deformation*

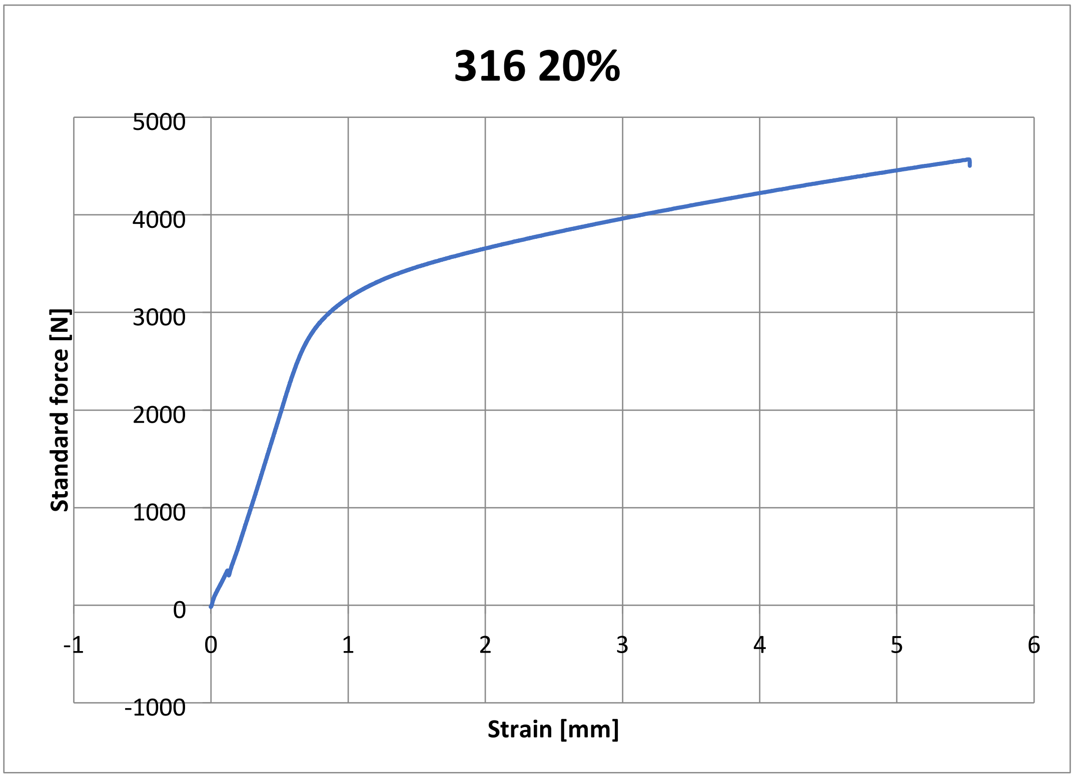

Figure G.4: *316 stainless steel deformed to 20% plastic deformation*

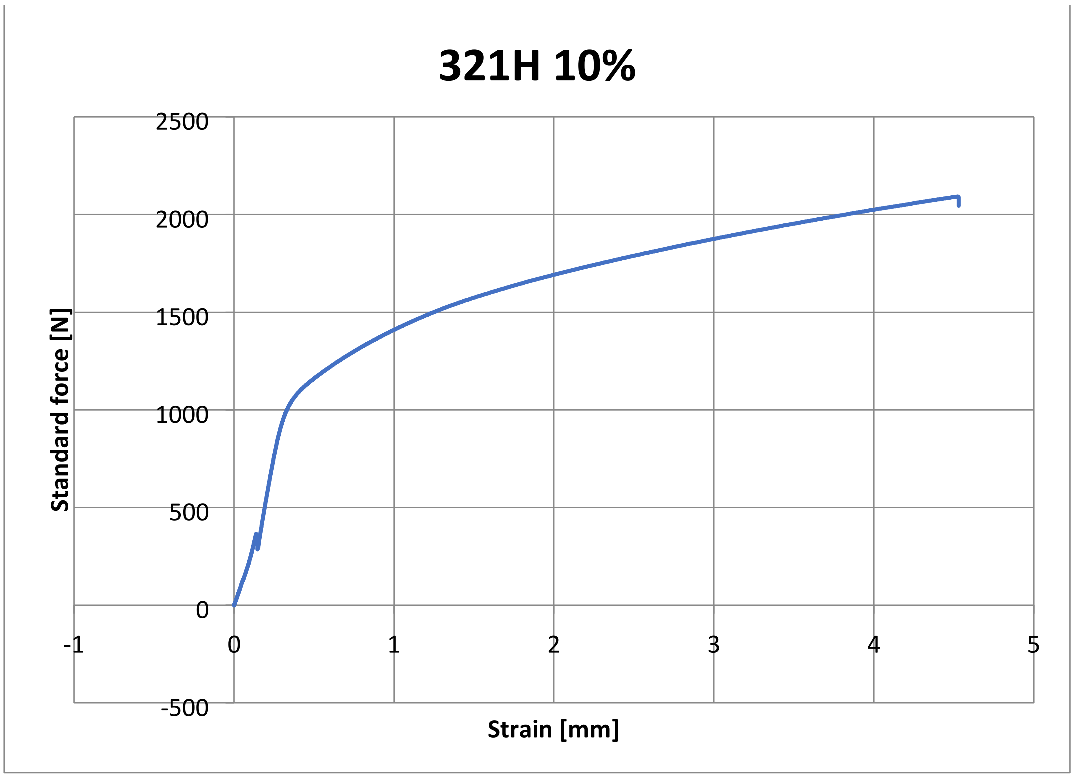

Figure G.5: *321H stainless steel deformed to 10% plastic deformation*

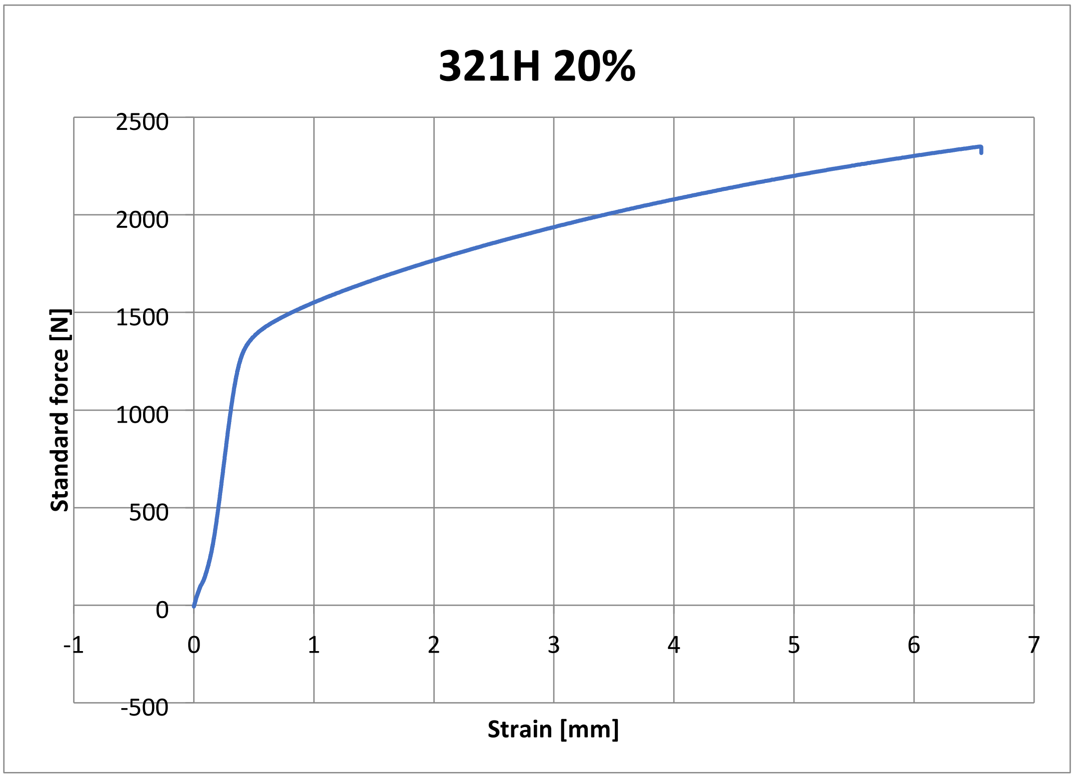

Figure G.6: *321H stainless steel deformed to 20% plastic deformation*

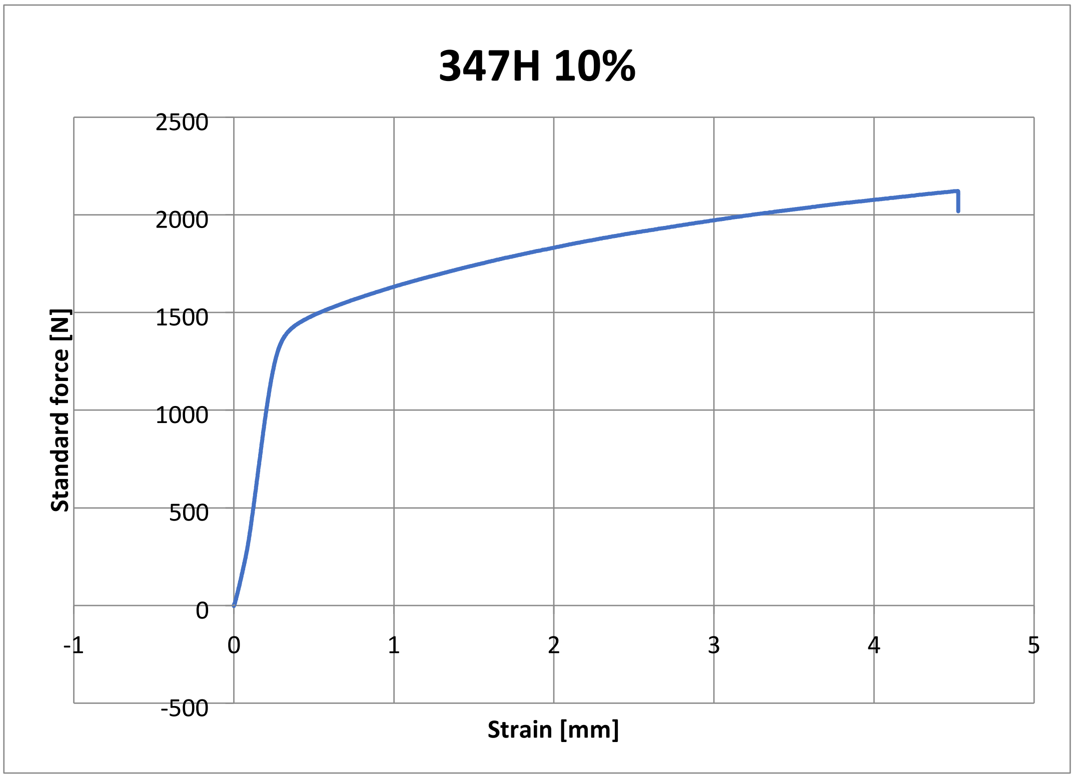

Figure G.7: *347H stainless steel deformed to 10% plastic deformation*

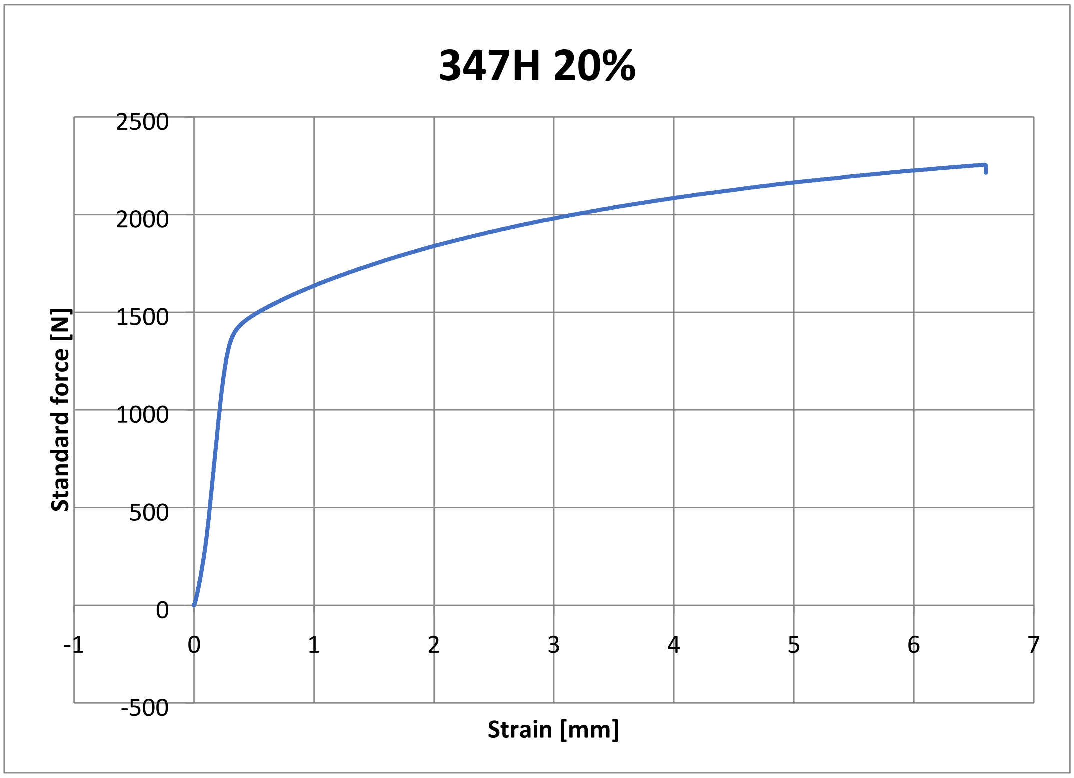

Figure G.8: *347H stainless steel deformed to 20% plastic deformation*

The following figures shows the images of the plastically strained and then heat treated samples at 1230℃.

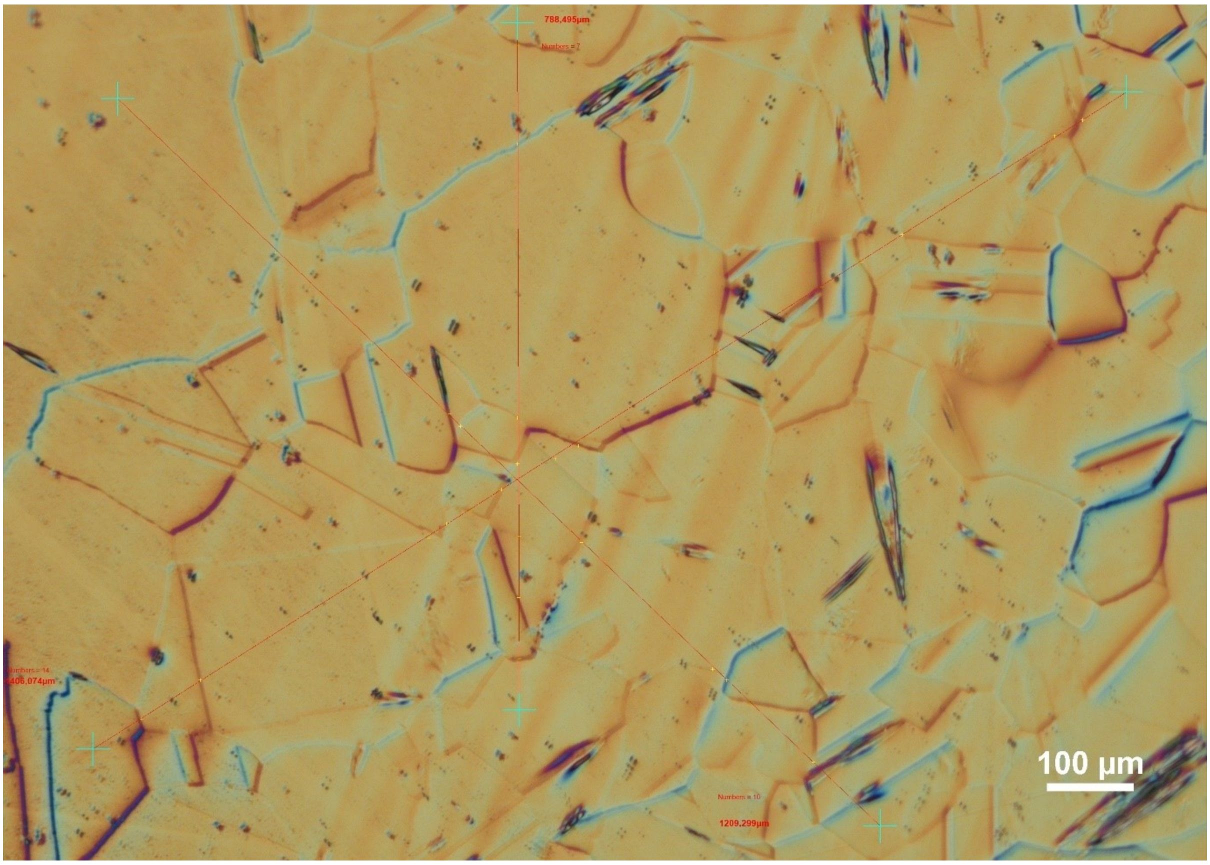

Figure G.9: *347H sample deformed 20% and heat treated at 1230℃*

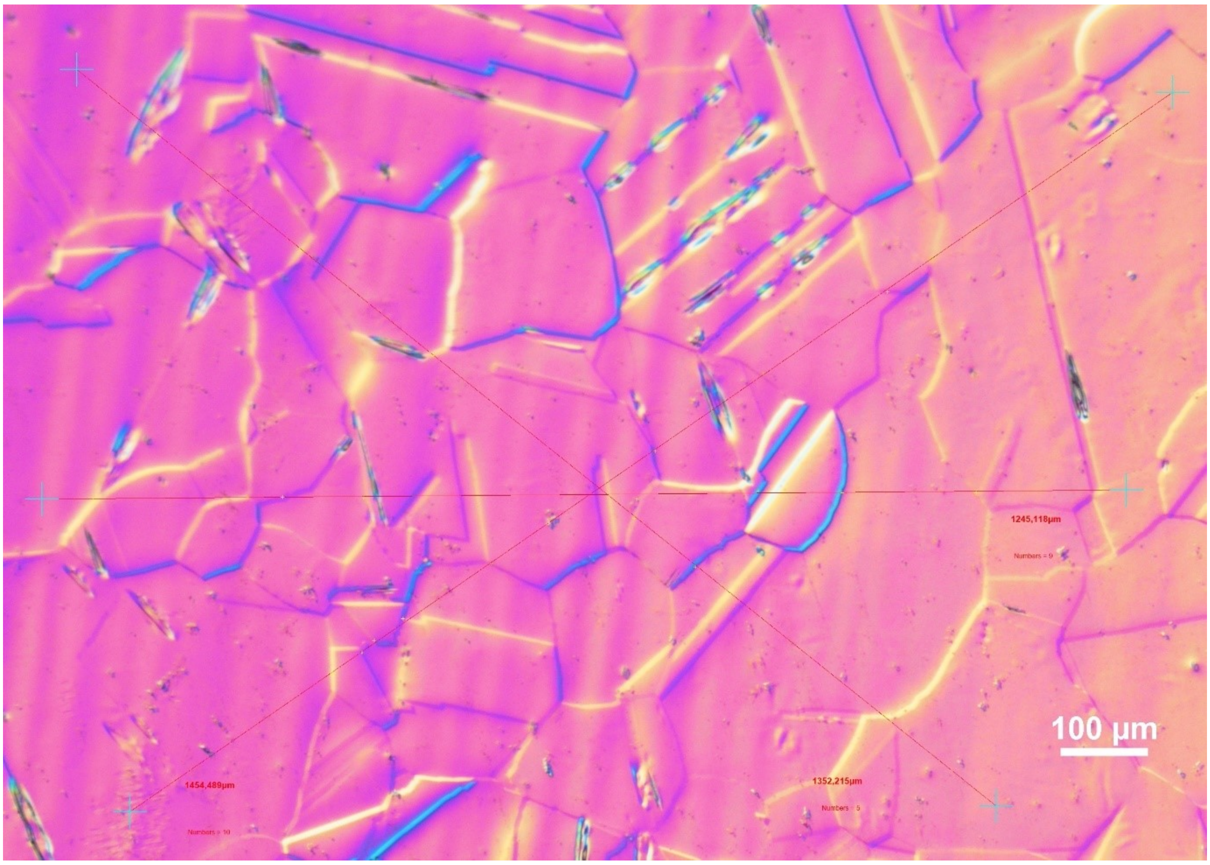

Figure G.10: *347H sample deformed 10% and heat treated at 1230℃*

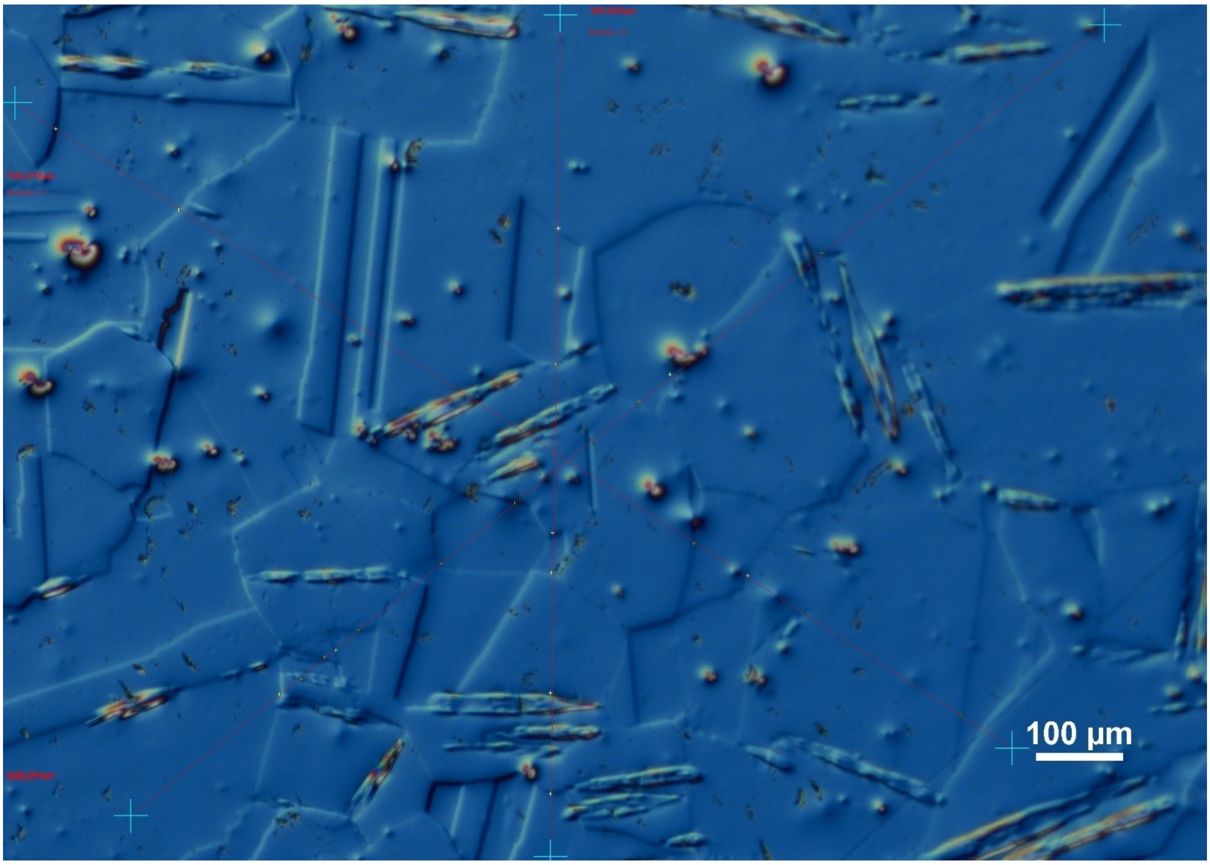

Figure G.11: *321H sample deformed 20% and heat treated at 1230℃*

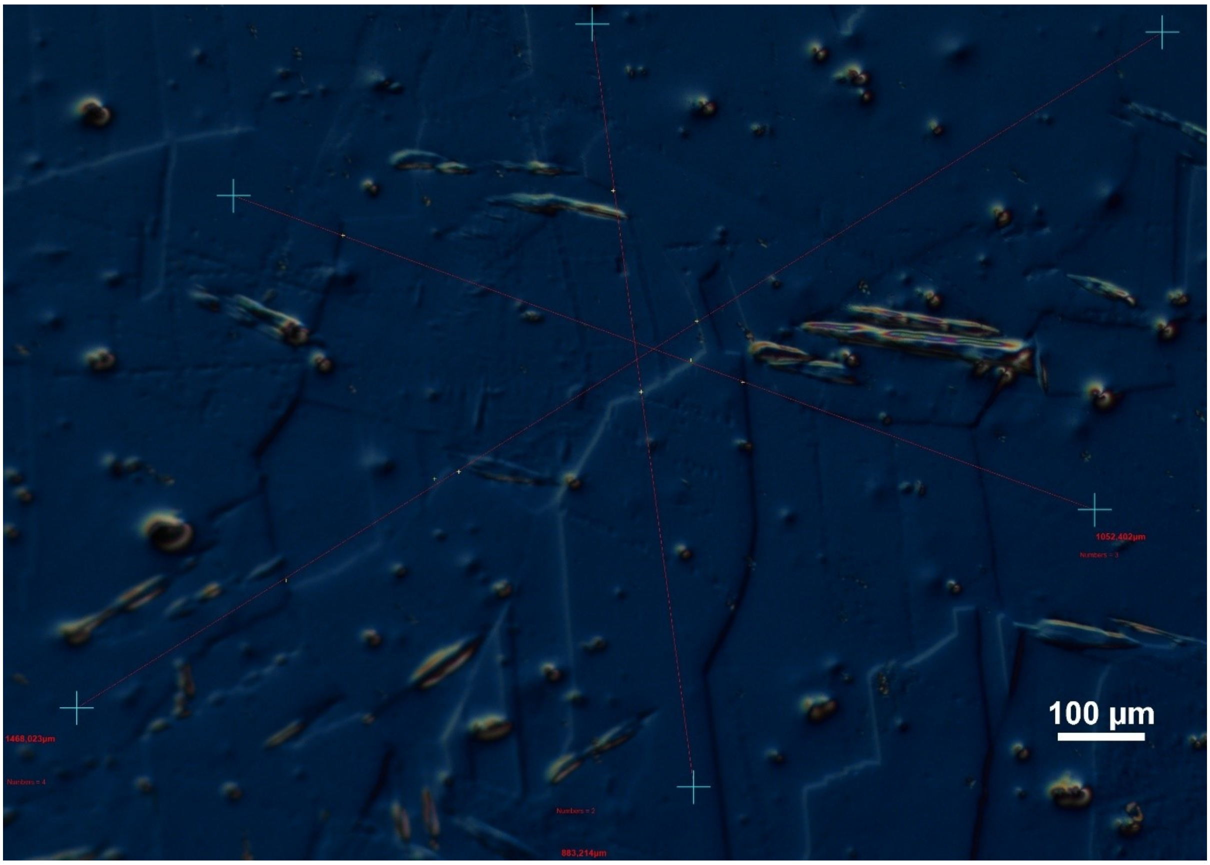

Figure G.12: *321H sample deformed 10% and heat treated at 1230℃*

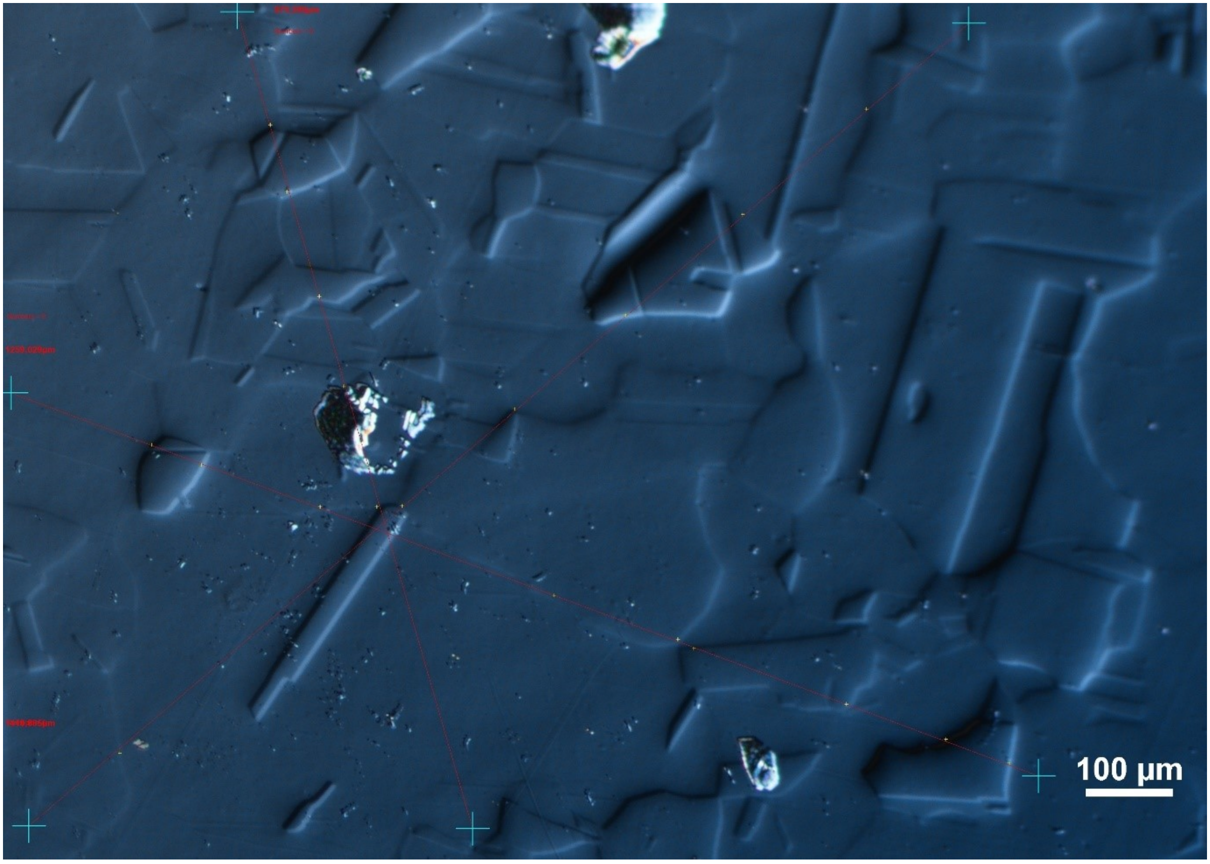

Figure G.13: *316 sample deformed 20% and heat treated at 1230℃*

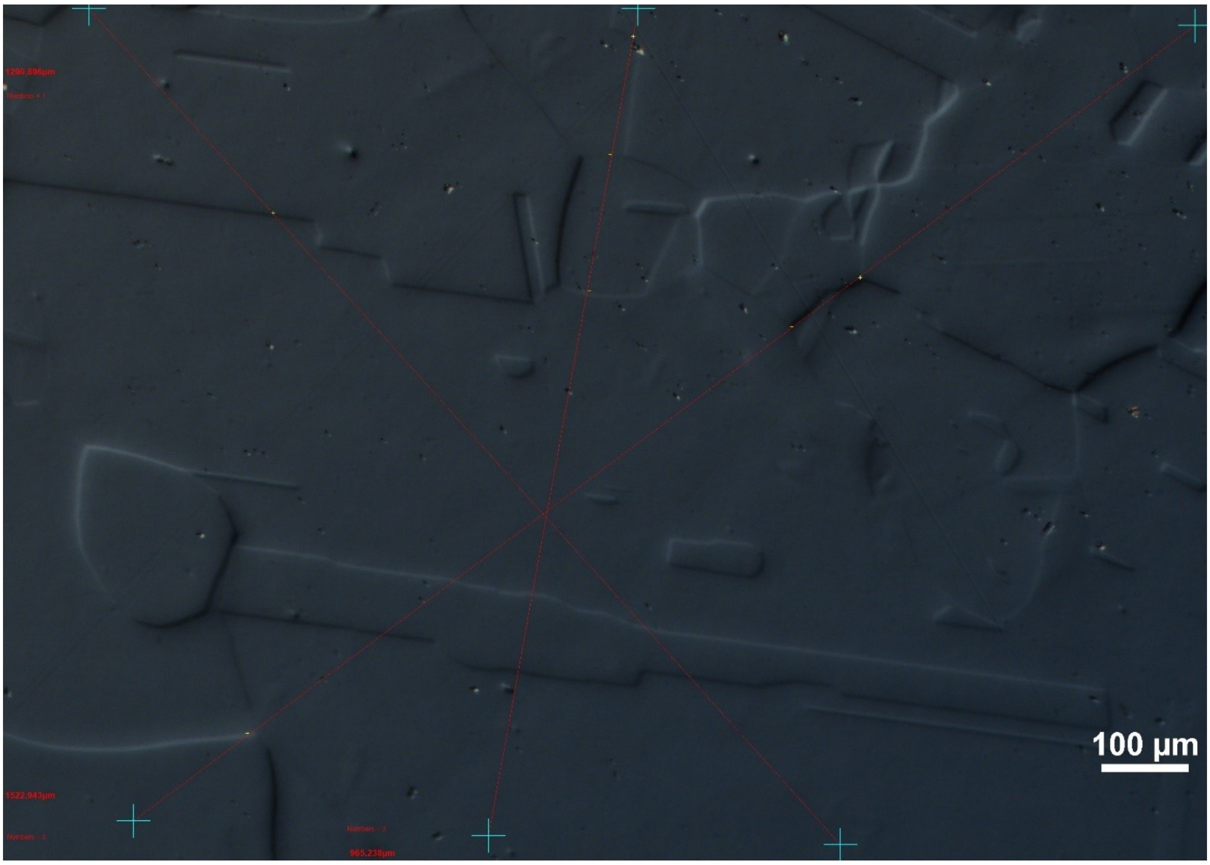

Figure G.14: *316 sample deformed 10% and heat treated at 1230℃*

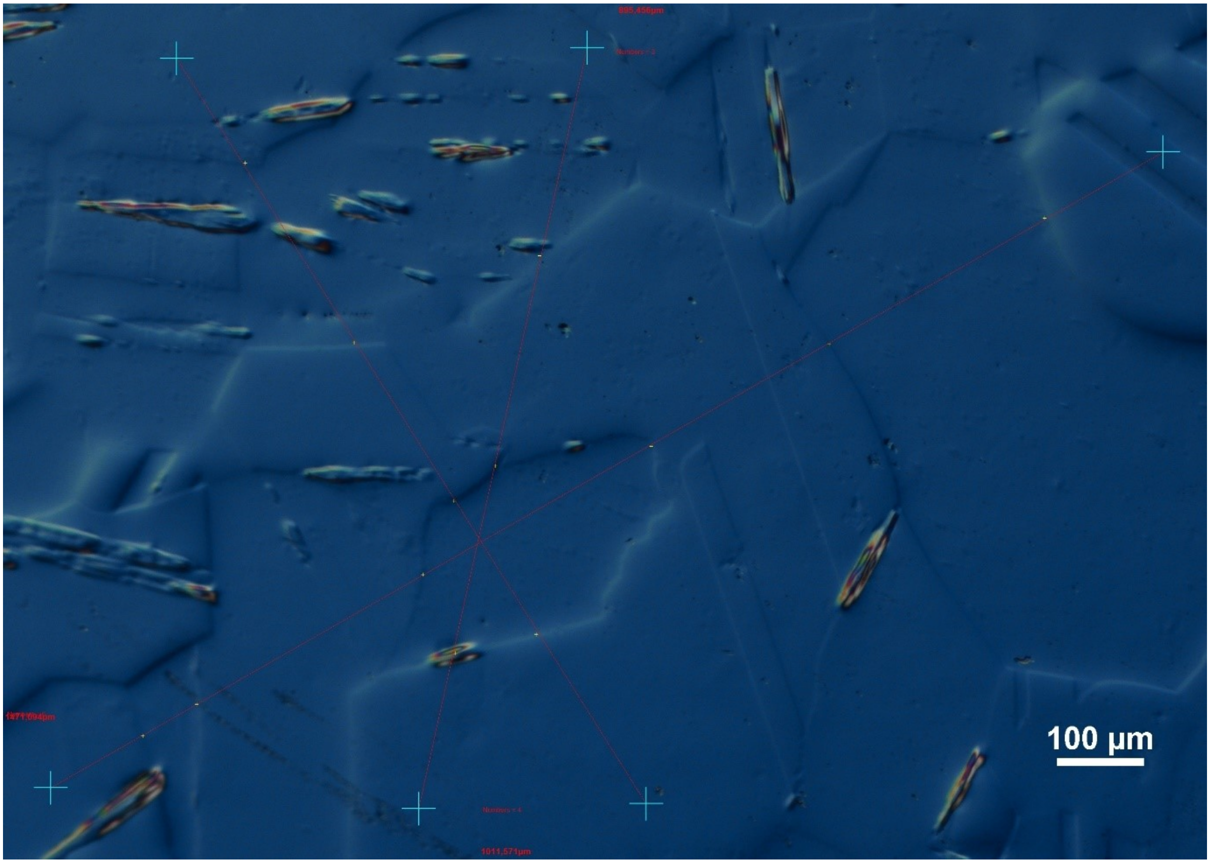

Figure G.15: *304 sample deformed 20% and heat treated at 1230℃*

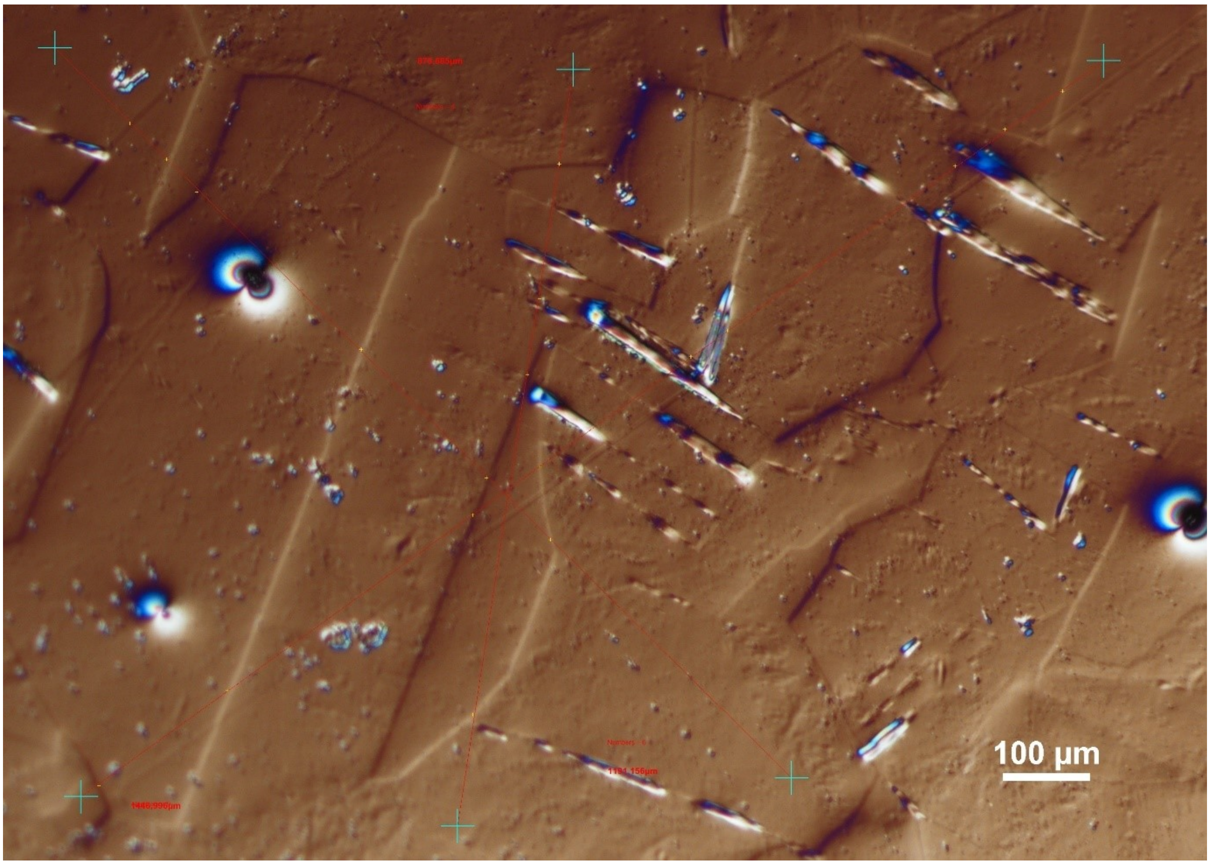

Figure G.16: *304 sample deformed 10% and heat treated at 1230°C*